Coupled Geochemical and Nano-Petrophysical Study of the Utica Play,

Appalachian Basin,

Ohio, U.S.A.

By

Dillon Worley

Presented to the Faculty of the Graduate School of

The University of Texas at Arlington in Partial Fulfillment

of the Requirements

for the Degree of

MASTERS OF SCIENCE IN EARTH AND ENVIRONMENTAL SCIENCES

THE UNIVERSITY OF TEXAS AT ARLINGTON

October 2017

I

Acknowledgements

Abstract

Coupled Geochemical and Nano-Petrophysics of the Utica Play,

Appalachian Basin,

Ohio, USA

Dillon Thomas Worley, M.S.

The University of Texas at Arlington, 2017

Supervising Professor: Q.H. Hu

Being more extensive than the Marcellus Play, the Utica Play covers from New York state in the north to northeastern Kentucky and Tennessee in the south. The Utica Play is a stacked play consisting of organic-rich mudstones from upper Ordovician units of Utica Shale, Point Pleasant, and the Logana member of the Lexington/Trenton Limestone. This study will focus on the pore structure and rock-fluid interaction and with relation to the rocks geochemical properties to assess the Utica Play. To achieve this research purpose, 7 core samples and 16 cuttings, with different maturities were collected from various wells, to study rocks from Utica Shale, Point Pleasant, and Lexington Limestone, as well as the Kope Formation which is immediately above the Utica Shale.

The research investigated the nano-petrophysics by the means of mercury injection capillary pressure (MICP), helium porosity and permeability, low-pressure nitrogen gas physisorption, contact angle, and spontaneous imbibition. The geochemistry of rocks was analyzed by pyrolysis and total organic content (TOC) measurements, while mineralogy was determined by X-ray diffraction (XRD). MICP results indicate that clay-rich formations have more intra-clay, organic-matter, and intragranular pores (2.8-50 nm in pore throats), while the more carbonate-rich samples possess a more prevalent

amount of intragranular and intergranular pores ($\sim$ 100 nm in pore throats). Mineralogically speaking, carbonate and clay have an inverse relationship, as clay increases carbonate decreases. Samples have a low connectivity for the hydrophilic pore network but high for the hydrophobic pore network. From pyrolysis, S1 shows a positive correlation with MICP porosity. However, the Utica Shale and Point Pleasant Formation show a negative correlation suggesting OM may play a negative role in porosity development. Carbonate is not a controlling factor but influences overall porosity. When compared to other unconventional reservoirs, the Utica Play shows similar traits of hardness, brittleness, organic richness, porosity and permeability as other successful unconventional plays. For the Utica Play, this study provides a better understanding of pore structure and how thermal maturity can reduce porosity in mature samples due to the infilling of bitumen and mineralogy, specifically carbonate, influence porosity. Our mineralogy, petrophysical, and geochemical results support the Point Pleasant Formation being the target of the Utica Play. The better sustain production rate of Well B compared to Well A could be due to the more favorable petrophysical and geochemical properties of the Point Pleasant Formation. Knowing the petrophysical and geochemical characteristics of the Utica Play could aid in well placement, well design, and hydraulic fracture design and optimization.

Table of Contents

List of Illustrations

List of Tables

Chapter 1: Introduction

1.1 Introduction

Part of the Appalachian Basin, the Utica Play includes the Late Ordovician strata of Utica Shale, Point Pleasant, and the organic-rich Logana member of the Lexington/Trenton Limestone (Figure 1-1) (referred herein collectively as Utica Play unless specified for each interval) each with its own characteristics (EIA, 2016). Covering Ohio, West Virginia, Pennsylvania, and New York, the Utica Play spans 60,000 square miles. Both the Utica and Point Pleasant Formations are favorable for the accumulation and production of hydrocarbons, but the Point Pleasant formation is more often targeted because it is more productive (EIA, 2016). The Lexington Limestone, which lies below the Point Pleasant formation, has also been a target for the play, but is not as extensive as only the Logana member proves to be organic rich. Changes in maturation level as these formations become deeper to the east have resulted in roughly parallel trends of oil, wet gas and dry gas production (Patchen and Carter, 2015) as seen in Figure 1-2. Samples were obtained from low maturity in central Ohio to high maturity in eastern Ohio (Figure 1-2). Most of the oil and gas exploration and development has been focused in eastern Ohio where the Utica Play is shallower, meaning it is relatively less expensive to drill.

The Utica Play was first discovered in 2004 by Range Resources. In 2012, USGS originally estimated the reserves containing 940 MMbo and 38 Tcf gas. As of mid-2015, the Appalachian Oil and Natural Gas Research Consortium in West Virginia University calculated the Utica Play to contain 1960 MMBO and 782.2 Tcf gas (Patchen and Carter, 2015), nearly 20 times as much technically recoverable natural gas resource than previously thought by the USGS in 2012. Shale production in Ohio has increased from 2.5 Bcf in 2011 to 452 Bcf in 2014. In October 2015, operators were producing more than 3 Bcf/d in Ohio (EIA 2016). Per Ohio Department of Natural Resources (ODNR), there are 2,134 drilled wells and 2,634 permits as of 10/8/17 since September of 2010.

One of the current issues with unconventional reservoirs is the problem of sharp production decline. In the past decade wells have either been plugged or re-fracked to face this problem, but would only see a short production peak followed by the same sharp decline in production. New wells are being drilled just to maintain oil and gas production and be economical. The sharp decline coupled with the low recovery rates have caught the attention of the oil and gas industry.

The current recovery factor for oil and gas are 3% and 28% for the Utica Play in Ohio (Patchen and Carter, 2015). The low recovery rate and steep production decline in tight formations are partly limited by diffusive hydrocarbon transport in the poorly-connected pore spaces. Despite this steep decline and low overall recovery in shale hydrocarbon development, investigations into their root causes are surprisingly scarce (Hu and Ewing, 2014).
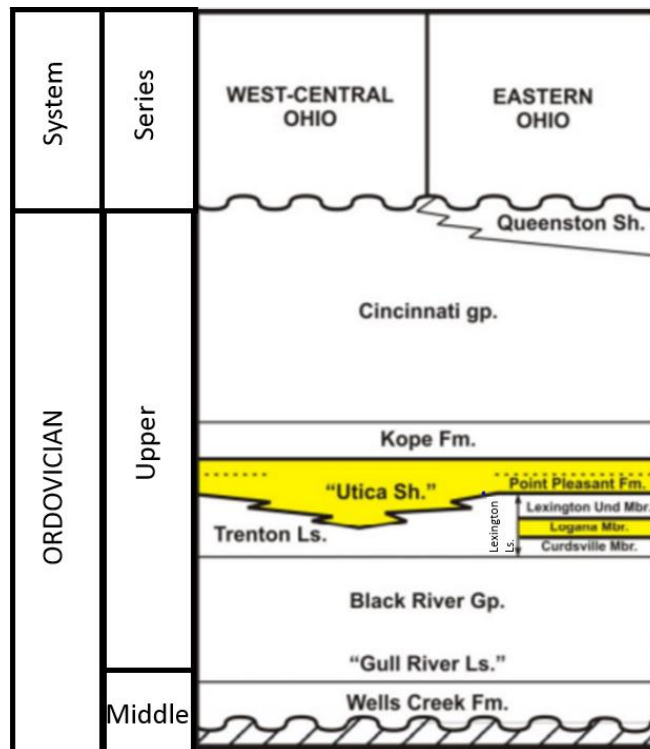
Figure 1-1 General stratigraphic column of the Upper Ordovician strata for west-central Ohio and eastern Ohio. Highlighted in yellow is the target potential of the Utica Play which includes the Utica Shale along with Point Pleasant Formation and the Logana Member of the Lexington Limestone (modified from Patchen et al., 2006)

In this work, both drilling cuttings and core samples were obtained from several locations (Figure 1-2) for several strata. From the wells Prudential #1-A and Cadiz B4H-14, samples were only obtained for stratum Utica Shale, for wells A and B samples (provided from a company, with the well names not revealed) were obtained for all members of the Utica Play, and additionally the Kope formation in Well A.
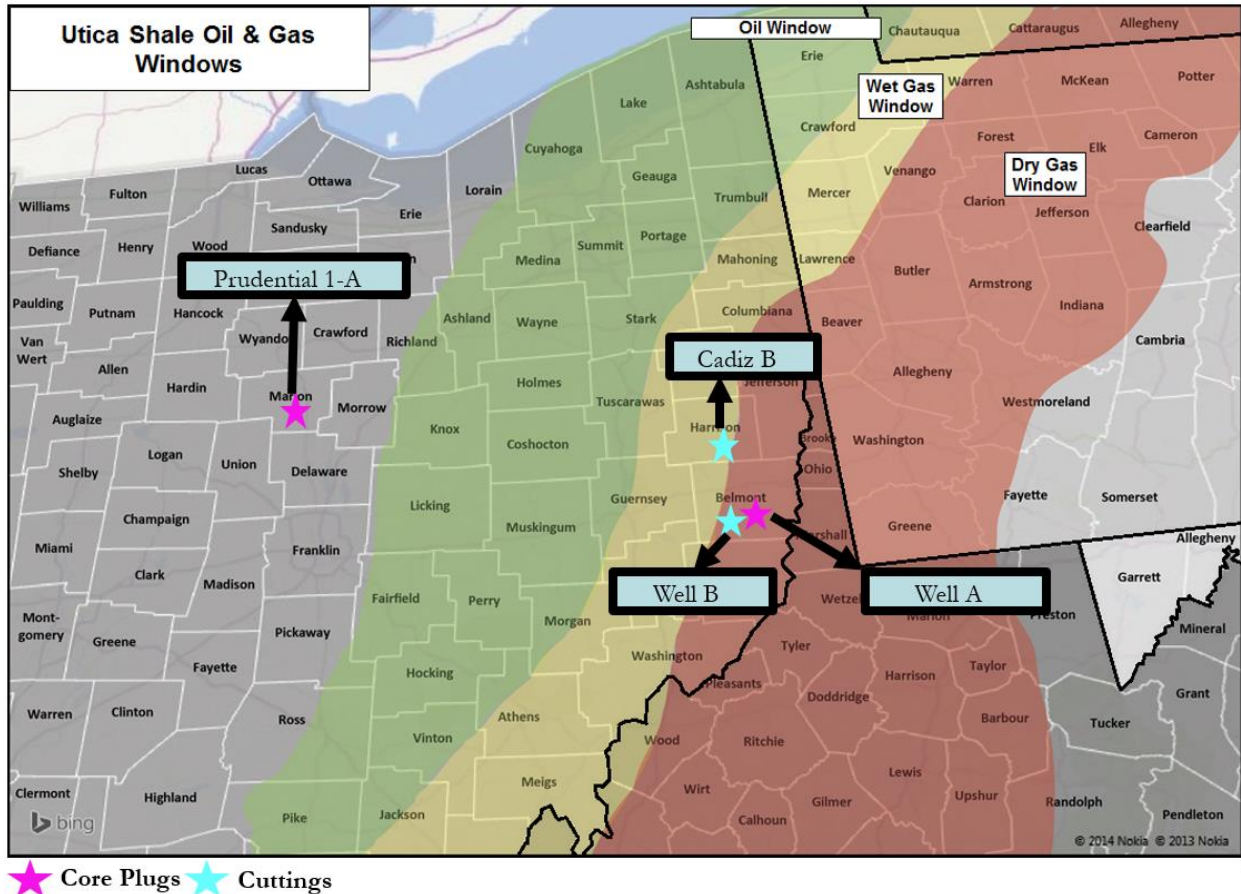
Figure 1-2 Map showing oil and gas windows in Eastern Ohio, Western Pennsylvania, and West Virginia. The stars show where samples were obtained along with the well name. Purple stars denote core plug and the blue stars denote cuttings (modified from NGI, 2017)

1.2 Literature Survey and Our Objective of Study

As the Utica Play has been receiving a lot of attention over the past five years due to the substantial amounts of natural gas and oil it yields, an increase of research has been conducted on this

play to get a better understanding of its geological characteristics of the play. Some research was done on the Late Ordovician strata, as summarized in "The Geologic Play Book for Utica Shale Appalachian Basin Exploration" coordinated by the Appalachian Oil & Natural Gas Consortium and the West Virginia University Shale Research, Education, Policy and Economic Development Center by Patchen and Carter (2015). This play book incorporates and integrates results of inorganic geochemistry (bulk mineralogy, carbonate content, and carbon isotopes), source rock geochemistry (TOC analysis, Rock Eval, organic petrography & thermal maturity), porosity and permeability (pore imaging, CT X-ray analysis, XRD, MICP, and helium pycnometry), and subsurface mapping and correlation through geophysical log analysis. According to Patchen and Carter (2015), three main objectives for the study were to:

1) Characterize and asses the lithology, source rock geochemistry, stratigraphy, depositional environment(s) and reservoir characteristics of Utica and equivalent rocks in the northern Appalachian basin

2) Define Utica oil and gas fairways by integrating regional mapping work with drilling activity and production tracking efforts

3) Provide production-based and volumetric Utica resource assessments informed by geologic and geochemical data collected during the course of this study.

Even with the large-scale of this study, the researchers were limited to five cores to analyze with most of their work performed on cuttings and well logs. Other research investigating the pore structure and petrophysical properties of the Utica Play include the following: Ismail and Zoback (2016) evaluated the effects of mineralogy and pore structure play on the transport mechanisms using non-adsorbing gas on Utica and Permian shale samples. Brinkley (2016) characterized the Utica Shale/Point Pleasant about geochemical and geophysical properties for one well in Washington County, Ohio. Bai et al. (2016) studied the submicron pore characterization of the Ordovician Utica shale using MICP, XRD, Dispersive X-ray Spectroscopy, scanning electron microscopy (SEM), and FIB (focused ion beam)-SEM imaging to

4

determine pore size distribution, types of pores, and to provide three-dimensional tomography model. Chukwuma (2015) evaluated the pore structure and fluid migration pathways at the nano-scale using MICP, fluid imbibition and tracer migration, and laser ablation-inductively coupled plasma-mass spectrometry (LA-ICP-MS). Swift et al. (2014) characterized Utica Shale at nano- to micro scale using neutron scattering methods.

Of late, authors like Loucks and Reed (2014) and Ko et al. (2017) have been investigating the maturation and distribution of organic matter to determine the origins of nano-scale pores. Using both core and cuttings samples from 4 wells and different maturities, the objective of this study will focus on the pore structure and rock-fluid interaction with relation to the geochemical properties to assess the late Upper Ordovician strata by MICP, helium porosity and permeability, low-pressure nitrogen gas physisorption, spontaneous imbibition and contact angle tests (petrophysical attributes), pyrolysis and TOC (geochemistry) and XRD (mineralogy).

Chapter 2: Geologic Setting and Hydrocarbon Potential of the Upper Ordovician Shale

2.1 Geologic Setting

The Appalachian Basin is an elongate, asymmetric foreland basin that is about 230,000 mi^2 in area. It can be more than 1,000 miles long and as much as 350 miles wide (Witt, 1993), and is an oblong sedimentary basin extending from southeastern Ontario and Southern Quebec to northeastern Alabama (Ettensohn, 2008). The basin is filled with Paleozoic rock ranging in age from Early Cambrian to Early Permian, with a preserved thickness of 600-900 m on its western flank and to more than 13,700 m on its eastern flank (Ettensohn, 2008). As seen in Figure 2-1, the Appalachian Basin is bounded by the eastern flank of the Cincinnati, Findlay, and Algonquin arches and is bordered on the east by metasedimentary, metavolcanic, and intrusive Precambrain and Paleozoic rocks of the Allegheny Front consisting of the Adirondack dome, Blue Ridge and New England Uplands. The northwestern boundary is defined by the

5

updip erosional limit of Paleozoic sediments along the Laurentian and Frontenac arches of the Canadian Shield in southeastern Ontario and southern Quebec. The Black Warrior Basin defines the transitional southern boundary.

The Appalachian Basin formed in response to tectonic loading during four orogenic events on the eastern margin of Laurentia/Laurussia during approximately 220 Ma from the Early-Middle Ordovician transition through Permian time (Ettensohn, 2008). The first Paleozoic orogeny, ~ 472 Ma, formed for nearly 200 Ma through the closure of the Iapetus and Rheic oceans. The tectonic loading during the growth of this orogeny of the crust generated the accommodation space for the Appalachian sedimentary record. The Allegheny orogeny was the highland at this time that acted as a sediment source, depositing sediments into the depocenter. The depocenter is roughly coincident with the Rome trough between northern West Virginia and central Pennsylvania suggesting that the position and configuration of the depocenter may, in part, have been controlled by the trough (Repetski et al., 2014).
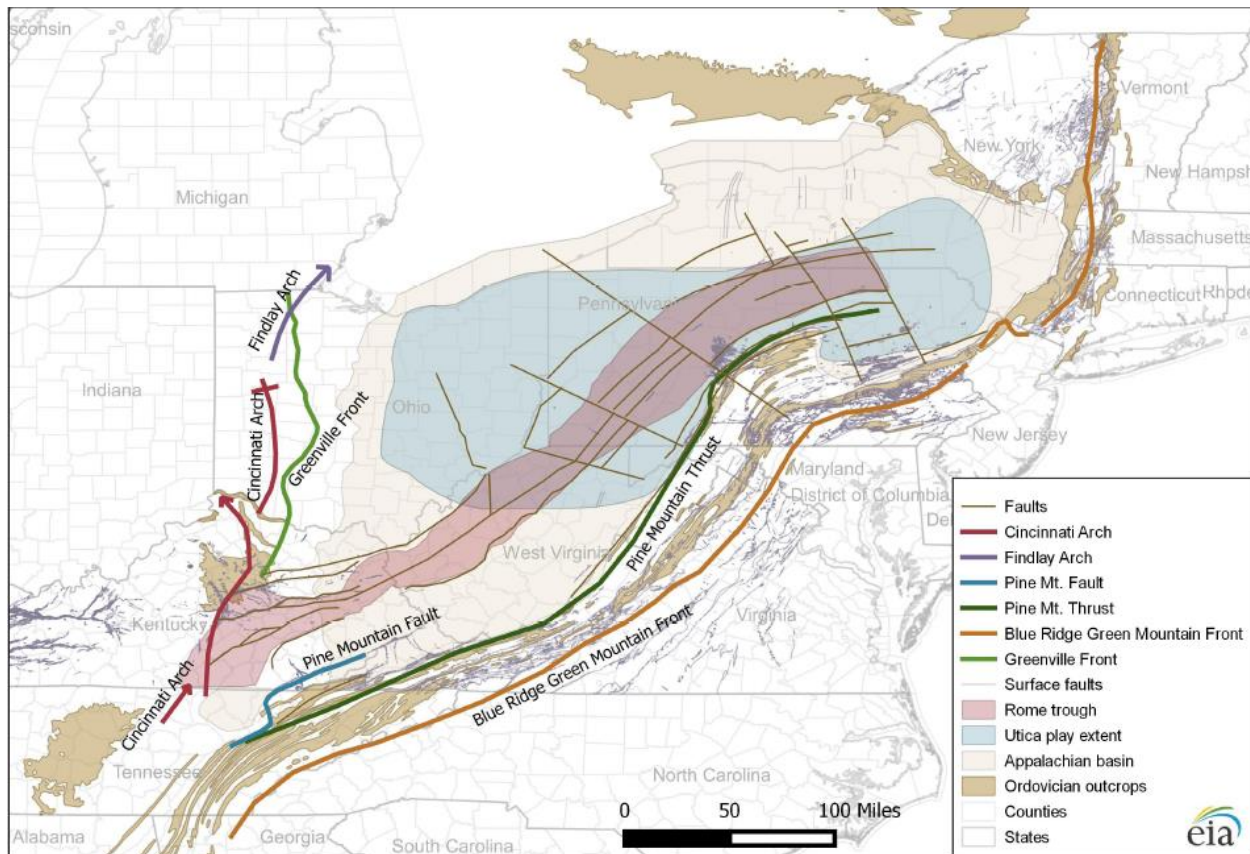
Figure 2-1 Major structural and tectonic features in the region of the Utica Play (EIA, 2016)

2.2 Stratigraphy of the Late Ordovician Shale

The stratigraphic succession of the Late Ordovician strata of the Appalachian Basin is a mixed carbonate-clastic system which includes the Kope, Utica Shale, Point Pleasant and Lexington/Trenton Formations (Figure 2-2). Trenton and Lexington are both formal formation names that have been applied to the same interval of rock (Patchen and Carter, 2015). The Point Pleasant Formation and the upper members of the Lexington/Trenton Formation have been the primary target and producing interval (Wickstrom, 2013; Patchen and Carter, 2015). This is due to the high TOC % and high carbonate content which is good for its fracability. Extensive research has been extended in surface exposure in areas of the Cincinnati Arch, Nashville Dome, and in Virginia, yet few published subsurface studies of the

Late Ordovician strata include the east Ohio region. Descriptions of each major lithologic unit, from top to bottom, of our studied strata are provided below in Sections 2.2.1 thru 2.2.4.
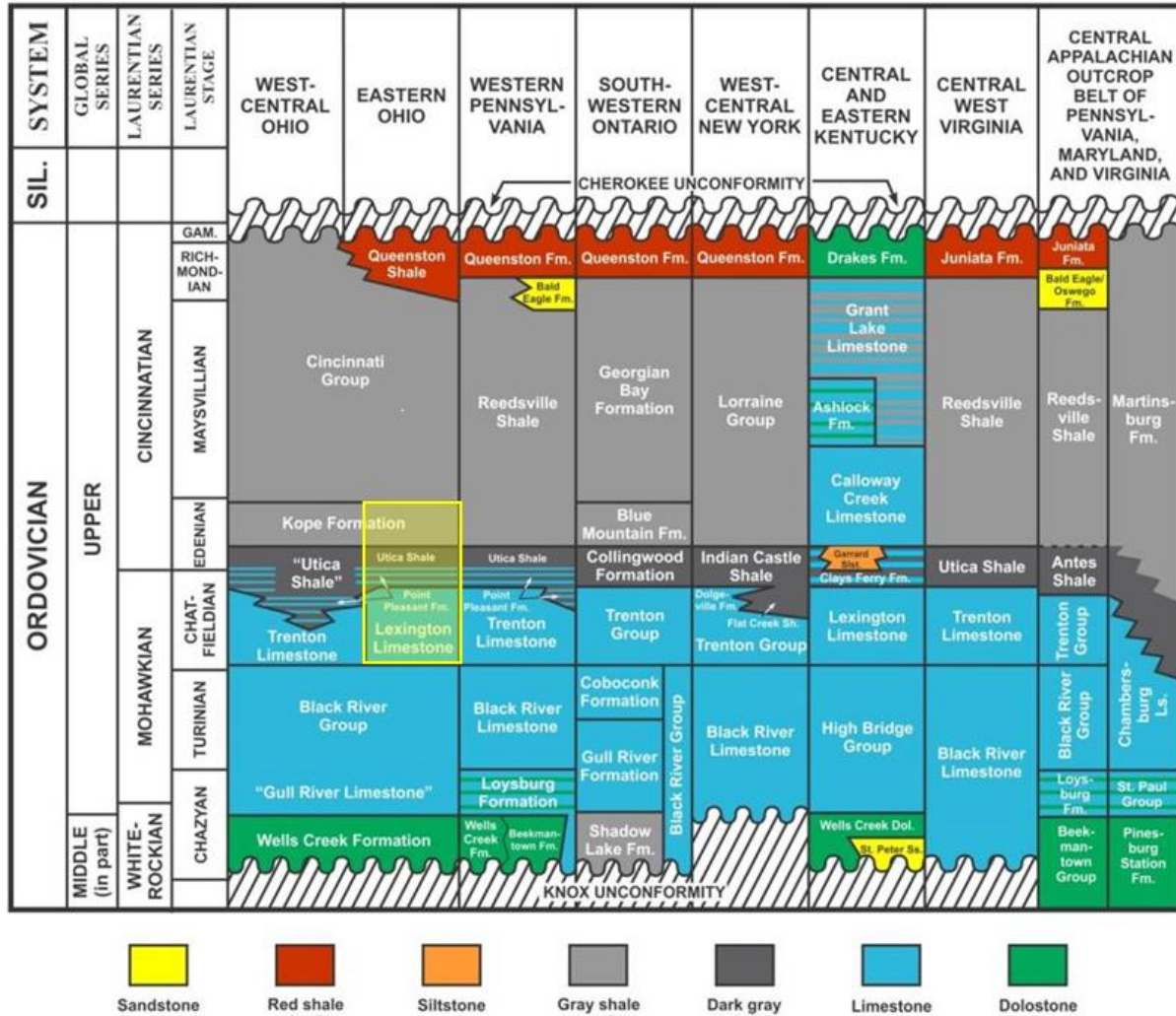
Figure 2-2 Regional correlation chart of Upper Ordovician strata. Studied intervals highlighted in yellow box. (modified from Patchen and Carter, 2015).

2.2.1 Kope Formation

The Kope Formation consists predominantly of soft, pale to medium gray, readily weathering mudstones or shales with very minor black or dark gray tongues, thin beds of light-gray siltstone or calcisiltite (Brett and Alego, 1999). This organic-poor shale and siltstone unit lies above the Utica Shale.

It is composed of interbedded shale (about 60 to 80%), limestone (20 to 40%), and minor siltstone (Patchen and Carter, 2015). This formation ranges in thickness from about 40 to 1600 ft with an average thickness of 200 ft. Equivalent units include the lower portion of the Calloway Creek Limestone of Kentucky, Lorraine Group of New York, and Reedsville Shale of Pennsylvania and West Virginia (Figure 2-2).

2.2.2 Utica Shale

The Utica Shale, which is Middle to Late Ordovician in age, consists largely of brownish-black to black marine shale with small amounts of gray shale, siltstone, or intercalated nodular argillaceous limestone (Witt, 1993). In eastern Ohio, the Utica Shale is a massive, fossiliferous, organic-rich, black to gray shale that ranges from 90 to 210 ft thick and interfingers and overlies the Point Pleasant Formation (Ettensohn, 2010). Moving eastward, the Utica thickens to about 400 ft in central New York. The Utica Shale was deposited as the basin continued to experience rapid subsidence on the western flank of the north-south trending Taconic Orogeny. The deepening water column becomes stratified, and the organic matter is buried and preserved as dark or black muds to result in oxygen-deprived (dysoxic or anoxic) environments (Ettensohn, 2008). This marine deposit was deposited throughout the Appalachian Basin and includes the equivalent facies: Athens Shale in Alabama, the Blockhouse Shale in Tennessee, the Paperville Shale in southwestern Virginia, the Antes Shale in Pennsylvania, the Utica Shale in central and eastern Ohio, and the Point Pleasant Formation in southwestern Ohio (Witt, 1993).

2.2.3 Point Pleasant Formation

The underlying Point Pleasant Formation in Ohio consist of interbedded light gray to black limestones, brown to black organic-rich calcareous shales (Wickstrom, 2013). This interval, where it exists, is equivalent to the lower Clays Ferry Formation of Kentucky and the lower Indian Castle Shale of New York (Patchen and Carter, 2015). The average carbonate content is about 40 to 60%. As it extends northward beneath the Utica Shale it is described being interbedded, fossiliferous limestone, shale and

minor siltstone. The thickness ranges from 0 ft in northwestern Ohio to 240 ft in northern Pennsylvania (Patchen and Carter, 2015). The Point Pleasant Formation appears to have been deposited in part contemporaneously with the Trenton Limestone in northwestern Ohio, but also appears to have been deposited over the Trenton along portions of the platform margin to the southwest (Patchen et al., 2006).

2.2.4 Lexington/Trenton Formation

The Trenton Formation is a light gray, crystalline, highly fossiliferous, skeletal grainstone. It lies above the Black River Group and below Utica Shale in Northwest Ohio (Figure 2-2). As the carbonate-platform deposits of the Trenton thin, the interbedded, organic-rich carbonates and shales of the Utica Shale and Point Pleasant thicken (Wickstrom, 2013). The Trenton Formation is correlative to the Lexington Formation as they accumulated on the edges of the Appalachian Basin as low relief carbonate buildups or platforms. It ranges from 40 feet thick in west-central Ohio to more than 300 feet thick in northwestern Ohio (Hansen, 1997). Stratigraphically, the carbonate platform is divided; such limestones are called the Trenton Limestone in northwestern Ohio or Lexington Limestone in southeastern Ohio.

The Lexington Formation consists of nodular and irregularly bedded fossiliferous limestone and shale (Patchen and Carter, 2015), which consists of three different members: Lexington Undifferentiated Member, Logana Member, and the Curdsville Member. The Lexington Undifferentiated Member is considered a cleaner limestone with abundant fossils such as bryozoans, brachiopods, mollusk and trilobite, and are abundant in whole and broken fragments. The Logana Member is organic-rich and represents an interbedded calcisiltite, shale and coquinoid limestone (Patchen and Carter, 2015). The basal strata of the Lexington Limestone are the Curdsville Member which is organic-poor and carbonate rich. The Lexington platform is a deeper water platform than the Trenton platform in northwestern Ohio as indicated by more argillaceous material and a more gradational upper contact with the overlying Point Pleasant (Patchen et al., 2006).

2.3 Central Appalachian Basin Architecture and Deposition during Ordovician

During the Ordovician, Ohio was in southern tropical latitudes and dominated by warm, shallow

seas (Hansen, 1999). Major structural changes occurred during the collision between the North

American and European continents during the Middle Ordovician which form a series of island arcs and

mountains to the east of Ohio. The Early-Middle Ordovician transition is commonly represented by a

major unconformity, which has been interpreted to represent the initiation of convergence on the new

Laurentian margin and ongoing closure of the Iapetus Ocean (Ettensohn, 2008) known as the Knox

unconformity. This is the base of Ordovician strata. The widespread Knox unconformity, an episode of

emergence and erosion of the carbonate platform, was formed when the land surface bulged upward

(known as a peripheral bulge), accompanying development of a foreland basin to the east at the edge of

the orogenic belt (Hansen, 1999; Ryder, 1998). The western margin of the Rome Trough is controlled by

a system of down-to-the-east extensional basement faults, across which abrupt eastward thickening of

carbonates occurs. The northwest boundary fault system of the Rome trough continued to control

subsidence during this time but with diminished effect of sedimentation and depositional patterns as

compared to the early Cambrian (Patchen and Carter, 2006).

During the Middle/Late Ordovician time the architecture evolved into a broad, stable, shallow-

water carbonate ramp as the seas transgressed much of the area. Thick, shaly-carbonates were

deposited within the Rome Trough coming into existence as the depocenter for the Appalachian Basin.

During the late Ordovician time the central Appalachian basin architecture continued to evolve with the

appearance of low-relief carbonate buildups of the Trenton and Lexington platforms surrounding the

interplatform Utica/Point Pleasant sub-basin (Patchen et al., 2006; Figure 2-3). As clean carbonates were

being deposited on shallow-water platforms, interbedded limestones and shales were simultaneously

being deposited within the inter-platform sub-basin (Figure 2-4). During deposition of the Utica Shale,

the intensity of the Taconic orogeny once again increased causing a rapid rise in sea level or increased

subsidence of the region resulting in the Utica Shale replacing carbonate deposition on the platform

(Patchen et al., 2006).
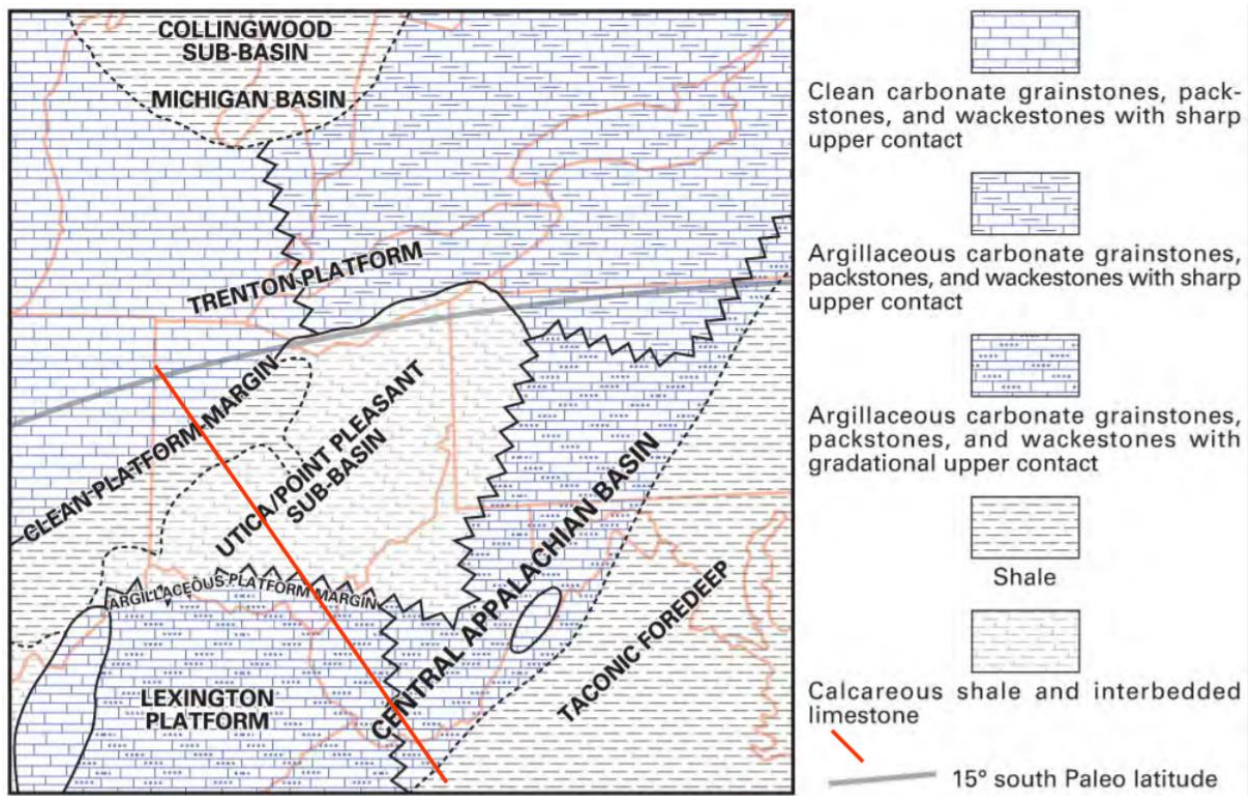
Figure 2-3 Facies map of Trenton/Point Pleasant time (from Wickstrom, 2012)
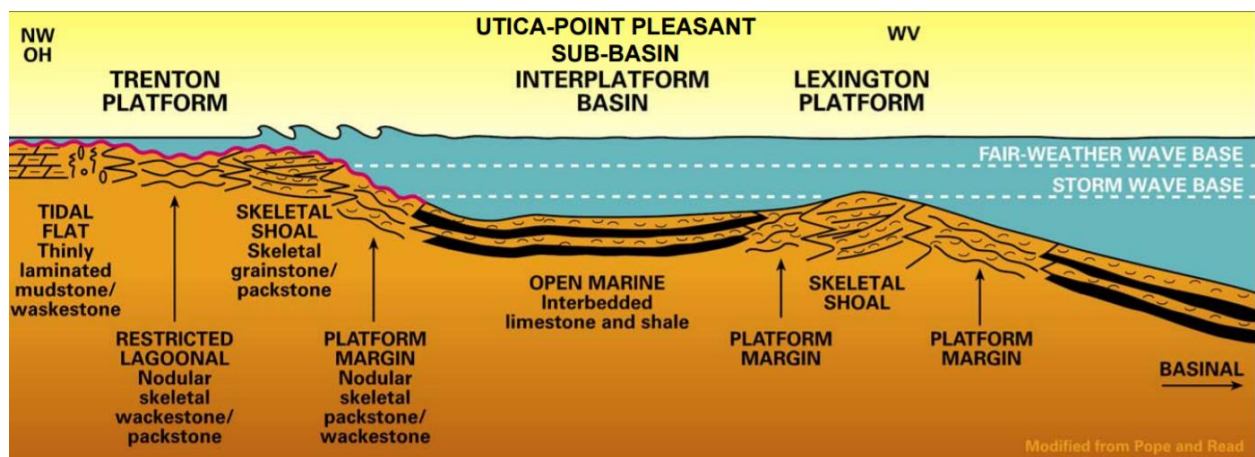
Figure 2-4 Cross section from transect line above (NW Ohio – West Virginia) displaying depositional model with idealized platform and sub-basin with facies (from Pope and Read, 1997)

2.4 Petroleum Potential of the Upper Ordovician

The Utica Play has been known to be a source rock for over 100 years (Orton, 1899; Wallace and Roen, 1989; Witt, 1993; Ryder, 1998) and is now being drilled as an unconventional reservoir. Even though most refer to this as the Utica Play, the Point Pleasant Formation is the primary target and producing interval (Wickstrom, 2013). This is because the Point Pleasant Formation when compared to the Utica, has a lower clay content, higher organic content, better porosity, and more favorable rock properties. Several thermal maturation indicators (T_{max}, Ro, Production Index, Conodont Alteration Index) show that the Utica Play in Ohio transitions from the oil window in western Ohio to dry gas in eastern Ohio. Burial- and thermal-history models indicate that the Utica Shale in eastern Ohio entered the oil-generation window approximately between Late Devonian and Late Pennsylvanian time and entered the gas-generation window between Middle Mississippian and Early Permian time (Rowan, 2006; Ryder, 2014).

2.4.1 Thermal Maturity

Thermal maturity is one of the most important parameters when evaluating an oil and gas play. Vitrinite reflectance (%Ro) is commonly used as a thermal maturity indicator. Vitrinite reflectance is a direct microscopic measure made on the macerals extracted from the kerogen in the source rock but is dependent on kerogen type and cannot be measured in rocks that lack vitrinite. Rowan (2006) defined that Ro % values < 0.6 are immature source rock, Ro % values between 0.6 to 1.2 are in the oil window, and Ro % values > 1.2 are in the gas window. Figure 2-5 shows the progression of vitrinite reflectance from west to east in Ohio. In western Ohio, Ro % values are less than 0.6%, in central Ohio range from 0.6-0.8%, and in eastern Ohio range from 0.8-1.9%. In western Ohio there are immature oil prone source rock and moving eastward the Utica Play grades into mature gas-prone source rock.

Figure 2-5 Calculated %Ro average value per well and %Ro values of the Upper Ordovician Shale Interval in Ohio (from ODNR, 2013)

2.4.2 Conodont Alteration Index (CAI)

The conodont alteration index (CAI) is an important criterion for estimating the thermal maturity of Ordovician to Mississippian rocks in the Appalachian basin. CAI is based on color changes seen in microscopic-sized fossil teeth from the remains of eel-shaped chordates (Patchen and Carter, 2015). These fossils are highly resistant to weathering and high temperature regimes, and are both time and temperature dependent. When comparing against a set of conodont color standards the CAI can be obtained. The onset of oil generation is placed between 1.0 and 1.5, limit of oil generation is between 2.0 and 2.5, and dry gas is generally associated with CAI values in excess of 2.5 (Harris, 1979; Patchen and Carter, 2015). Using CAI to estimate thermal maturity, Patchen and Carter (2015) defined CAI max

isograds (Figure 2-6) which also displays the trend of increasing thermal maturity in Ohio increasing to

the east. In central Ohio the maximal CAI values are 1.0 (i.e. the onset of oil generation) and moving

eastward CAI max values are up to 4.0 in southeastern Ohio which is associated with dry gas.
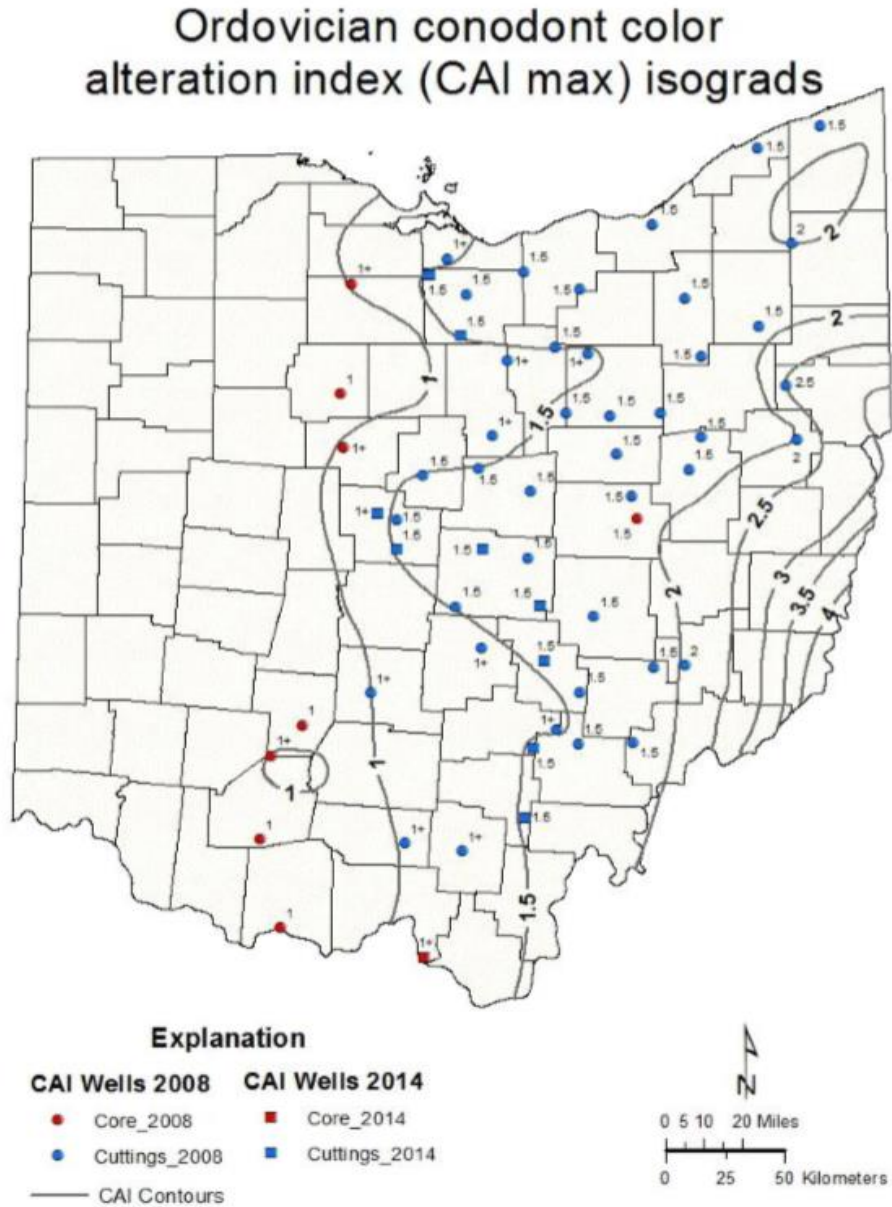
Figure 2-6 Map of CAI for the Upper Ordovician shale in Ohio (from Patchen and Carter, 2015)

2.4.3 Total Organic Carbon (TOC)

The Utica shale is characterized by type II kerogen, which is a variety of kerogen that is typically prone to oil generation (Ryder, 2014). Maximum TOC values for the Upper Ordovician shale interval range from poor TOC values as low as 0.1% in south-central Ohio to excellent TOC values > 4.0% in central and eastern Ohio (Figure 2-7). The average TOC value is up to 3.5% for the Utica Shale, 4 to 5% for the Point Pleasant Formation, and high as 4 to 5% for the upper Lexington/Trenton with TOC (Patchen and Carter, 2015).
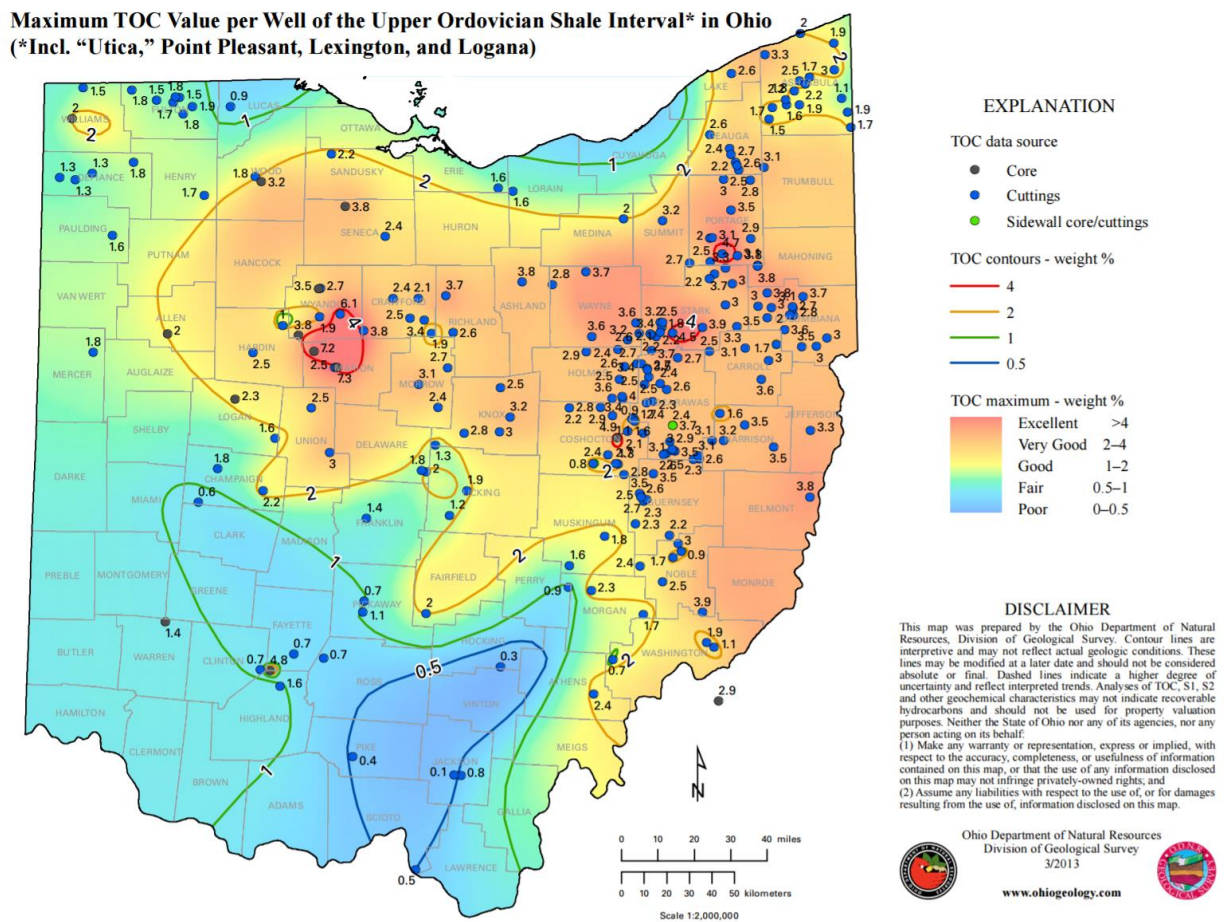
Figure 2-7 Maximum TOC values of the Upper Ordovician Shale interval in Ohio (from Ohio DNR, 2013)

Chapter 3: Methods

3.1 Acquisition of Samples

As the target of the study, the upper Ordovician shale and limestone consisting of Kope, Utica Shale, Point Pleasant, and the Lexington Limestone Formations, with a focus on the calcareous organic-rich black Utica Shale. Samples were obtained from a variety of maturity levels from the counties of Marion, Harrison, and Belmont in Ohio (Table 3-1; Figure 1-2).

Table 3-1 Sample Information

Well Name	Depth (ft)	Formation	Sample ID	Sample Type	Maturity (Ro, %)	Producing
Prudential #1-A	1144	Utica	P1144-U	Core Plugs	Low (0.64)	N/A
	1235		P1235-U			
	1336		P1336-U			
Cadiz B 4H-14	8500-8540	Utica	CB8500-U	Cuttings	High (~1.4)	Oil and Gas
	8600-8650		CB8600-U			
	8670-8700		CB8670-U			
Well A	9930	Kope	KS9930-K	Core Slabs	High (~1.8)	Gas
	10121	Utica	KS10121-U			
	10150	Point Pleasant	KS10150-PP			
	10230	Lexington Limestone	KS10230-LL			
Well B	10150	Utica	KB10150-U	Cuttings	High (~1.8)	Gas
	10180		KB10180-U			
	10210	Point Pleasant	KB10210-PP			
	10240		KB10240-PP			
	10270		KB10270-PP			
	10300		KB10300-PP			

		10330		KB10330-PP			
		10360		KB10360-PP			
		10390		KB10390-LL			
		10420		KB10420-LL			
		10450	Lexington Limestone	KB10450-LL			
		10480		KB10480-LL			
		10510		KB10510-LL			

To investigate how maturation and mineralogy control pore-throat size distribution and if nonwetting and small pore sizes reduce fluid migration, samples were obtained with various thermal maturities within the Utica Shale and subsequent Ordovician strata. Core samples from the Utica Shale in Ohio were obtained from the Horace R. Collins Core Lab Facility through the Ohio Geological Survey located in Columbus, Ohio, as well as an oil company whose name and name of wells shall remain confidential. From the Ohio Geological Survey, samples from following two wells were obtained: Prudential #1-A (API number 34101201960000) located in Marion County, and Cadiz B 4H-14 (API number 34067211990000) located in Harrison County. From the oil company, samples from two wells were obtained: Well A and Well B, both are located in Belmont County (Figure 1-2). Moving from Marion to Harrison to Belmont Counties, samples increase in thermal maturity. Prudential #1-A has the lowest maturity of the samples with a Ro of 0.64 % and samples from Well A and B have the highest maturity of Ro ~ 1.8 %. Core plugs of the Utica Shale were received from well Prudential #1-A at the depths of 1144', 1235', and 1336' (Table 3-1; Figure 3-1). Cadiz B 4H-14 is in the high maturity range with Ro ~ 1.4 %, with its cuttings received of the Utica Shale at the depth intervals of 8500'-8540', 8600'-8650, and 8670'-8700' (Table 3-1; Figure 3-2). From Well A, core slabs were received from the following strata: Kope Formation, Utica Shale, Point Pleasant, and the Lexington Formation at the depths of 9930',

10121', 10150', and 10230' respectively (Table 3-1; Figure 3-3). From Well B, cuttings were received

from depths of 10150'-10510' every 30 feet from the following strata: Utica Shale, Point Pleasant, and

the Lexington Formation (Figure 3-4). Once core samples were received they were prepared to

numerous sizes to be performed with the following laboratory experiments: helium porosity and

permeability (2.5 cm in diameter x >2.5 cm in height), MICP (1-cm sided cube; and sometimes GRI +,

GRI), low pressure nitrogen gas physisorption (GRI), contact angle (1cm in width x 1 cm in length x 0.3

cm in height), imbibition (1-cm sided cube), TOC (<75 µm), pyrolysis (<75 µm) and XRD (<75 µm). GRI+

are of the size fraction of 1.77 to 2.36 mm and GRI (Gas Research Institute; Guidry et al., 1995) are of

the size fraction of 500 to 850 µm; both names of GRI+ and GRI are used internally for sample sizes.
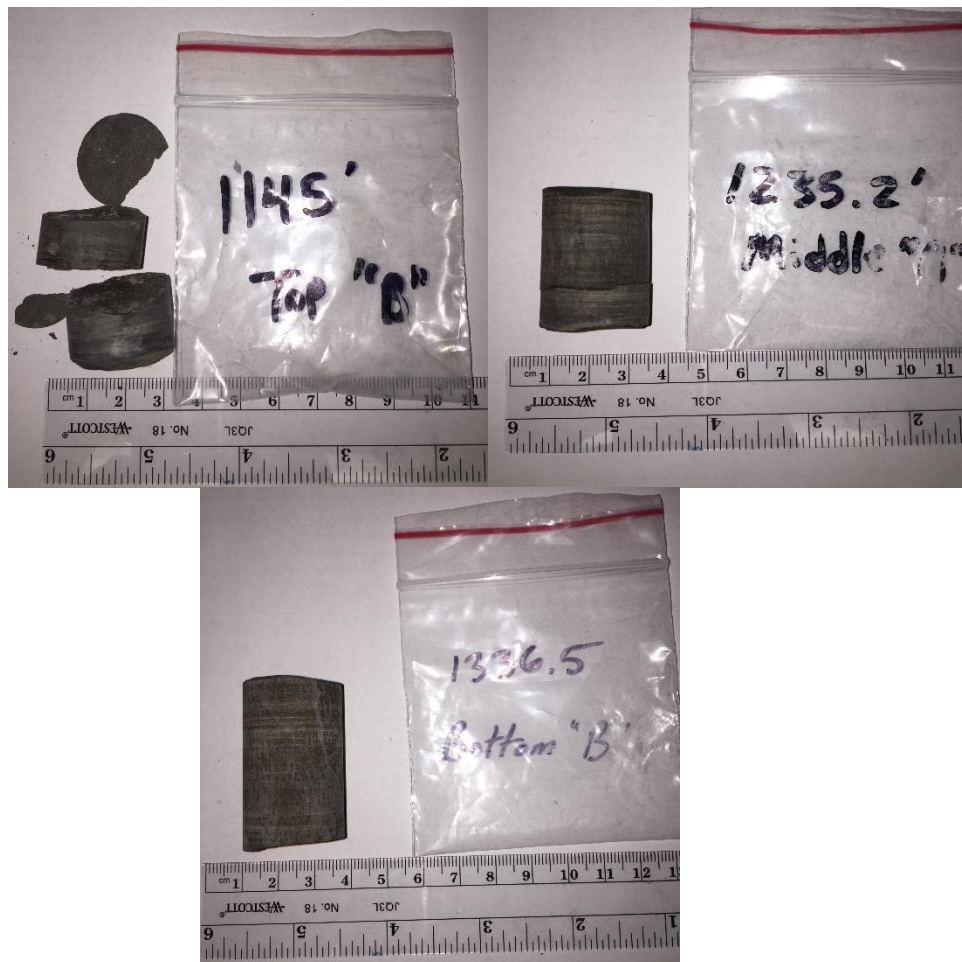
Figure 3-1 Photos upon arrival of Prudential #1-A. Top left is a core plug from depth 1145'. Top right is a core plug from depth 1235'. Bottom middle is a core plug from depth 1336'
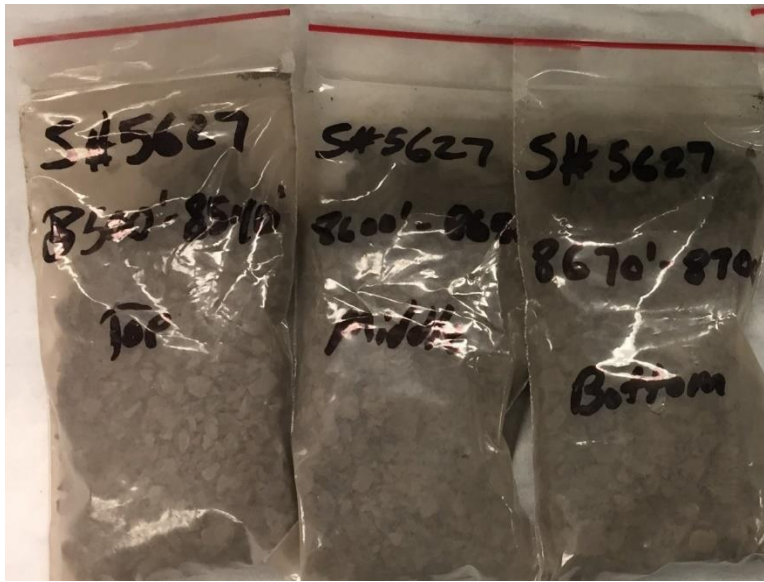
Figure 3-2. Photo upon arrival of cuttings from Cadiz B 4H-14.

A) KS9930-K

B) KS10121-U

C) KS10150-PP

D) KS10230-LL

Figure 3-3 Photos upon arrival of core slabs from Well A

A) KB10150-U
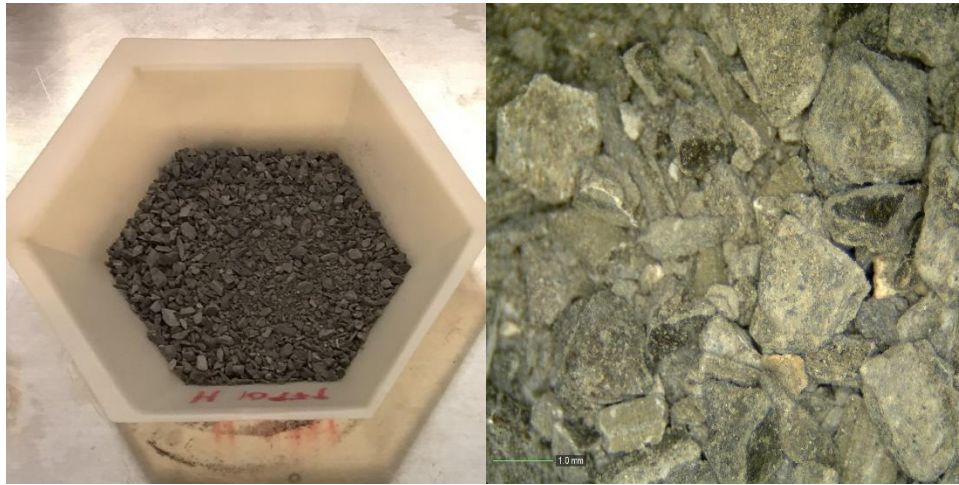
B) KB10180-U

C) KB10210-PP

D) KB10240-PP
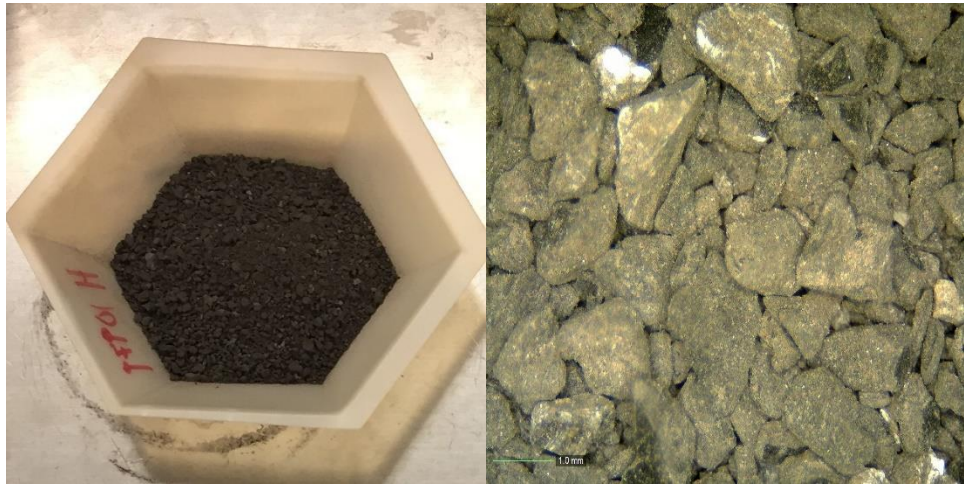
E) KB10270-PP
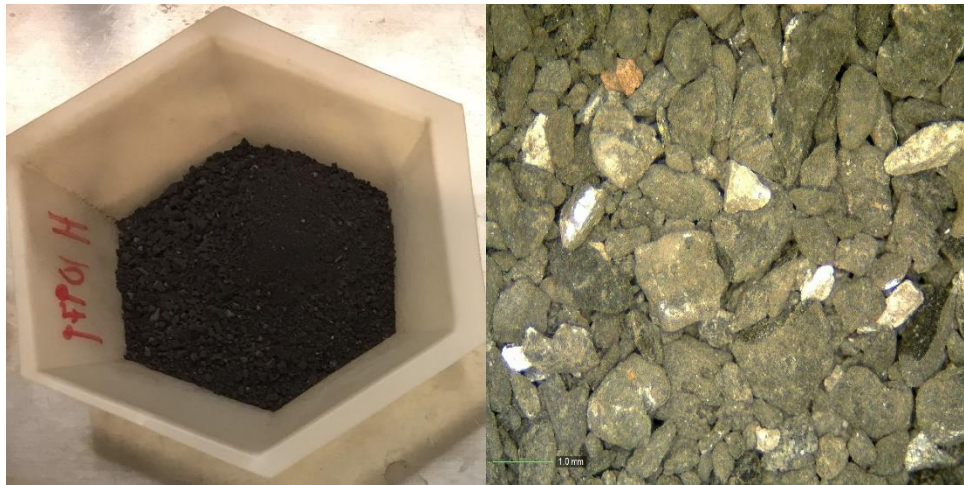
F) KB10300-PP
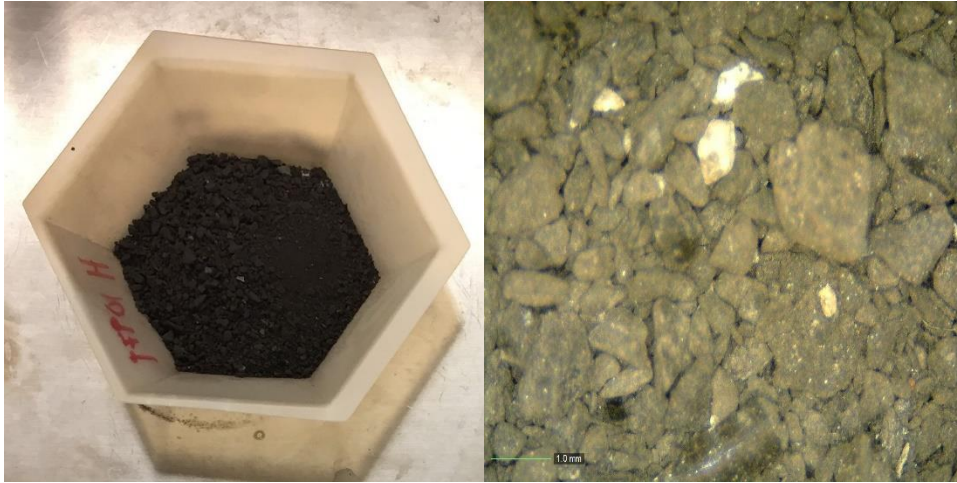
G) KB10330-PP
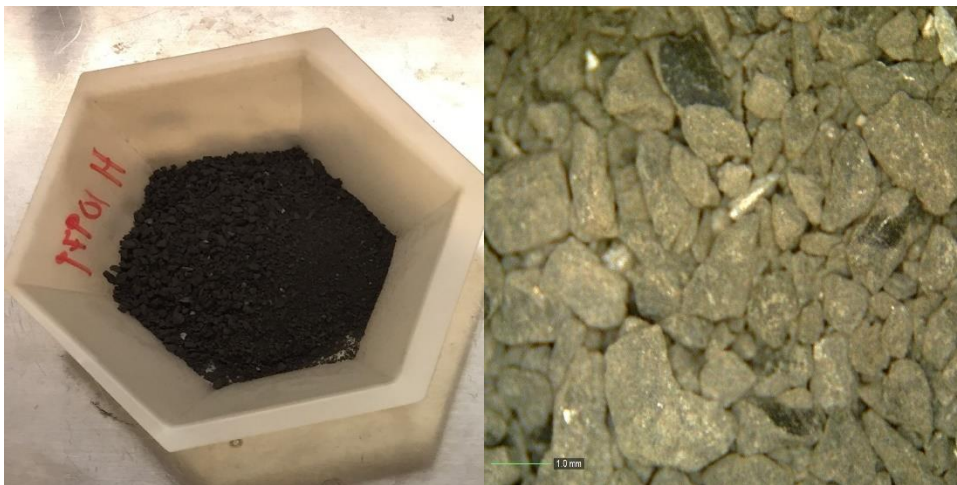
H) KB10360-PP

I) KB10390-LL

J) KB10420-LL

K) KB10480-LL

L) KB10510-LL

M)

 Figure 3-4 Sample photos upon arrival from Well B. Left photo is zoomed out. Right photo is zoomed in.

3.2 X-Ray Diffraction (XRD)

X-Ray Diffraction (XRD) analysis was performed on all samples. Using MAXima_X XRD-7000

(Figure 3-5) at Shimadzu Center for Environmental, Forensics and Material Science (CEFMS) Laboratory

located at University of Texas at Arlington (UTA). XRD is used to identify minerals and obtain the bulk

composition of sample, and the methods and procedures from CEFMS laboratory is provided in

Appendix A.

Figure 3-5 Shimadzu MAXima_X XRD-7000

3.3 Total Organic Carbon (TOC)

Total Organic Carbon (TOC) was derived from the Total Inorganic Carbon (TIC) and Total Carbon

(TC), which were performed at CEFMS Laboratory of UTA with Shimadzu TOC Vws SSM-5000A (Figure 3-

6). TOC was performed on all samples except for Well B. The methods and procedures from CEFMS

Laboratory is provided in Appendix B. Equation 3-1 is used to calculate the TOC %.

TC % - TIC% = TOC %   (3-1)

Figure 3-6 Shimadzu TOC Vws SSM-5000A

3.4 Pyrolysis

Pyrolysis was performed on all samples. This analysis was performed at our collaborating

institute, China University of Geosciences (CUG) with an instrument OGE-V (Figure 3-7) manufactured by

RIPED (Research Institute of Petroleum Exploration and Development of PetroChina). Pyrolysis analysis

identifies the type and maturity of organic matter as well as the quality of hydrocarbons in samples. The

analysis is performed by a controlled heating of the sample as the organic matter decomposes in the

absence of air. Tissot and Welte (1984) described the following basic parameters to be obtained from

pyrolysis analysis:

- S1 = the amount of free hydrocarbons (HC) in sample (mg HC/g);

- S2 = the amount of hydrocarbons generated through thermal cracking of nonvolatile organic matter. This parameter is an indication of the quantity of hydrocarbons that the rock has potential of producing should burial and maturation continue (mg HC/g);

- S3 = the amount of CO_2 produce during pyrolysis of kerogen. This parameter is an indication of the amount of oxygen in the kerogen (mg CO_2/g);

- S4 = the residual carbon content of sample (mg C/g)

- T_{max} = the maximum temperature reached from S2 (°C).

From these basic parameters, the type and maturity of organic matter can be determined. The hydrogen index (HI) is the ratio of S2 hydrogen to TOC (Equation 3-2) and is used to characterize the origin of organic matter. The oxygen index (OI) is the ratio of S3 to TOC (Equation 3-3), and measures the oxygen richness of sample. The production index (PI) is the ratio of already generated hydrocarbons to potential hydrocarbons (Equation 3-4). The PI increases with depth and associated hydrocarbon generation, and can be a good indicator for maturity of sample.

$$HI = \frac{S2}{TOC} \times 100 \qquad (3\text{-}2)$$

$$OI = \frac{S3}{TOC} \times 100 \qquad (3\text{-}3)$$

$$PI = \frac{S1}{S1+S2} \qquad (3\text{-}4)$$

The procedure for pyrolysis from Weatherford can be found in Appendix C for information. The instrument OGE-V measures S4 instead of S3 because this instrument does not have the sensor capable of measuring S3, like the commonly used Rock-Eval instrument. Instead, this instrument has the sensor to measure S4 during the oxidation to measure the residual organic carbon.

Figure 3-7 Instrument OGE-V for pyrolysis analysis

3.5 Mercury Injection Capillary Pressure (MICP)

The MICP approach utilizes the non-wetting mercury to invade pore throats by overcoming the applied capillary pressure of up to 60,000 psia (414 MPa). Pore structure characterization of samples includes the direct measurement of porosity, particle and bulk density, pore-size distribution, and median or mean pore diameters (Hu and Ewing, 2014). This method can also indirectly determine broader pore characteristics, such as total pore surface area, permeability, and tortuosity (Micromeritics, 2001; Hu and Ewing, 2014). The University of Texas at Arlington and Nanjing University (NJU) possesses the MICP instrument (Micrometrics Autopore IV 9510, Norcross, GA; Figure 3-8).

Mercury, a non-wetting fluid to most porous media, will not invade pores unless an external pressure is applied. The diameter of pore-throats invaded by mercury is inversely proportional to the applied pressure; the higher the applied pressure, the smaller are the pores invaded by mercury (Hu and Ewing, 2014). Washburn (1921) expressed this in the equation he developed (Washburn Equation) assuming all pore are cylindrical and the opening is circular in cross-section (Equation 3-5).

$$\Delta P = -\left(\frac{-2\gamma \cos\theta}{R}\right) \tag{3-5}$$

Where,

ΔP – difference in pressure across the curved mercury interface (psia);

γ – surface tension for mercury (dynes/cm);

θ – contact angle between the porous medium and mercury (degrees);

R – corresponding radius of the pore throat (cm).

Prior to Wang et al. (2016), Equation 3.5 assumed a constant value for both contact angle and surface tension. Wang et al. (2016) found that the contact angle of mercury in a circular pore increases exponentially as pore size decreases. As mercury starts to invade pores less than 5 nm, varying values for contact angle and surface tension are proposed. The contact angle varies with pore size, geometry, and temperature (Wang et al., 2016). A new modified Washburn equation is displayed below (Equation 3-6) and Wang et al. (2016) explained how they derived their new equation.

$$\Delta P = -\left(\frac{2\gamma_{Hg}(R)*\cos\theta_{Hg}(R)}{R}\right) \tag{3-6}$$

Where,

γ_{Hg} and θ_{Hg} are functions of R instead of being constant.

During the sample analysis, the MICP collects the data of applied pressure and incremental intrusion volume at that specific pressure (Gao and Hu, 2013; Hu and Ewing, 2014). Assuming all shale pores are cylindrical, the Washburn equation is unrealistic assumption in nature but applicable in petrophysics.

From the applied pressure and intrusion volume obtained from the MICP analysis we can indirectly obtain permeability. Katz and Thompson (1986;1987) derived an equation (Equation 3-7) that calculates permeability based on MICP data:

$$k = \frac{1}{89}(L_{max})^2 \left(\frac{L_{max}}{L_c}\right) \Phi S(L_{max}) \tag{3-7}$$

Where,

k – permeability (m^2);

L_{max} – pore-throat diameter at which hydraulic conductance is maximum (μm);

L_c – characteristic length which is the pore-throat diameter (μm) corresponding to the threshold pressure P_t (psia);

Φ – porosity of sample (fraction);

$S(L_{max})$ – mercury saturation at L_{max} (Gao and Hu, 2013).

Another important topological parameter is effective tortuosity which can be related to effective diffusion coefficient and travel distance of molecules. Hager (1998) and Webb (2001) developed Equation 3-8 which calculates tortuosity from the MICP data.

$$\tau = \sqrt{\frac{p}{24k(1+pV_{tot})} \int_{n=r_c,min}^{n=r_c,max} n^2 f_y(r_c) dr_c} \tag{3-8}$$

Where,

τ – tortuosity;

p – sample density ($^g/_{cm^3}$);

V_{tot} – total pore volume ($^{ml}/_g$);

$f_y(r_c)dr_c$ – volume probability density function (volume of pores with a radius in the range of r_c to r_c + dr_c per kg of dry material) (cm^3/g);

r_c min – minimum detectable capillary radius by MICP (μm);

r_c max – maximum detectable capillary radius by MICP (μm).

Compressibility and conformance need to be accounted for. Using a normal blank correction this can be corrected by completing an MICP experiment with an empty penetrometer. The apparent intrusion by the empty penetrometer due to mercury and penetrometer compressibility was found to be negligible when samples are added into the penetrometer to reduce mercury volume, as the compressibility (and hence apparent pore volume) mostly comes from mercury. When mercury is injected within crushed particles a certain pressure is required for mercury to fill all the voids between the particles (so called conformance effect) before entering the intra-particle pores (Tinni et al., 2014).

3.5.1 Procedure for MICP Test

Each sample is oven-dried at 60 °C for at least 48 hours to remove moisture, then immediately placed in the desiccator (~23°C) with less than 10% relative humidity to be cooled to room temperature. Once the sample is cooled, it is weighed and placed into a penetrometer, which is an apparatus consisting of a sample chamber connected to a metal precision-bore and glass capillary stem. Depending on sample size and porosity levels (GRI+, GRI, or 1-cm^3 cube), the appropriate penetrometer will need to be selected for the mercury change within the stem to be detectable. The sample is placed in sample chamber and then properly sealed. The penetrometer with sample inside is weighed again and placed into a low-pressure chamber where it is evacuated to 50 μm Hg (0.05 torr, 0.000972 psi, 6.7 pa or

99.993% vacuum). This evacuation process removes air and/or moisture that remains inside the sample. After the evacuation process, the mercury fills up the sealed sample cup to start low-pressure intrusion to a maximum filling pressure of 30 psia (0.21 MPa). Equilibrium time (the minimum time for mercury to stabilize within the sample before the next pressure is applied; the detection limit of the mercury volume intruded is < 0.1 µL) of 10 seconds is set for low-pressure analysis for shale samples. The mercury will first invade the sample surface-accessible pore throats with a diameter of about 50 µm, depending on penetrometer being used. Once the low-pressure analysis is completed, the penetrometer is removed and weighed again to account for the mercury inside the penetrometer to calculate the densities.

Next, the penetrometer is placed in the high-pressure chamber. The pressure is increased from 30 psia (0.21 MPa) up to 60,000 psia (414 MPa) with an equilibrium time of 30 seconds for pressure each step. Mercury can intrude pore throats as small as 2.8 nm at its highest pressure. Permeability and tortuosity can be calculated using the physical properties of mercury (interfacial tension), the contact angle between mercury and the sample, pore throat radii, and porosity (Gao and Hu, 2013; Hu and Ewing, 2014). One note about the MICP analysis is the overestimate of volume of smaller pores and an underestimate of larger pores; this phenomenon is called the ink-bottle effect. This is when large pores are connected by smaller neck entrances from the sample surface (Kaufman, 2010; Hu and Ewing, 2014), and need a higher pressure to be reached in order to pass through the initial small pore throat.

Figure 3-8 MICP apparatus of Micrometrics Autopore IV 9510

3.6 Helium Porosity and Permeability

The small gas molecule, helium, is utilized to simultaneously measure the permeability and porosity test at confining pressures up to 9950 psi over a wide permeability range (0.001 mD to > 10 D) (Coretest Systems, 2012). Helium porosity and permeability were conducted by Chengdu University of Technology (CDUT) using the AP-608 Automated Porosimeter-Permeameter (Figure 3-9).

The non-sorbing gas helium invades the pores when a pressure is applied. The AP-608 machine is capable of directly measuring pore volume for cylindrical core plugs by measuring the grain volume. From this, porosity is calculated using Equation 3-9 if bulk volume is known (e.g., calculated from the dimensions of core plugs):

$$\Phi = \frac{PV}{BV} \text{ x } 100 \qquad\qquad (3\text{-}9)$$

Where,

Φ = porosity (%)

PV = pore volume (cm^3)

BV = bulk volume (cm^3)

This instrument uses the pressure-decay method to determine the Klinkenberg-corrected permeability, slip, and turbulence correction factors. This technique is well suited for low permeability samples, 0.1 milidarcy to about 0.01 microdarcy (API RP 40, 1998) because the small differential pressures and low permeabilities eliminate inertial flow resistance. In general, the lower the permeability of a sample, the slower the pressure decay.

Since the ultra-low permeability nature of shale samples, the pulse-decay method is suitable to estimate the permeability of a shale sample. This method assumes Darcy flow as the only flow regime during permeability test, so gas slip effect is needed to consider differentiating gas permeability from that of liquids. At the molecular level, gas molecules collide with pore walls and tend to slide while not losing velocity during gas flow (Wang et al., 2017). Gas slippage can be significant when the pore throat size is comparable to the mean free path of gas molecules at a given pressure and temperature. Klinkenberg (1941) identified this gas slip effect, which was later called the Klinkenberg effect and included it in his equation for permeability 3-10:

$$k_a = k_\infty \left(1 + \frac{b_k}{P_m} \right) \qquad\qquad (3\text{-}10)$$

Where,

k_a = corrected permeability ($10^{-3}\mu m^2$)

k_∞ = intrinsic permeability ($10^{-3}\mu m^2$)

b_k = Klinkenberg factor (psi)

P_m = mean pore pressure (psi)

To obtain b_k, the corrected permeability, k_a, is measured at a minimum of three different mean

pore pressures (API RP 40, 1998). The Klinkgenberg factor is found by Equation 3-11:

$$b_k = \frac{16c\mu}{w}\sqrt{\frac{2RT}{\pi M}}$$
(3-11)

Where,

c = constant typically taken as 0.9 (Wang et al., 2015)

μ = helium viscosity (Pa·s)

M = helium molecular weight (g/mol)

w = width of pore throat (μm)

R = universal gas constant (J/mol)

T = temperature (°C)

3.6.1 Procedure for Helium Porosity and Permeability

The procedure follows Coretest Systems (2012) operator manual for the AP-608 instrument. A

core plug (2.5 cm in diameter x ∼ 3 cm in height) is loaded into the core holder. Then, with the confining

fluid reservoir pressure regulator set to apply 25 psi of air pressure, valve 5 is open, with helium

displacing air from system and the coreholder through plastic drain line. Any remaining air from the

confining pressure intensifier is purged, repeated two to three times. A reference volume calibration is

completed which is used for porosity and permeability measurements. The system then applies 1,000

psi confining pressure to the coreholder and 200 psi of pore pressure. After a stabilizing period, valve 1

will close and the system will monitor for stability. After this pressure has become stabilized P1 is

recorded. Next, the volume adjuster will retract increasing the volume by a known, fixed amount, When

the pressure has stabilized, P2 is recorded and the reference volume is calculated. The AP-608 measures

the porosity and permeability of core sample at 20 confining pressures (test steps). The fill valve is

closed and the pressure is monitored until no further change is observed, indicating thermal and

pressure equilibrium. After this pressure has become stable, valve 1 is open, initiating the pressure-

transient portion of the measurement. This decay is measured in time and recorded. A differential

pressure transducer measures the pressure difference between the reservoirs, and another transducer

measures the absolute pressure in the downstream reservoir (API RP 40, 1998)
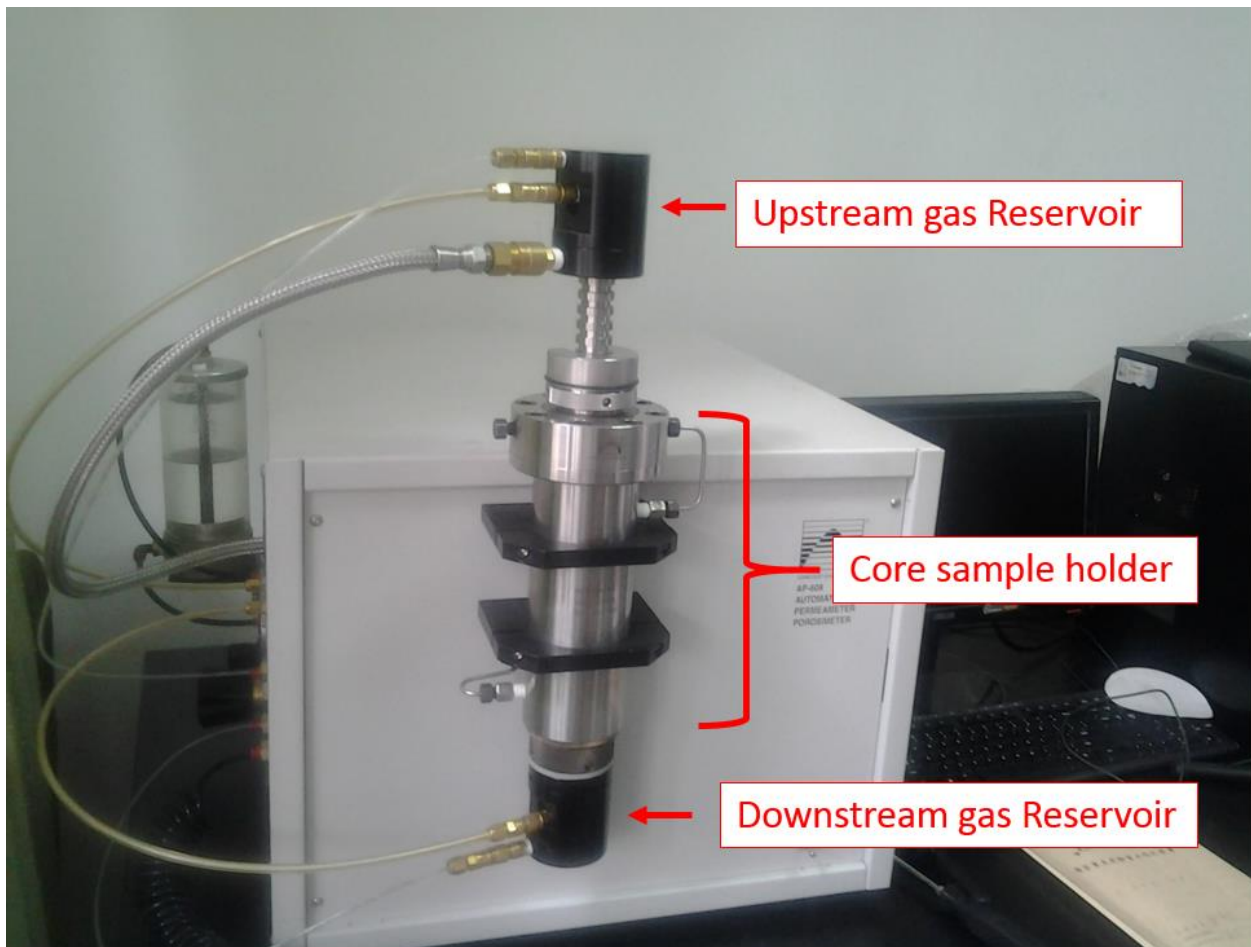
Figure 3-9 AP-608 Automated Porosimeter-Permeameter

3.7 Low Pressure Nitrogen Gas Physisorption

Nitrogen (N_2) gas physisorption is performed on crushed samples (GRI) by measuring the quantity of gas adsorbed onto or desorbed from a solid surface at some equilibrium vapor pressure (Quantachrome Instruments, 2015). This method is conducted at a constant temperature of -196.15 °C (-321.1°F), controlled by liquid nitrogen, at a relative pressure (P/P_o) in the range 0.001 to slightly less than 1.0 for nitrogen gas (Quantachrome Instruments, 2015). Direct measurements include adsorption/desorption isotherms of sorbed gas amount over relative pressure, from which data can be reduced to, BET surface area (single and/or multipoint), Langmuir surface area, pore size and surface area distributions, micropore volume and surface area are modeled according to some theories (Quantachrom Instruments, 2015). This experiment was conducted at one of our collaborating universities, China University of Geosciences at Wuhan (CUG), using the autosorb iQ (Quantachrom Instruments, Boynton Beach FL; Figure 3-10).

When a sample is incrementally being saturated with N_2, nitrogen gas will be sorbed onto sample's surfaces. Isotherms are produced as the quantity adsorbed under different relative pressures is recorded and can provide information on the surface area, pore volume and pore size distribution. The shape of isotherm and the hysteresis pattern are useful to qualitatively predict the type of pores present. The isotherms may be grouped into one of six types presented by Sing et al. (1985), and hysteresis patterns into four types (Labani et al., 2013). Direct measurements from this instrument are based on numerous well-studied theories. Specific surface area (m^2/g) is obtained by the Brunauer-Emmett-Teller (BET) method (Brunauer et al., 1940) which is based on the adsorption theory of multimolecular layers. Pore size distribution and mesopore volume by Dollimore-Heal (DH) and Barrett-Joyner-Halenda (BJH) method (Barrett et al., 1951; Dollimore and Heal, 1964). Gegg and Sing (1991)

used both methodologies to calculate actual pore size assuming cylindrical shaped pores using the

thickness of adsorbed layer and the Kelvin equation. However, Ravikovitch et al. (1998) determined that

previous two methods do not give a realistic description of micropore filling and leads to an

underestimation of pore sizes for micropores and mesopores. The Density Functional Theory (DFT) takes

into account the absorbent and absorbate (Lastoskie et al., 1993) and provides a more accurate

approach for pore size distribution at sub-nano size range. The measurement range for pore size

distribution for the BJH method is approximately 3.1 to 220 nm, while for DFT is 1.41 to 36.0 nm. A more

detailed discussion of theories and calculations behind methods is comprehensively discussed in

previous aforementioned works.

Figure 3-10 AutosorbiQ apparatus for low pressure gas physisorption

3.7.1 Procedure for Low Pressure Nitrogen Gas Physisorption

It is required to remove moisture content by degassing samples prior to analysis, as volatile substances and free water will compete with nitrogen molecules for adsorption sites. Each sample is first dried in an oven at 60 °C for at least 48 hours. Dried sample of about 0.05 g is then placed into the sample cell with a diameter of 4 mm, which is installed onto the sample degassing apparatus operating at 300 °C for 3 hours under vacuum (Quantachrome Instruments, 2015). After evacuation, an isotherm tube is attached to sample cell. The manifold and sample tube are evacuated and after sufficient vacuum has been achieved, the manifold is cooled to -196.15 °C (-321.1°F) by raising the liquid nitrogen tank allowing free space to be determined at the analysis temperature. The nitrogen gas is dosed into manifold. By opening the sample port, nitrogen adsorbs onto sample surfaces. The instrument records nitrogen pressure and temperature, and also the quantity of nitrogen gas removed from the manifold (Quantachrome Instruments, 2015).

3.8 Contact Angle

The contact angle test observes the surface wetting characteristics of the sample and determines whether the shale is wetting or non-wetting to de-ionized (DI) water (hydrophilic fluid), API (American Petroleum Institute) brine, n-decane (hydrophobic fluid), 20% isopropyl alcohol (IPA) in de-ionized water. API brine is water wetting but with a high salinity to mimic formation fluid, and the 20% IPA is to achieve an intermediate surface tension between DI water and API brine. The test is conducted on a flat surface of the sample. One drop of fluid (2μL) from a pipette is used to wet the surface to observe the spreading of the liquid. From this experiment, the contact angle the bead makes with the sample surface interface is measured, and each sample is photographed and recorded during testing (Model SL200KB, Kino; Figure 3-11). The contact angle will be taken at the 30 second mark of the

experiment. No spreading of the fluid on the sample is represented by a very high contact angle (∼ 100°) while perfect spreading of the fluid is represented by a very low contact angle (∼ 0°).
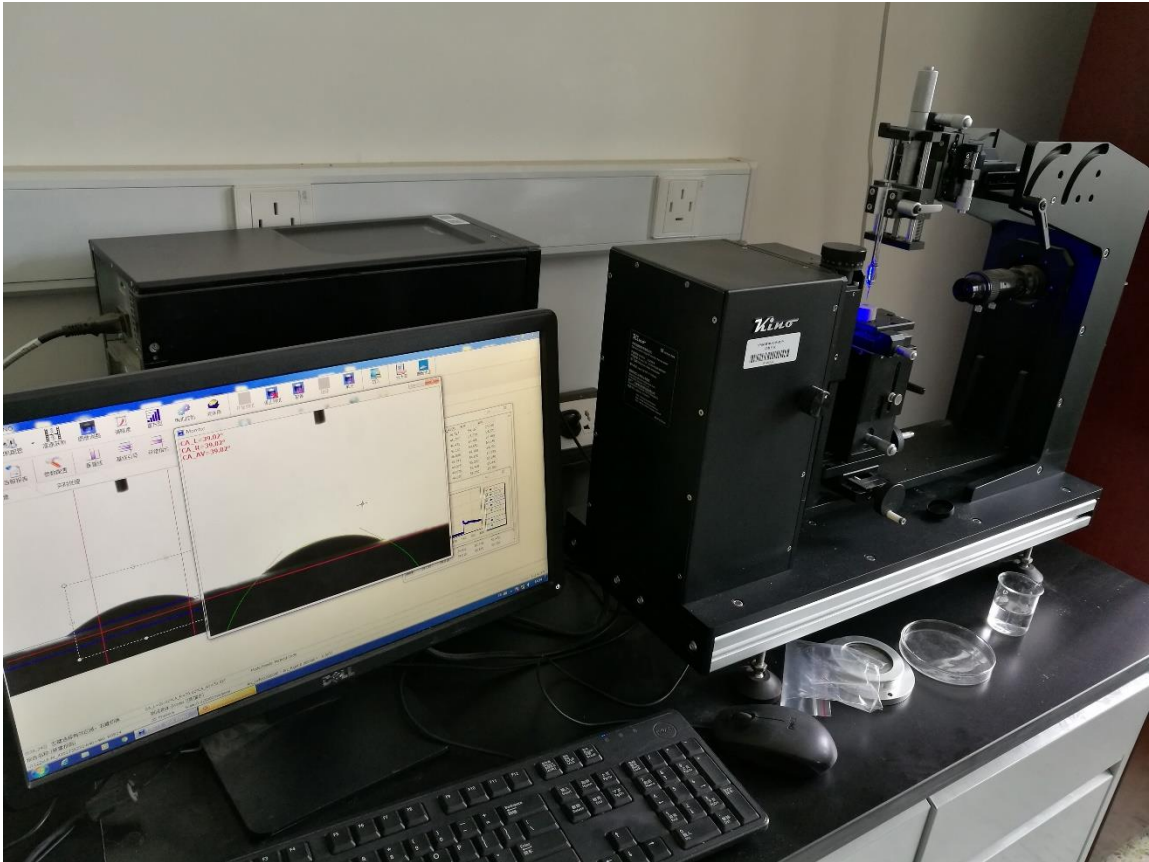
Figure 3-11 Kino Model SL200KB instrument for contact angle measurement

3.9 Spontaneous Fluid Imbibition

Spontaneous fluid imbibition is the process by which a wetting fluid is drawn into a porous medium by capillary action (Morrow and Mason, 2001). The University of Texas at Arlington possess the fluid imbibition instrument. The rate of imbibition is primarily dependent on the porous media, the fluids, and their interactions which include matrix permeability and relative permeability, matrix shapes and boundary conditions, fluid viscosity, interfacial tension and wettability (Zhang et al., 1996). Spontaneous imbibition of wetting liquid into porous media is regarded as a crucially important driving mechanism for enhancing oil recovery from naturally fractured reservoir, especially with low

permeability (Cai et al., 2012). Imbibition test involve exposing one face of a shale sample to liquid (water or n-decane) and monitor the mass uptake over time (Hu et al., 2001; Hu and Ewing, 2014). To evaluate the imbibition behavior, the equations of Philips, and Handy are used. In soil science, Philip (1957) developed the Philip's Infiltration Equation (Equation 3-12) which relates cumulative infiltration (e.g., imbibition) with time and sorptivity. This equation assumes that capillary pressure is greater than gravity.

$$I = St^{0.5} \tag{3-12}$$

Where,

I – cumulative Imbibition (mm)

S – sorptivity (a function of initial water content and porous media; mm/min$^{0.5}$)

t – infiltration time (min)

In petroleum engineering, Handy (1960) has a similar equation to Equation 3-13 which relates volume of imbibed fluid, acting in a piston-like manner, to the one-dimensional spontaneous imbibition of fluid into rock sample. In this equation, the weight or volume of the imbibed water is proportional to the square root of the imbibition time. The driving force for fluid imbibition is capillary force as the gravity is neglected.

$$N_{wt}^2 = A^2 \frac{P_c k_w \emptyset S_{wf}}{\mu_w} t \tag{3-13}$$

Where,

N_{wt} – volume of water imbibed into the sample (cm^3)

A – cross-section area of the core (cm^2)

P_c – capillary pressure at a fluid saturation of wetting front S_{wf} (Pa)

k_w – effective permeability to fluid phase (cm^2)

μ_w – fluid viscosity (Pa·s)

t – time (s)

Presented in Equation 3-12, sorptivity, another useful parameter to quantifying the rate of imbibition behavior, that is jointly controlled by the capillary pressure and permeability (Philip, 1957; Kao and Hunt, 1996). When the gravitational force is negligible, the cumulative infiltration/imbibition is related to the square-root-of-time through sorptivity with a slope of 0.5 (Philip, 1957; Kao and Hunt, 1996; Hut et al., 2001; Tokunaga and Wan, 2001).

In addition, the effective wetted distance (L_d) equals the cumulative infiltration divided by the step change in the volumetric fluid content ($\Delta\theta$), which is often less than or equal to the porosity of porous media:

$$L_d = H/\Delta\theta \tag{3-14}$$

Combining Equations 3-12 and 3-14, the effective wetting front distance (L_d) can be expressed as (Tokonaga and Wan, 2001):

$$L_d = \frac{S}{\Delta\theta}\sqrt{t} \tag{3-15}$$

Assuming that the porous medium has good pore connectivity, Equation 3-16 is often used to characterize the imbibition behavior in one-dimensional medium. Kao and Hunt (1996) further reported that, when the porous medium has a perfect wettability (contact angle is zero) towards an imbibing fluid, there is a one-fourth power relationship between the permeability and the effective wetted distance (Kao and Hunt, 1996; Tokonuaga and Wan, 2001):

$$L_d = B\sqrt{\sigma/\mu}\,k_{imb}{}^{1/4}\sqrt[4]{t} \tag{3-16}$$

Where constant B reflects the geometry of the porous medium (0.5 commonly used); σ is the liquid-gas surface tension, mN/m; μ is the fluid viscosity, mPa·s; k_{imb} is the permeability of porous media obtain from imbibition data.

Combining Equation 3-15 and 3-16, a relationship between a fourth-power of sorptivity and the permeability of the porous media (k_{imb}) can be obtained from imbibition tests, which is expressed as follows (Kao and Hunt, 1996; Tokonaga and Wan, 2001):

$$k_{imb} \sim \left(\frac{\mu}{\sigma}\right)^2 \left(\frac{S}{B\Delta\theta}\right)^4 \qquad (3\text{-}17)$$

This study will focus on spontaneous fluid imbibition of the upper Ordovician strata using two fluids (DI water and n-decane) to probe pore connectivity along with the interaction between different fluids in the sample. Indicated by the slope of log imbibed liquid mass versus log time, we probe pore connectivity by using the results of network modeling of Ewing and Horton (2002). Generally, the slope characteristics for imbibing fluid can be divided into three stages: the initial stage (Stage I), linear imbibition stage (Stage II), and late imbibition stage (Stage III) (Yang et al., 2017). During Stage I, the balance weight (e.g., imbibed mass) of some samples may fluctuate for a few minutes as the cumulative imbibition is increasing quickly with respect to time. This may be the result of fluctuations in weight, the boundary effect and/or instability of sample. During Stage II, the sample stabilizes and linear relationships in log-log spaces can be observed in which can be used to qualitatively assess the pore connectivity. The driving force in Stage II may be mainly capillary pressure in macro- and meso-pore networks (Yang et al.,2017). During Stage III, the imbibed fluid has very small slope (usually close to zero) suggesting fluid has reach the top of the sample. At this point the fluid will continue to imbibe into the sample's nano-sized matrix until available pore space is filled. The driving force in this period is also capillary pressure (Yang et al., 2017). The imbibition behavior – slope of ¼, ¼ changing to ½, or ½ roughly classifies a rock's pore connectivity (Hu et al., 2012; Hu and Ewing, 2014). A slope of ¼ indicates poor

connectivity in which the pore connectivity is barely above the percolation threshold. Below this threshold, it is assumed that connected pores do not exist over the observational scale. A slope of ¼ changing to ½ is indicative fluid imbibition (analogous to solute diffusion) is anomalous at short times and distances, but later transitions to classical Fickian behavior. A slope of ½ is indicative of a well-connected pore system.

3.9.1 Procedure for Fluid Imbibition

For the imbibition experiments, samples were cut into cubes of about 1 cm^3. All sides except the top and bottom were treated with quick-cure transparent epoxy to allow 1-dimensional imbibition and avoid evaporation and condensation of imbibing fluid through the sides of the sample. The samples were epoxied so that imbibition was carried in the direction perpendicular to the bedding place of the sample. The samples were initially dried in the 60°C oven for a period of at least 48 hours, and then immediately place in desiccator ($\sim$ 23°C) with less than 10% relative humidity to be cooled to room temperature. This is done to achieve a constant initially dry water saturation state. The imbibition setup is shown in Figure 3-12. Before running the imbibition experiment, various objects need to be weighed which include: "dish + solution", sample only, and "sample + holder". Beakers of fluid (same fluid in the "dish + solution") were placed inside the experiment chamber to keep the relative humidity high and constant inside the chamber. The holder has aluminum foil placed inside of it and between the sample held in place with a small hole left for air to escape which could lead to vapor transport and capillary condensation on to the top face to some extent but smaller than the imbibition amount from the bottom face. The "sample + holder" was placed onto a hook that is connected to the electronic scale. The sample bottom is submerged to a depth of about 1 mm in the fluid reservoir (DI water or n-decane) by raising the adjustable stage. The imbibition rate is monitored by automatically recording the sample weight change over time. For the first two minutes, the sample weight is recorded every second. Then from the elapsed time interval of 2 to 60 minutes, the sample weight is recorded every 30 seconds. After

60 elapsed minutes the electronic balances is changed to record the sample weight every 2 minutes. The

electronic balance used is a high precision analytical balance (Shimadzu Analytical Balance AUW22OD,

with a precision of 0.01 mg). Once the desired timing of test is completed, the final weight of the sample

is recorded. A Kimwipe is slightly moistened with the imbibing fluid used and weighed. This is to remove

any residual fluid before weighing the sample that is adhered to the sample face. The moisten Kimwipe

is then weighed again to record any weight change from the contact with the sample. The "sample +

holder" is weighed again, along with sample and the holder itself. Finally, the "dish + solution" is

weighed. The measurements taken will be used for data processing and analysis of the test results.
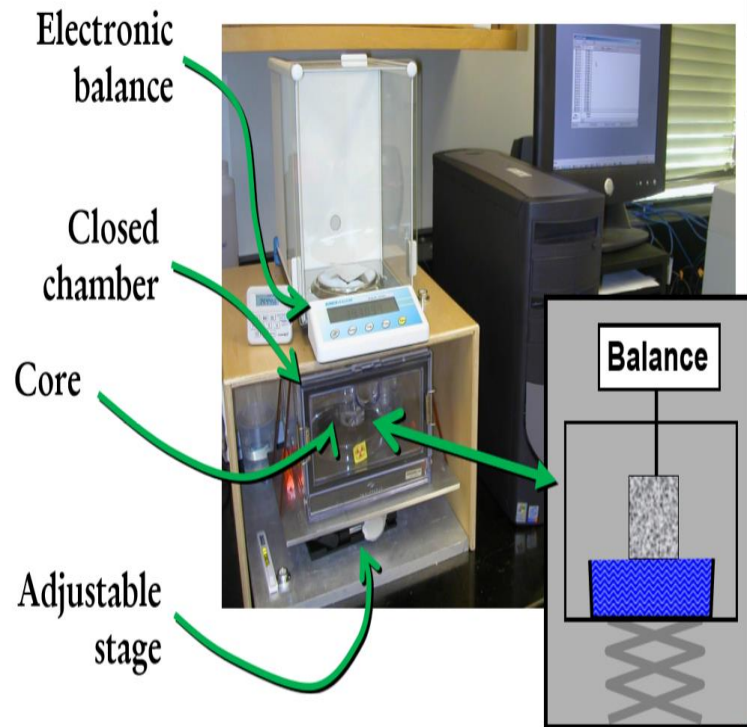
Figure 3-12 Imbibition apparatus

3.10 Production Data

DrillingInfo gathers monthly production data in the state of Ohio and offers data analytics to observe trends in production. A complimentary subscription of Drilling Info provided to the Dr. Qinhong Hu's research group here at the University of Texas at Arlington. This allowed production data to be viewed quickly and accurately, and linked to petrophysical and geochemical studies in the lab.

Chapter 4: Results

4.1 XRD

The mineralogy data from XRD is posted on Table 4-1. Most sample compositions are dominated by carbonate, quartz and clay with minor amounts of feldspars and pyrite (Figures 4-1, 4-2, 4-3, and 4-4). In Figure 4-5, wells Prudential #1-A, Cadiz B, Well A, and Well B are plotted on a ternary diagram for organic mudstones proposed by Schlumberger (2014). For this ternary diagram, the end members are dry-weight for clay (Illite + chlorite + muscovite +kaolinite), carbonate, and QF (quartz + feldspar) in weight percent. The Kope Formation sample is plotted as a mixed mudstone. The Utica Shale samples displayed great heterogeneity, both vertically within a well and laterally between wells, plotting as argillaceous/siliceous mudstone, mixed mudstone and mixed carbonate mudstone. Being more carbonate rich, the Point Pleasant samples plotted near the line between mixed carbonate mudstone and silica-rich carbonate mudstone lithotype. All the Lexington Limestone samples plotted as a carbonate-dominated lithotype displaying more homogeneity than other formations.

Table 4-1 Major mineral groups (wt. %) for each sample tested

	Whole Rock Mineralogy (wt. %)							Clay Mineralogy (wt. %)			
	Quartz	Feldspar	Carbonate	Pyrite	Baryte	Sulfides, Sulfate, Oxide and other	Total Clay	Illite	Muscovite	Chlorite	Kaolinite
P1144-U	35.9	-	12	4.3	-	2.7	45.2	-	29.9	15.3	-
P1235-U	23.5	6	37.5	3.3	-	11.8	18	-	16.9	1.1	-
P1336-U	27.4	3.1	51	3.6	-	-	14.8	-	12.3	2.5	-
CB8500-U	23.9	6.6	30.8	5.7	4.6	8.4	20.1	-	12.8	7.3	-
CB8600-U	15.6	2.7	60.4	2.4	2	1	15.8	-	6.4	9.4	-
CB8670-U	14.8	6.4	55.6	1.9	4.4	3.1	13.9	-	10.8	23.3	-
KS9930-K	21.4	3.7	23.8	3.5	-	8.7	38.9	-	15.6	4.2	-
KS10121-U	17.4	4.5	65.7	-	-	0.5	12	-	7.8	1.6	-
KS10150-PP	9.2	-	63.6	2.3	-	11.3	13.5	-	4.2	0.6	-
KS10230-LL	8.6	2.7	84	1.5	-	0.6	2.7	-	2.1	15.3	-
KB10150-U	15.9	1.9	22.6	2.1	5.5	37.2	14.5	3.9	4.3	1.1	6.3
KB10180-U	20	4.8	43.7	2.6	1.7	4.2	23	8.5	5.4	2.5	9.1
KB10210-PP	18.5	2.7	59.6	3.6	6.4	-	9.1	3.4	3.9	-	-
KB10240-PP	16.8	2.9	62.6	3.6	5.1	2.3	6.9	3.2	2.1	-	-
KB10270-PP	17.9	3.5	59.2	6.2	3	3.5	6.6	3.2	2.4	1.8	1
KB10300-PP	17.1	3.1	56.6	4.4	4.3	4.1	10.5	4.6	4.8	1.6	1.1
KB10330-PP	20.7	3.4	55	4	4.8	4.1	8	3.7	2.7	-	1.6

KB10360-PP	20.9	3	57.1	5.6	3.3	1.6	8.5	3.2	3.9	-	1.4
KB10390-LL	4.1	0.4	91.3	0.6	1.7	1.4	0.5	-	0.5	-	-
KB10420-LL	9.5	2.7	79	2.8	2.2	-	3.7	-	3	-	0.7
KB10450-LL	7.6	1.2	80.3	2	2.2	0.8	4.9	1.2	2.6	1.1	-
KB10480-LL	9.1	2.9	78	3.3	3.5	-	3.2	-	2.5	0.7	-
KB10510-LL	8.6	1.7	74.7	3.2	3.7	-	8.2	-	7.4	0.8	-
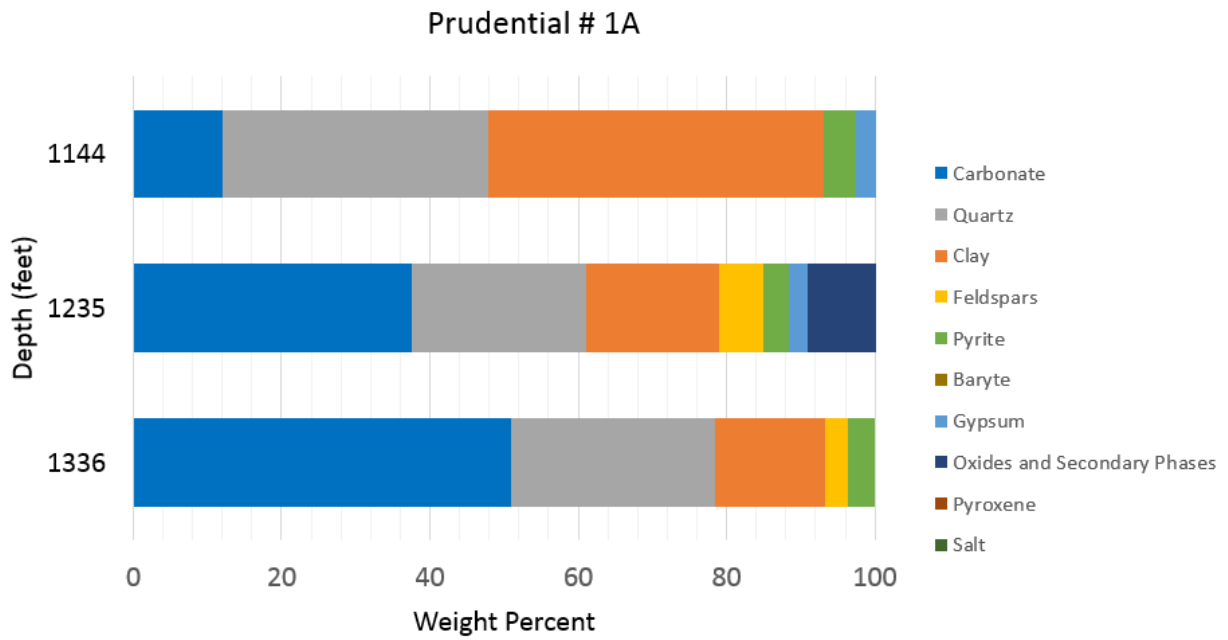
Figure 4-1 Mineralogy of Prudential #1A in weight percent
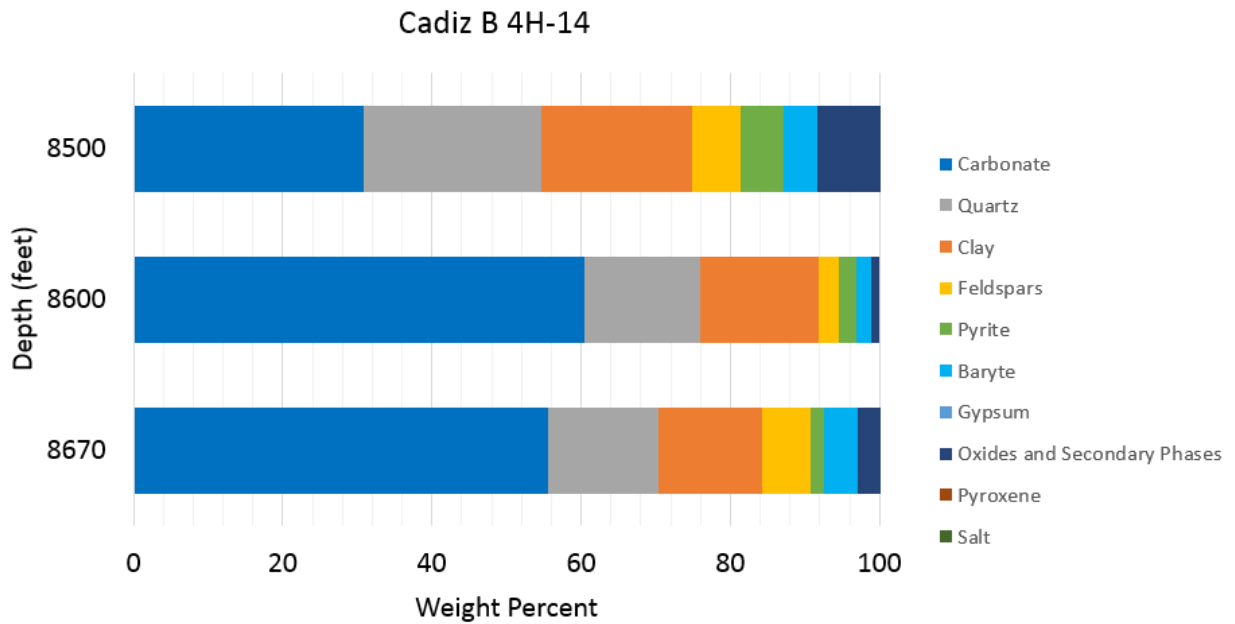
Figure 4-2 Mineralogy of Cadiz B in weight percent
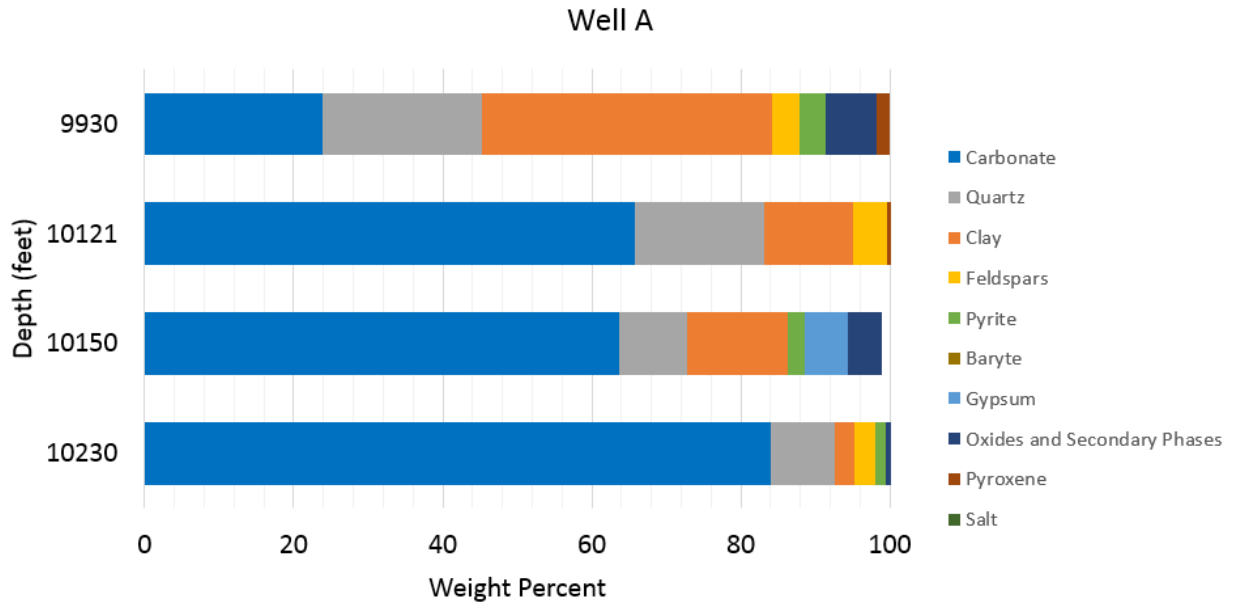
Figure 4-3 Mineralogy of Well A in weight percent
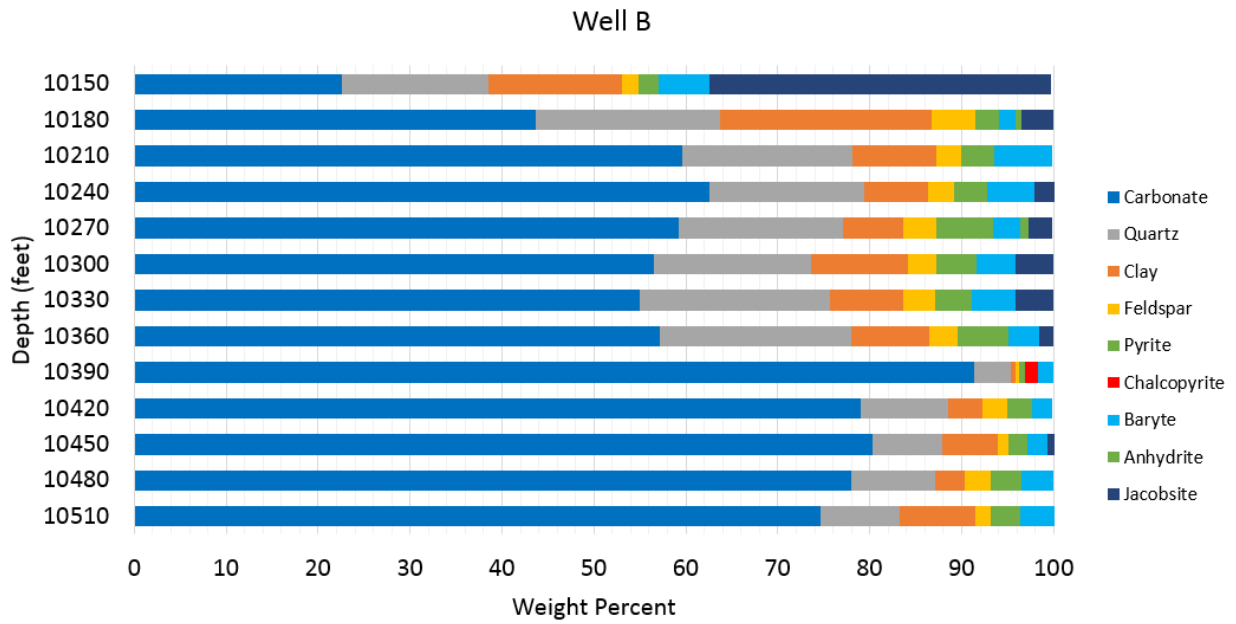
Figure 4-4 Mineralogy of Well B in weight percent
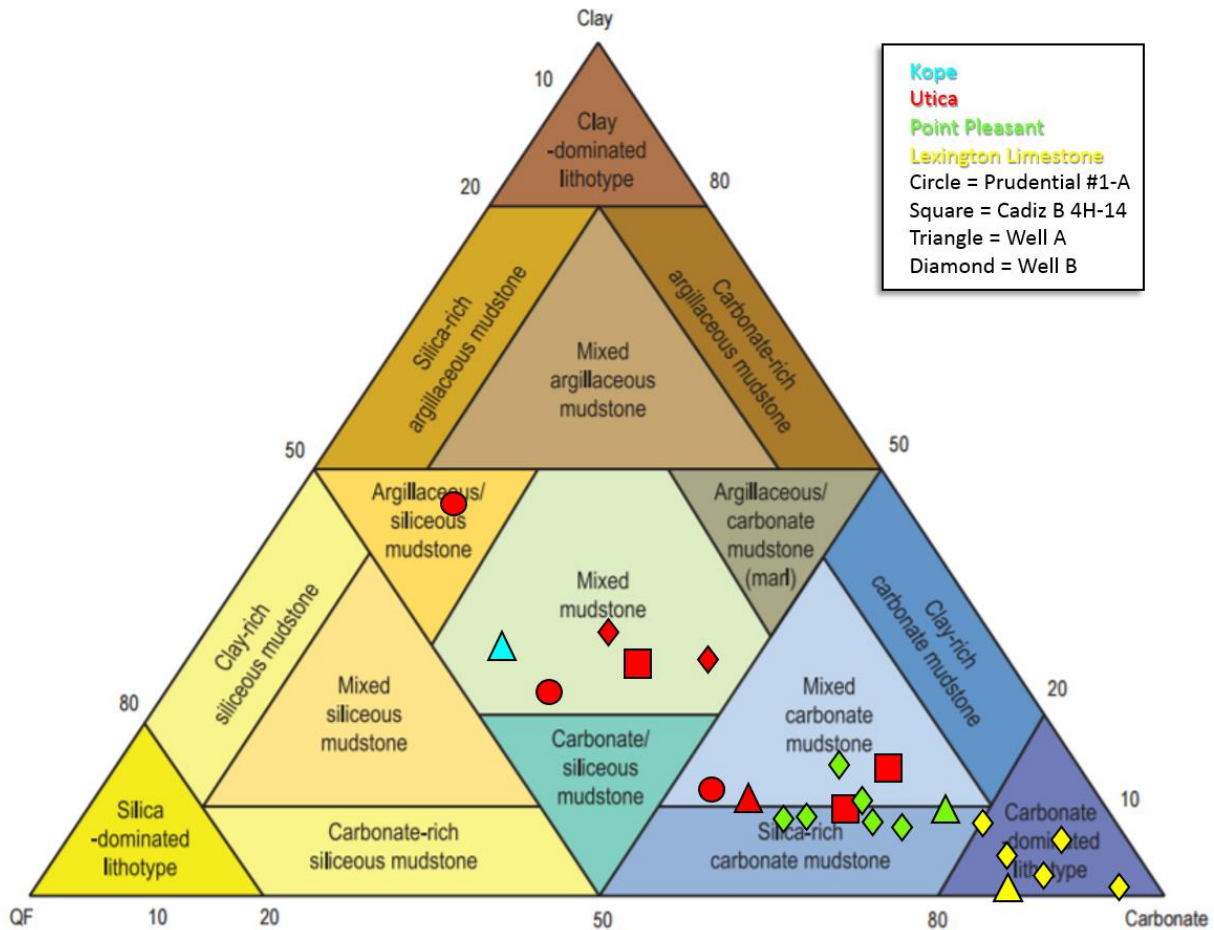
Figure 4-5 Schlumberger (2014) sCore lithofacies ternary diagram for mudstones samples plotted on it

4.2 TOC

All the samples were tested for TOC except for samples from Well B. Results from TOC are shown in Table 4-2. The average TOC value for the Utica Shale in Prudential #1-A and Cadiz B 4H-14 is 3.36 and 1.78, respectively. In Well A TOC values ranged with the highest TOC value being 4.57 % (Point Pleasant), and the lowest TOC value being 0.46 % (Kope Formation). In the Utica Shale, well Cadiz B and Prudential # 1A, there is an increase in TOC values with depth. In Well A we also see an increase of TOC % with depth except for the deepest sample of the well, KS10230-LL, it decreases to 2.5%.

Table 4-2 TOC results for samples

Sample	TOC (%)
P1144-U	3.33
P1235-U	3.20
P1336-U	3.54
CB8500-U	1.31
CB8600-U	1.59
CB8670-U	2.44
KS9930-K	0.46
KS10121-U	3.37
KS10150-PP	4.57
KS10230-LL	2.50

4.3 Pyrolysis

Pyrolysis was performed on all samples and the results are presented in Table 4-5. S3 values were not able to be obtained from our analyses, but S4 is measured as the organic matter remaining in the sample after pyrolysis. Table 4-3 show standard guidelines for interpreting source rock quality, quality and maturation, and commonly used for pyrolysis results (Peters and Achaegakwo, 2016).

Table 4-3 Guidelines for interpreting source rock quantity, quality and maturation, and commonly used parameters (Peters and Achaegakwo, 2016)

Quantity	TOC	S1(mg HC/g rock)	S2(mg HC/g rock)
Poor	<0.5	<0.5	<2.5
Fair	0.5-1	0.5-1	2.5-5.0
Good	1-2	1-2	5-10
Very Good	2-4	2-4	10-20
Excellent	>4	>4	>20
Quality	HI (mg HC/g TOC)	S2/S3	Kerogen Type
None	<50	<1	IV
Gas	50-200	1-5	III
Gas and Oil	200-300	5-10	II/III
Oil	300-600	10-15	II
Oil	>600	>15	I
Maturation	Ro (%)	Tmax (0C)	TAI
Immature	0.2-0.6	<435	1.5-2.6
Early Mature	0.6-0.65	435-445	2.6-2.6
Peak Mature	0.65-0.9	445-450	2.7-2.9
Late Mature	0.9-1.35	450-470	2.9-3.3
Post Mature	>1.35	>470	>3.3

The one Kope Formation sample, which is an organic-poor shale with poor hydrocarbon potential, yielded the lowest values for S1, S2, and T_{max} of 0.17 mg HC/g, 0.14 mg HC/g, and 418 °C respectively. The distribution range for S1, amount of free hydrocarbons, for the Utica Shale is 0.74 to 1.51 mg/g (avg. 1.14 mg/g), 1.12 to 4.57 mg/g (avg. 3.03 mg/g) for Point Pleasant Formation, and 0.58 to 2.55 mg/g (avg. 1.74 mg/g) for the Lexington Limestone. All TOC % values generated from pyrolysis collate with our results from TOC in section 4.2. The distribution range for S2, hydrocarbons generated from cracking of kerogen, are 0.54 to 16.99 mg/g (avg. 6.39 mg/g) for the Utica Shale, 0.44-3.51 mg/g (avg. 2.67 mg/g) for Point Pleasant Formation, and 1.11 to 4.4 mg/g (avg. 3.10 mg/g) for Lexington Limestone. Our results reflect the organic richness of the Utica Shale varies from fair to very good source rock with poor to very good source rock potential, Point Pleasant as very good to excellent source rock being poor to fair in source rock potential, and the Lexington Limestone as good to excellent source rock with fair source rock potential (Figure 4-6).
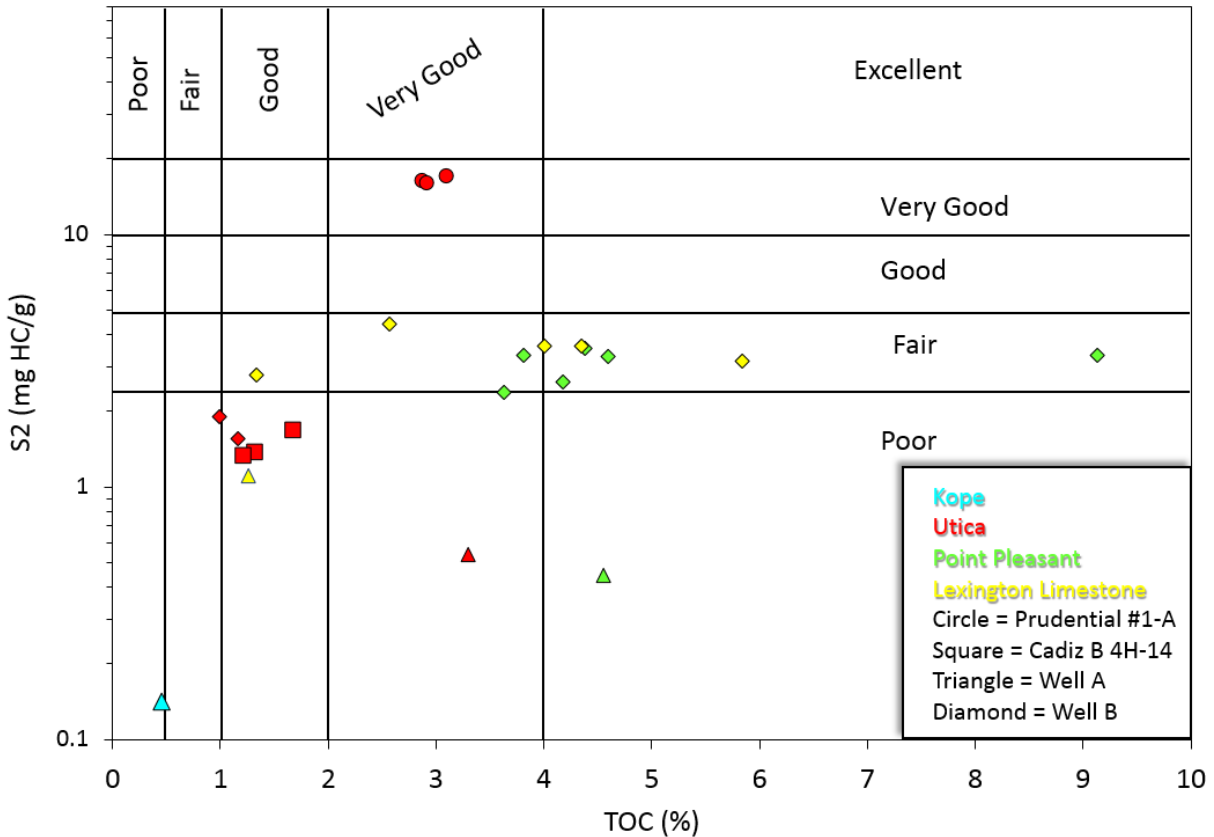
Figure 4-6 Plot of S2 vs. TOC indicating hydrocarbon potential and source efficiency

A key factor controlling hydrocarbon generation potential is the hydrogen content of the organic matter source rock. This factor is hard to determine and HI values from Rock-Eval pyrolysis are commonly used as a proxy (Peters and Achaegakwo, 2016). High HI values indicate an aquatic origin of organic matter, whereas low HI values represent a terrestrial origin or degradation/maturation of organic matter. HI values for the Kope Formation are 30.43 mg HC/g TOC, Utica Shale ranging from 16.36 to 567.25 mg HC/g TOC (avg. 257.48 mg HC/g TOC), Point Pleasant ranging from 9.67 to 86.61 mg HC/g TOC (avg. 58.57 mg HC/g TOC), and Lexington Limestone ranging from 53.69 to 206.77 mg HC/g TOC (avg. 97.88 mg HC/g TOC). Figure 4-7 indicates that the Utica Shale has good to very good generative potential generating gas and/or oil, Point Pleasant has very good to excellent generative potential in which gas would be generated, and the Lexington Limestone has good to excellent

generative potential which would generate gas. This is typical and encouraged by the presence of type II/III and III kerogens.
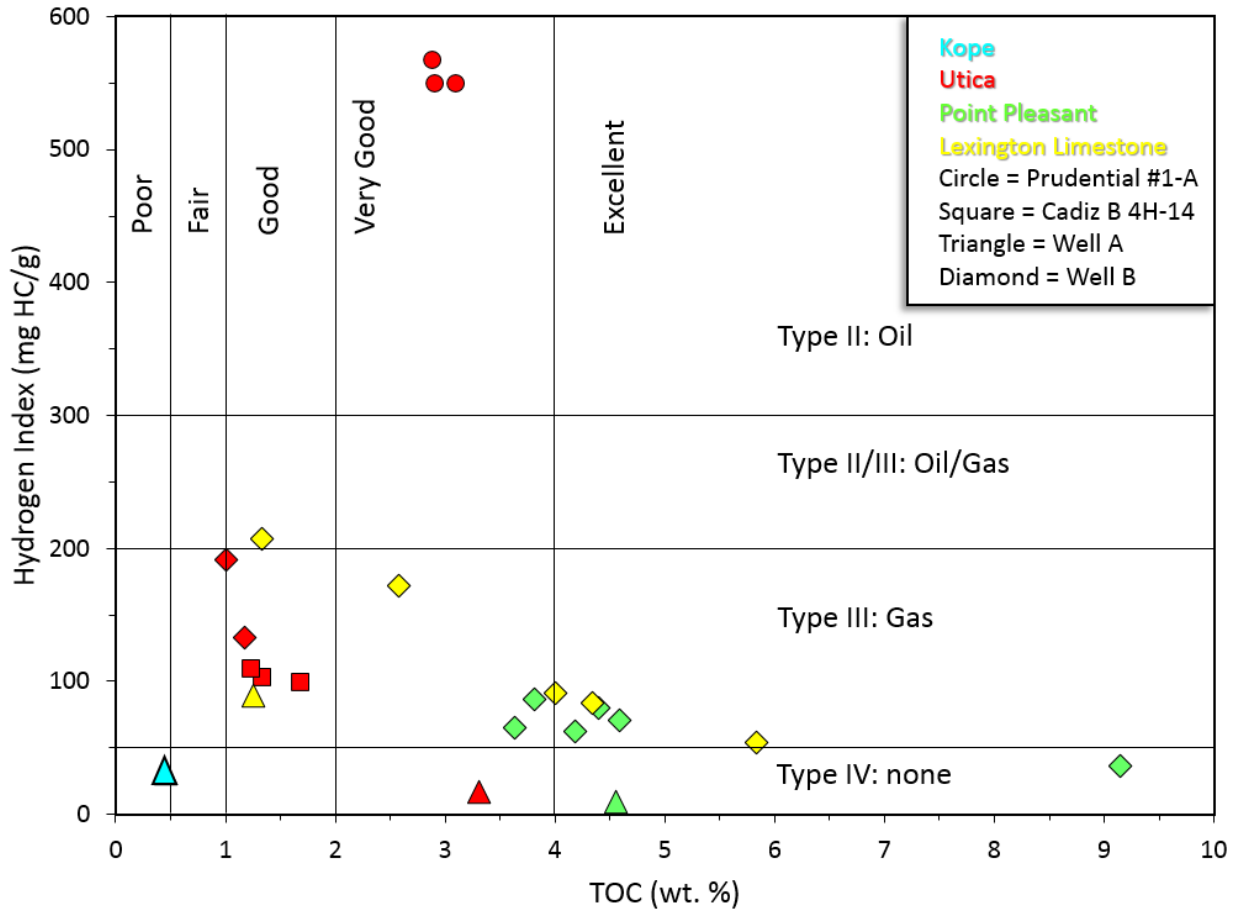
Figure 4-7 Plot of hydrogen index vs.TOC indicating kerogen type and generation potential

Kerogen type is an important parameter when evaluating reservoirs. Waples (1985) and Obaje et al. (2004) determined that it is possible to differentiate between types of organic matter by using HI values. HI greater than 600 mg/g have excellent potential to generate oil. Figure 4-8 plots HI versus T_{max} which can determine kerogen type and thermally maturity. The results show that the majority of samples across formations generally plot under type III and type II/III kerogen, while a group of Utica Shale samples from well Prudential #1-A plot under type II kerogen.

When S2 is plotted against TOC wt. %, kerogen type can be determined (Langford and Blanc-Valleron, 1990). Curves on the S2 vs TOC diagram are drawn as boundaries for kerogen type whereas the HI versus T_{max} serves more as maturity paths for kerogen types. This diagram shows that the majority of our samples across all formations fall within type II/III and III kerogen (Figure 4-9). The only samples to plot outside this range were samples from well Prudential #1-A as the type II kerogen. This further supports our results from the plot of HI vs. T_{max} (Figure 4-8).
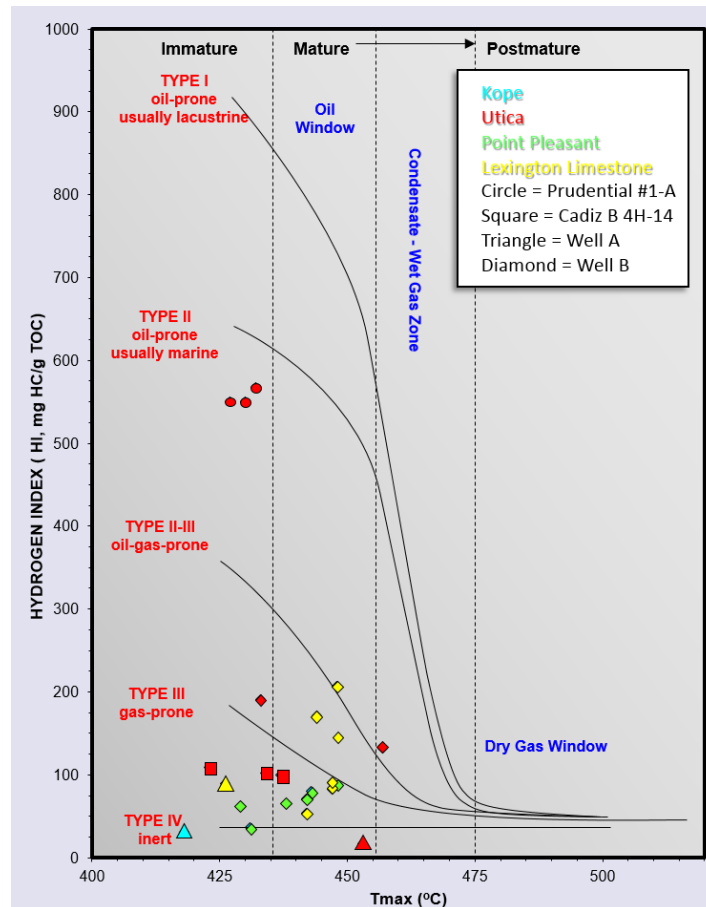
Figure 4-8 Plot of hydrogen index vs. T_{max} indicating kerogen type and thermal maturity
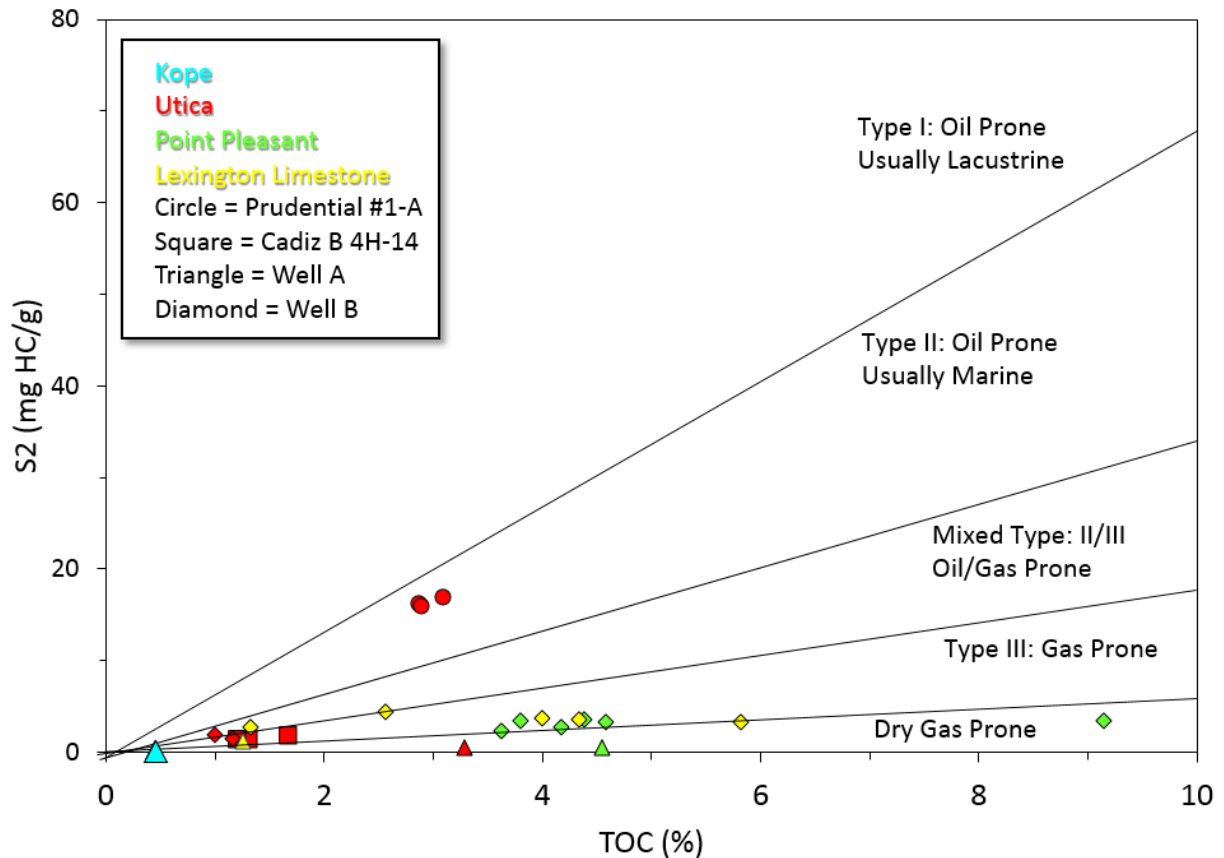
Figure 4-9 Plot of S2 vs. TOC indicating kerogen type

The concentration and distribution of hydrocarbons contained in a particular source depend on both the type of the organic matter and its degree of thermal maturation (Tissot and Welte, 1984). Thermal maturity can be determined from T_{max}, production index (PI), and vitrinite reflectance. Peters (1986) determine relationships between T_{max} and PI from Rock-Eval pyrolysis, and they reported T_{max} and PI values less than 430 °C and 0.1 contains inorganic matter. Mature organic matter T_{max} range from 430°C to 460°C, and a production index between 0.2 to 0.4, producing oil at upper end of values. Mature organic matter within the wet gas-zone has PI values greater than 0.4 and T_{max} greater than 470°C. The distribution for T_{max} are 423°C to 457 °C for the Utica Shale, 376°C to 448 °C for Point Pleasant formation, and 442°C to 448°C for Lexington Limestone. Plotting T_{max} vs. PI can be used to show the hydrocarbon generation zone (Figure 4-10). Our results show most of the samples have non-indigenous

and/or contaminated hydrocarbons and that majority of samples are mature organic matter in the wet

gas zone. Hydrocarbon contamination means that hydrocarbons have been produced in the source

rocks prior to primary migration process (El Nady and Hammad, 2015) which is expected as majority of

our samples are from the mature region of the unconventional reservoir of the Utica Play. A few

samples were dispersed within hydrocarbon generation and as immature. Figure 4-11 plots T_{max} vs.

production index indicate that majority of rock samples have fair source rock quality which are mainly

early mature to mature with moderate level of conversion and few contaminated hydrocarbons.

Waples (1985) and Dow (1977) consider the Ro data to be the most reliable and most commonly

used maturity indicator. A low source-rock grade is associated with Ro values between 0.5 to 0.7%, 0.7

to 1.0% indicate a moderate source-rock grade, and 1.0 to 1.3% reflect a high source-rock grade. For

shales with type II kerogen, Jarvie et al. (2001), calculated vitrinite reflectance (VR_{calc} %) from T_{max} data.

The average VR_{calc} for Utica Play formations in well Prudential #1-A, Cadiz B 4H-14, Well A and Well B are

0.58 %, 0.60 %, 0.99%, and 0.8%. Based on the Figure 4-12 our samples show great variability with

samples spanning the whole maturity spectrum, immature to late mature, which is the purpose of our

sample collection. Using the criteria above for source-rock grade samples from Prudential #1-A and

Cadiz B 4H-14 as low-grade source rock, and Well A and B as moderate grade source rocks. Our

calculated vitrinite reflectance results are lower than expected when compared to maturity maps in

literature. Table 4-4 shows the comparison between our VR_{calc} %, ODNR average calculated R_o% of the

upper Ordovician Shale interval (Figure 2-5), and thermal maturity based on isoreflectance lines (Figure

4-13) defined by Patchen and Carter (2015) in the Utica Play book. Our results indicate comparable

results for Prudential #1-A, but much lower values for Cadiz B 4H-14, Well A, and B. ODNR had the

highest average values across each well for average R_o% (Prudential #1-A is 0.64 %, Cadiz B 4H-14 is

about 1.4 % and Well A and B are about 1.8 %) while our VR_{calc}% estimated the lowest values.
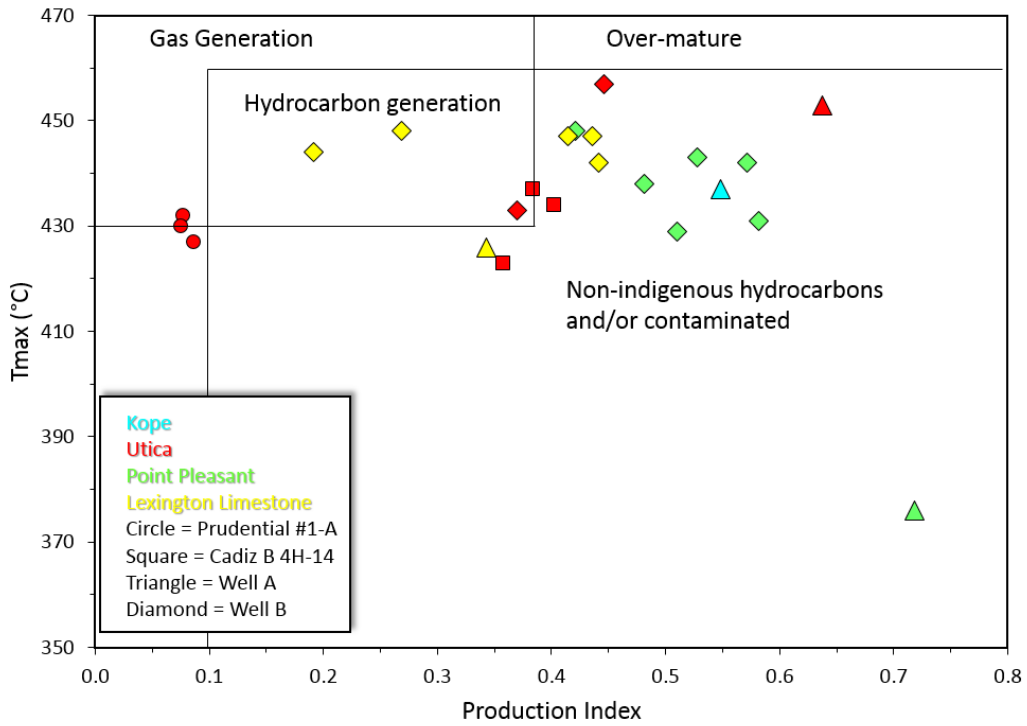
Figure 4-10 Plot of T$_{max}$ vs. PI showing hydrocarbon generation zone
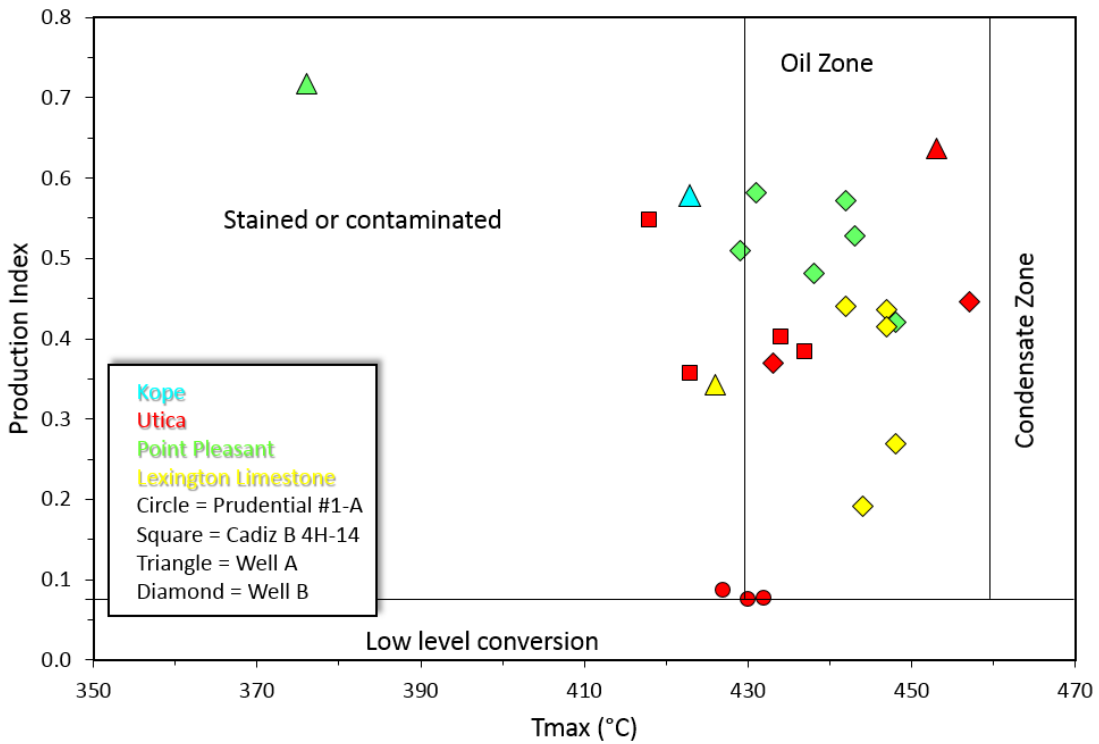
Figure 4-11 Plot of PI vs. T$_{max}$ showing levels of kerogen conversion and maturity
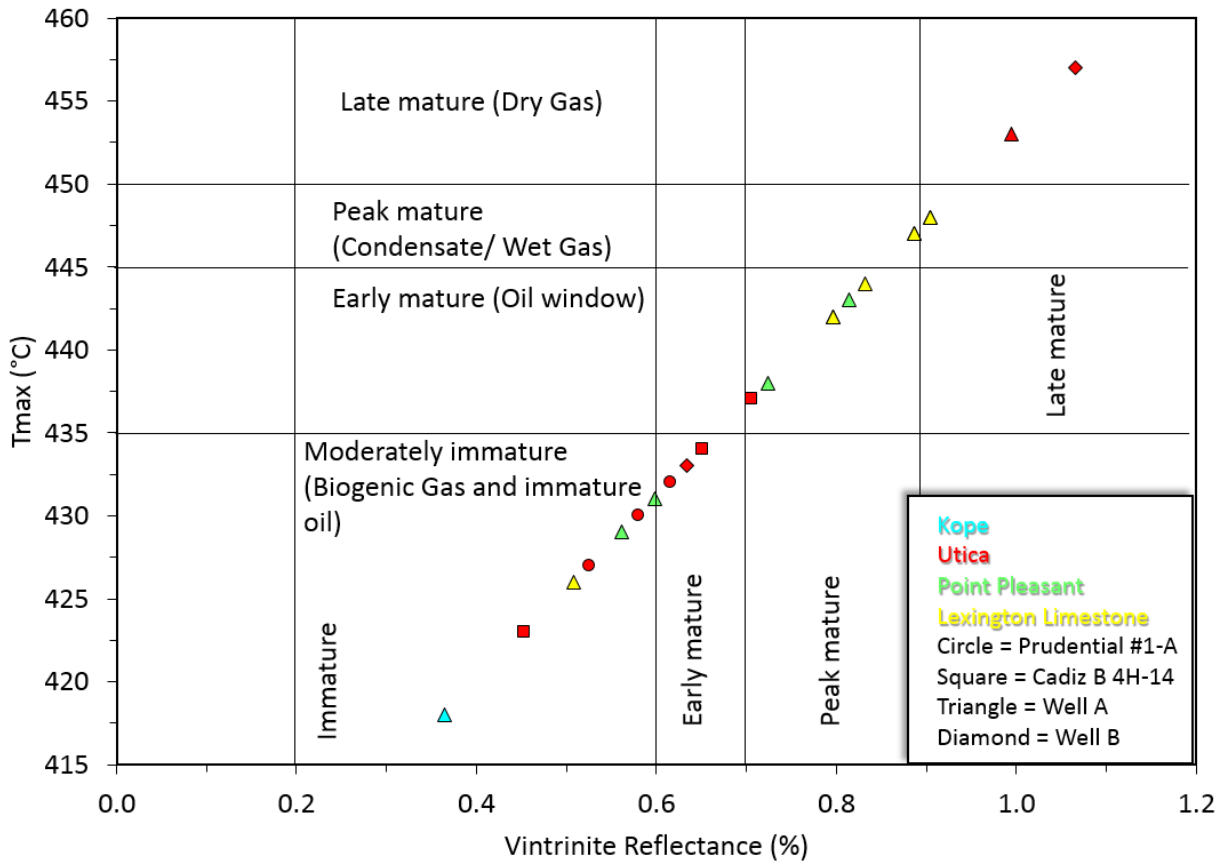
Figure 4-12 Plot of T_{max} vs. R_o showing maturity levels
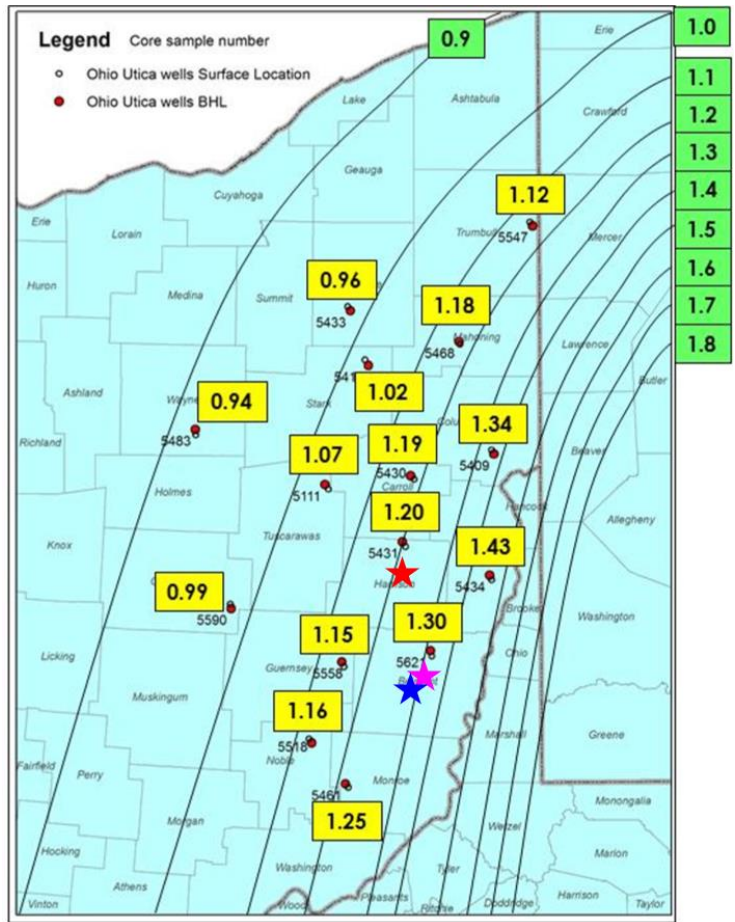
Figure 4-13 Thermal maturity map with isoreflectance lines of eastern Ohio (modified from Patchen and Carter 2015). Red star = Cadiz B 4H-14; magenta star = Well A; blue star = Well B

Table 4-4 Vitrinite reflectance comparasion

Sample ID	R_0		
	Calculated	ODNR (2013)	Patchen and Carter (2015)
P1144-U	0.62	0.64	0.6
P1235-U	0.53	0.64	0.6
P1336-U	0.58	0.64	0.6
CB8500-U	0.65	1.4	1.2
CB8600-U	0.45	1.4	1.2
CB8670-U	0.71	1.4	1.2
KS9930-K	0.36	1.8	1.3
KS10121-U	0.99	1.8	1.3
KS10150-PP	na	1.8	1.3
KS10230-LL	0.51	1.8	1.3
KB10150-U	1.07	1.8	1.3
KB10180-U	0.63	1.8	1.3
KB10210-PP	0.72	1.8	1.3
KB10240-PP	0.56	1.8	1.3
KB10270-PP	0.90	1.8	1.3
KB10300-PP	0.81	1.8	1.3
KB10330-PP	0.60	1.8	1.3
KB10360-PP	0.80	1.8	1.3
KB10390-LL	0.83	1.8	1.3
KB10420-LL	0.90	1.8	1.3
KB10450-LL	0.89	1.8	1.3
KB10480-LL	0.80	1.8	1.3
KB10510-LL	0.89	1.8	1.3

Table 4-5 Results from pryolysis

Sample ID	TOC (%)	S1 (mg HC/g)	S2 (mg HC/g)	S4 (mgC/g)	Tmax (°C)	VR$_{calc}$ (%)	HI (mg HC/g)	PI
P1144-U	2.87	1.36	16.3	14.1	432	0.62	567	0.08
P1235-U	2.90	1.51	15.9	14.5	427	0.53	550	0.09
P1336-U	3.09	1.39	17.0	15.7	430	0.58	550	0.08
CB8500-U	1.32	0.91	1.35	11.3	434	0.65	102	0.40
CB8600-U	1.22	0.74	1.33	10.5	423	0.45	109	0.36
CB8670-U	1.68	1.04	1.67	14.5	437	0.71	99.4	0.38
KS9930-K	0.46	0.17	0.14	4.35	418	0.36	30.4	0.55
KS10121-U	3.30	0.95	0.54	31.7	453	0.99	16.4	0.64
KS10150-PP	4.55	1.12	0.44	44.2	376	na	9.67	0.72
KS10230-LL	1.25	0.58	1.11	11.1	426	0.51	88.8	0.34
KB10150-U	1.17	1.25	1.55	9.34	457	1.07	132	0.45
KB10180-U	1.00	1.12	1.91	7.50	433	0.63	191	0.37
KB10210-PP	3.63	2.18	2.35	32.5	438	0.72	64.7	0.48
KB10240-PP	4.18	2.71	2.60	37.4	429	0.56	62.2	0.51
KB10270-PP	3.81	2.40	3.30	33.3	448	0.90	86.6	0.42
KB10300-PP	4.39	3.93	3.51	37.7	443	0.81	80.0	0.53
KB10330-PP	9.14	4.57	3.29	84.9	431	0.60	36.0	0.58
KB10360-PP	4.59	4.33	3.25	39.6	442	0.80	70.8	0.57
KB10390-LL	2.57	1.04	4.40	21.2	444	0.83	171	0.19
KB10420-LL	1.33	1.01	2.75	10.1	448	0.90	207	0.27
KB10450-LL	4.00	2.80	3.63	34.7	447	0.89	90.8	0.44
KB10480-LL	5.83	2.47	3.13	53.7	442	0.80	53.7	0.44
KB10510-LL	4.34	2.55	3.60	38.3	447	0.89	82.9	0.41
Kope Formation	Utica	Point Pleasant	Lexington Limestone					

4.4 MICP

The MICP approach was used to quantitatively characterize the pore structure, directly and indirectly. The direct measurements obtain from MICP are bulk density, particle density, total pore area, porosity, and pore throat diameter distribution, and through processing the raw data and using the proposed equation from Katz and Thompson (1986; 1987), we can infer the topological aspects of pore structure (permeability and tortuosity) (Hu et al., 2015). All samples from Prudential #1-A, Cadiz B 4H-14, Well A and eight samples from Well B were tested. The MICP machine at UTA (up to 60,000 psi) had

a failure and was not able to get fixed before completion of thesis, so samples were also run at NJU (up to 54,000 psi). Due to a computer failure, sample P1336-U was only measured for an intrusion to 3200 psi. The sample size used for Prudential #1-A and Well A was a cube approximately 1 cm x 1 cm x 1 cm except for sample KS10150-U which was run using GRI. The sample size used for Cadiz B 4H-14 and Well B were all GRI except for sample KB10150-U which was GRI +.

MICP is an effective tool to characterize pore-size distribution and other pore structure parameters. Figure 4-14 shows the cumulative intrusion and extrusion versus the applied pressure observed in MICP. Samples run on GRI/GRI + sized samples had 40 to 490 µL/g of mercury injected into the samples as seen in samples from Utica Shale, Point Pleasant and Lexington Limestone Formations which is much larger than the amount of mercury injected into the 1-cm^3 cubed samples ranging from 5 to 10 µL/g into samples as seen in the Kope, Utica Shale, and Lexington Limestone Formations. A substantial volume of mercury is initially needed to be injected into GRI/GRI+ samples to overcome the conformance pressure (5, 20 and 30 psia, respectively, for different fraction sizes) of the inter-granular pore space. The conformance effect is corrected to obtain intra-granular porosity of GRI/GRI+ samples, to be compared with cube ones.

From Figure 4-14 we can observe hysteresis curves from MICP intrusion and extrusion similar to what we would observe in low pressure gas sorption. Samples from the Kope and Utica Shale Formations produce similar hysteresis curves which show a significant amount of mercury remaining in sample after extrusion. This indicates that larger pore spaces are connected by narrow pore throats also known as the ink-bottle effect (Jiang et al., 2015; Yang et al., 2017). Unlike the Kope and Utica Shale Formations, most samples of the Point Pleasant and Lexington Limestone Formations produce similar hysteresis curves with rapid intrusion and a plateau effect on extrusion at high pressure with drainage starting at about 1000 psia. This phenomenon observed could be due to the lack of micro-and meso-pores. Working with shale, Tinni et al. (2014) notes that crushing the sample will expose more of the

larger pores, which can be accessed and drained easier by mercury. Tinni et al. (2012) examined

microcracks in samples as small as GRI particle size from images using a micro-CT scanner which could

contribute to the higher cumulative intrusion volumes in GRI sized samples.
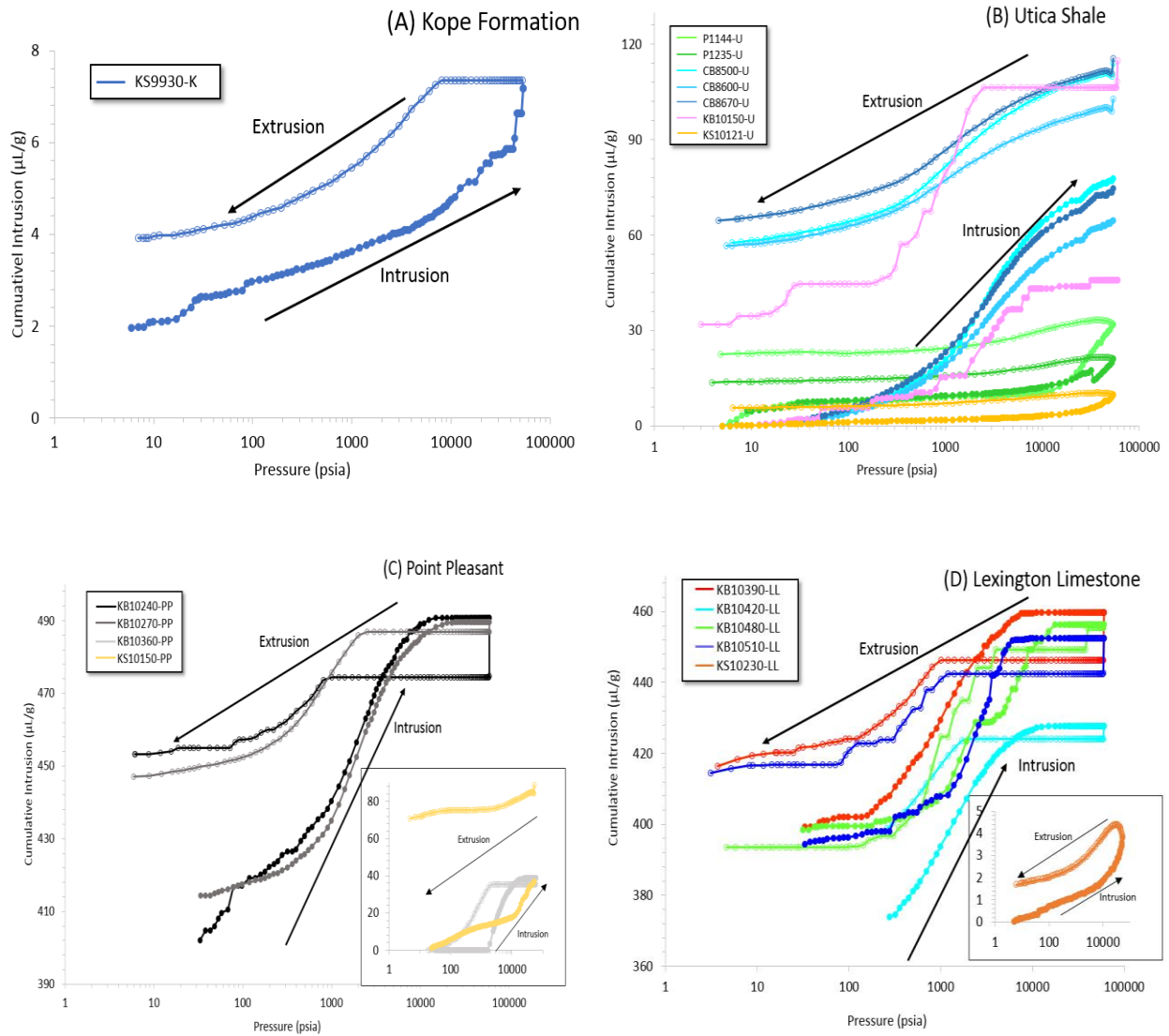
Figure 4-14 Intrusion (closed circles) and extrusion (open circles) curves of mercury versus applied pressure for (A) Kope (B) Utica Shale (C) Point Pleasant (D) Lexington Limestone

When processing the MICP data, inflection points are chosen depending on a switch-over in

intrusion volumes. Each inflection point represents a rapid increased intrusion of mercury into the pore

throats when the pressure has overcome the capillary pressure of a specific pore size. Intrusion within

specific pressures ranges have been correlated to different pore ranges to reflect the various pore

systems. To obtain the pore-throat distribution for each sample, we use the inflection points chosen

with the modified Washburn equation (Figure 4-15).
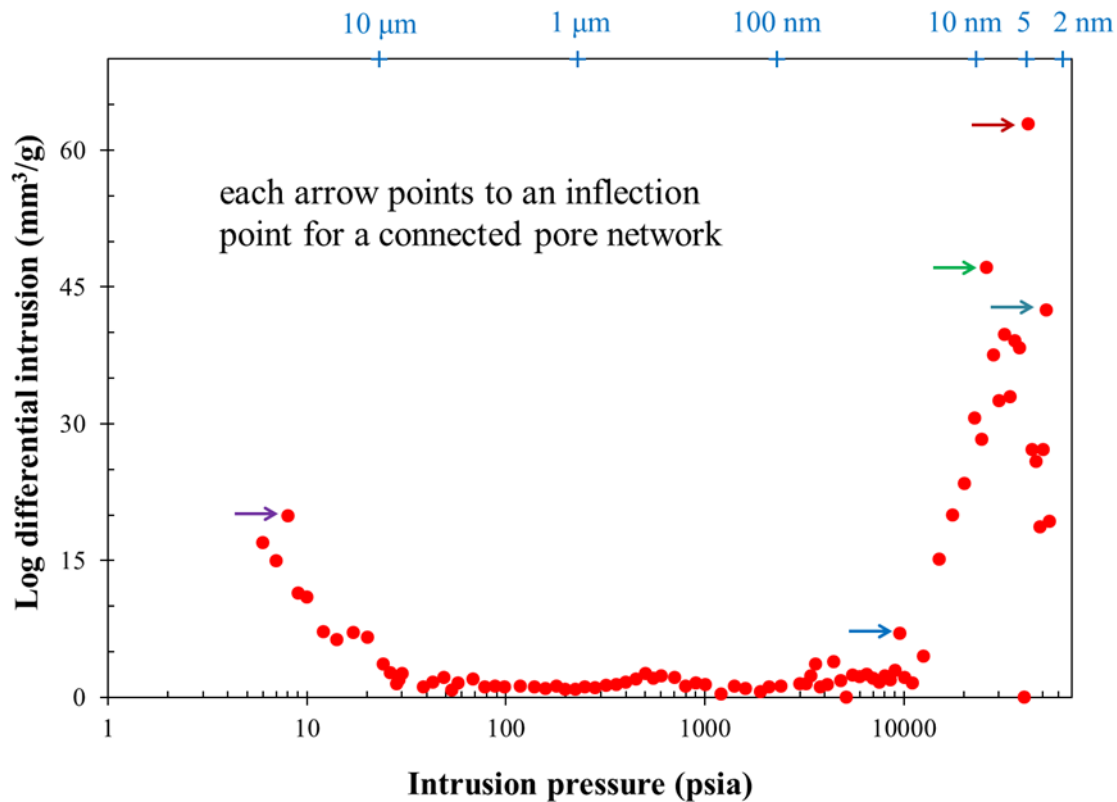
Figure 4-15 Example of chosen inflection points, sample P1144-U

The pore size distribution is displayed in Figure 4-16 (C, D, G, and H) and Table 4-6. Figure 4-16

(A, B, E, and F) shows the incremental intrusion on the y-axis against the pore-throat diameter on the x-

axis. The pore-throat diameters range to represent different ***predominant*** pore systems (Hu et al.,

2017):

- 1000 -1 μm micro-fractures and lamination

- 1-.05 μm intergranular pores

- .05-.01 μm intragranular pores

- .01-.005 μm organic matter-hosted pores

- .005- .0028 μm inter-clay platelet pores

Figure 4-16 (A, B, E, and F) plot the incremental intrusion (μL/g) on the y-axis and pore-throat size range (μm) on the x-axis. These plots indicate that the Kope Formation, Utica Shale, Point Pleasant, and Lexington Limestone possess various pore-throat size distribution.

The Kope Formation samples has a bi-modal pore size range occurring at pore-throats in the range from 2.8 to 5 nm and 10 to 50 nm accounting for nearly 50% of pore volume. The large intrusion spike (Figure 4.15 A) occurs at 730 μm could be a result of a microfracture in the sample.

Multiple pore-throat size distributions are observed in the Utica Shale samples. This could be the result of the heterogeneity of mineralogy, different maturities of samples, and/or the smaller sample sizes (1 cm^3 cube > GRI + > GRI) have more edge-accessible pores. For the immature samples of well Prudential #1-A there is a bi-modal pore-throat size distribution with the majority of porosity in the range of 2.8 to 50 nm and greater than 10 μm accounting for nearly 70% and 30%, respectively. Samples with pores greater than 10 μm could be due to laminations in the sample which would result in a high volume macro-pores (defined as > 50 nm, IUPAC).

Samples from Cadiz B 4H-14, which are in the wet gas window, and sample KB10150-U (Well B) from the dry gas window, observe a bi-modal pore-throat size distribution in the Utica Shale. Porosity is dominated by pores ranging from 10 to 100 nm and 0.1 to 1.0 μm accounting for about 40% and 36% of total pore volume. The highest maturity sample, being from Well A, observed a uni-modal pore-throat size distribution with the majority of porosity accounted for by pore-throats in the range of 2.8 to 10 nm accounting for about 55% of total pore volume.

Again, in the Point Pleasant Formation we see multiple pore-throat size distributions varying from well to well. Samples from Well B observe a uni-modal pore-throat size distribution as porosity is dominated by pore-throats of 0.1 to 1.0 μm accounting for about 40% and 50% for samples KB10240-PP and KB10270-PP, respectively. Sample KB10360-PP has nearly 40% of its porosity accounted for by pore-throats in the range of 0.05 to 0.1 μm. In Well A we observe a bi-modal pore-throat size distribution with porosity in pore-throats in the range of 10 to 50 nm and 0.1 to 1.0 μm accounting for 31% and 24% of total pore volume, respectively.

The Lexington Limestone Formation has multiple pore-throat size distribution. Samples KB10390-LL and KB10420-LL observe a uni-modal pore-throat size distribution with pore-throats in the range of 0.1 to 1.0 μm and 1.0 to 10 μm account for about 60% and 70% of porosity, respectively. Samples KB10480-LL and KB10510-LL have a bi-modal pore-throat size distribution with nearly 80% of porosity being accounted for by pores in the range of 10 to 50 nm and 0.1 to 1.0 μm, and 0.05 to 1.0 μm, respectively. A shift of dominate pore-throat sizes is observed from the clay-rich formations of Kope and Utica Shale to the more carbonate-rich formations of Point Pleasant and Lexington Limestone. The clay-rich formations have more 2.8 to 50 nm (inter-clay platelets, organic-matter, and intragranular) pores, as the more carbonate-rich experience more prevalent amount of ~ 100 nm (intragranular and intergranular) pores.

(A) Kope Formation

(C) Kope Formation

(B) Utica Shale
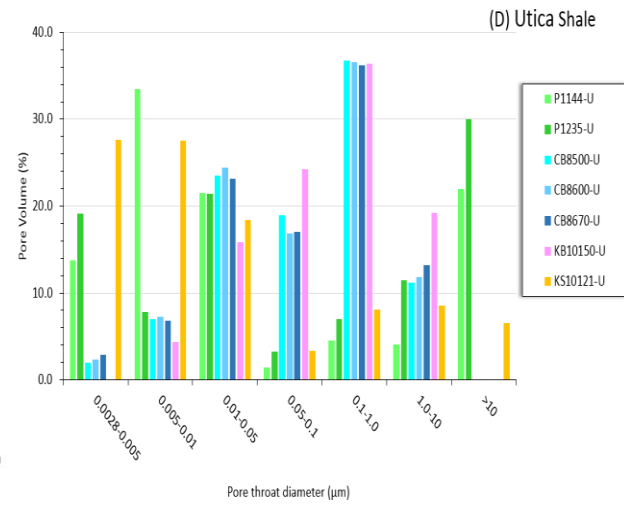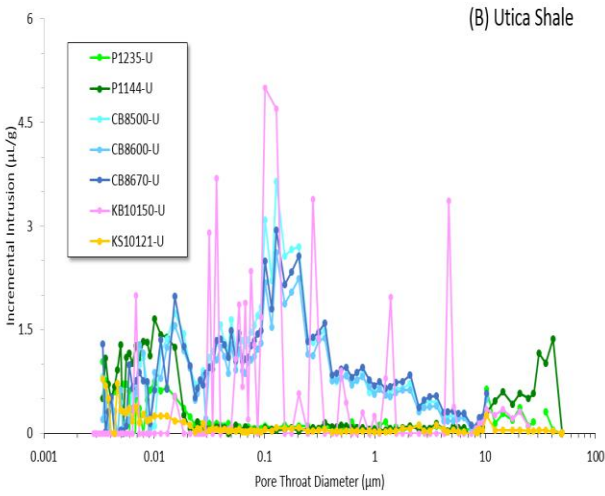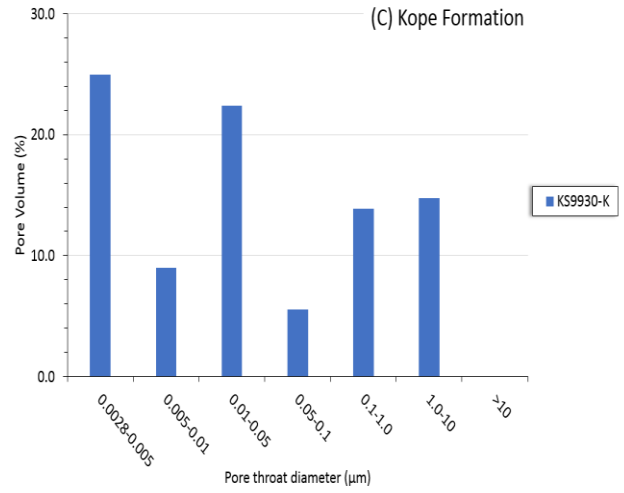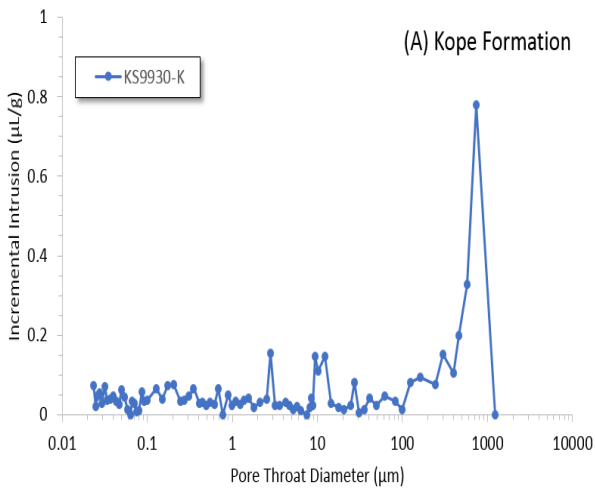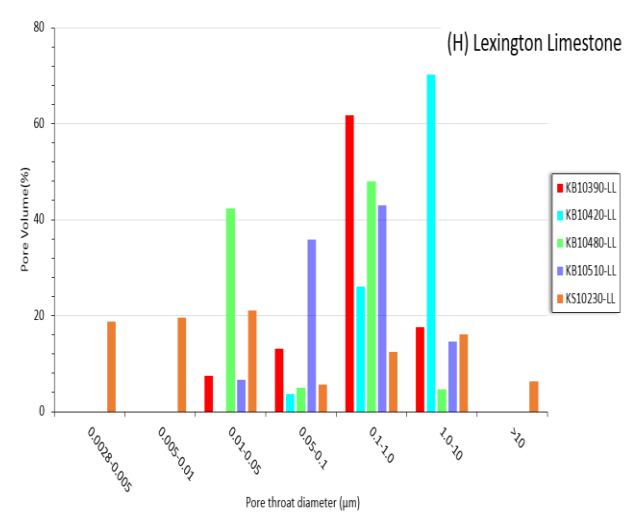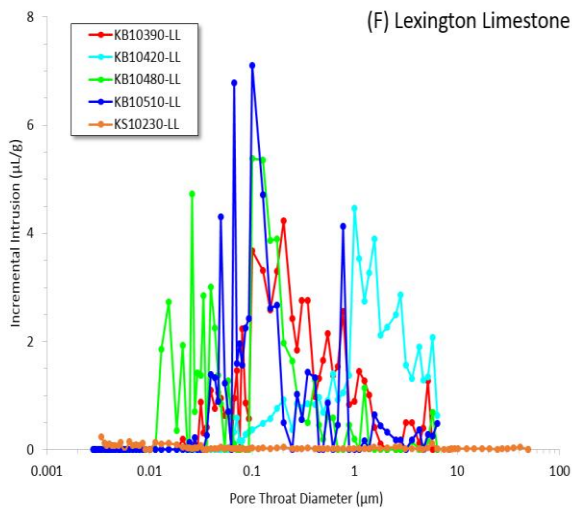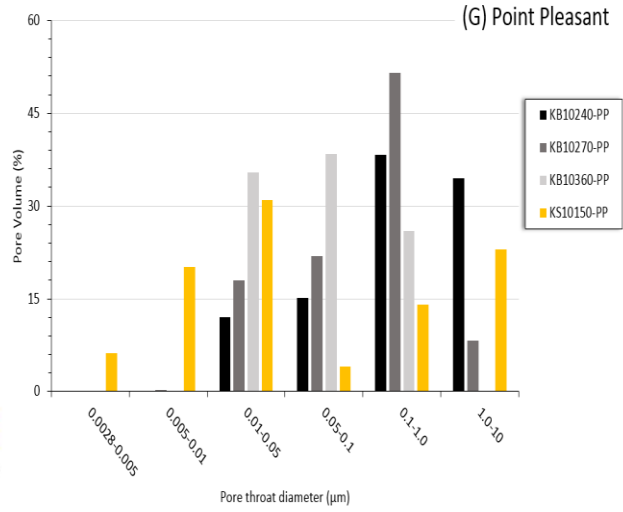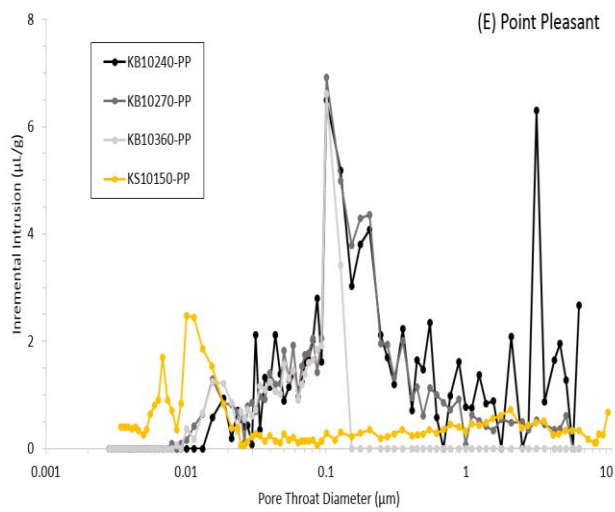
(D) Utica Shale

Figure 4-16 Incremental intrusion and pore volume percentage for Kope Formation (A and C), Utica Shale (B and D), Point Pleasant (E and G), and Lexington Limestone (F and H)

Table 4-6 Pore-throat diamter distribution

Sample ID	Sample Size	Distribution (%) of pore-throat diameter (μm)								
		0.0028-0.005	0.005-0.01	0.01-0.05	0.05-0.1	0.1-1.0	1.0-10	>10	2.8-10 nm	2.8-50 nm
P1144-U	1-cm cube	13.8	33.5	21.5	1.4	4.5	4.1	21.9	47.3	68.8
P1235-U	1-cm cube	19.1	7.8	21.5	3.3	7.0	11.4	30.0	26.9	48.4
CB8500-U	GRI	2.0	7.0	23.5	19.0	36.8	11.2	0	9	33
CB8600-U	GRI	2.4	7.3	24.4	16.9	36.6	11.8	0	10	34
CB8670-U	GRI	2.9	6.8	23.2	17.0	36.2	13.2	0	10	33
KS9930-K	1-cm cube	24.9	9.0	22.4	5.6	13.9	14.7	0	34	56
KS10121-U	1-cm cube	27.6	27.5	18.4	3.3	8.1	8.6	6.5	55.1	73.5
KS10150-PP	GRI	6.2	20.1	31.0	4.1	14.1	23.0	0	26	57
KS10230-LL	1-cm cube	18.8	19.6	21.1	5.6	12.4	16.2	6.4	38.4	59.5
KB10150-U	GRI +	0	4.4	15.8	24.2	36.4	19.2	0	4	20
KB10240-PP	GRI	0	0	12.0	15.1	38.3	34.5	0	0	12
KB10270-PP	GRI	0	0.2	18.0	22.0	51.5	8.3	0	0	18
KB10360-PP	GRI	0	0.2	35.5	38.4	25.9	0.0	0	0	36
KB10390-LL	GRI	0	0	7.6	13.1	61.8	17.5	0	0	8
KB10420-LL	GRI	0	0	0	3.6	26.1	70.3	0	0	0
KB10480-LL	GRI	0	0	42.4	5.0	47.9	4.7	0	0	42
KB10510-LL	GRI	0	0	6.7	35.8	43.0	14.5	0	0	7

Table 4-8 compiles results from MICP experiments. Using the GRI and GRI + size fraction with

the MICP, data was corrected for the conformance effect that mercury needs to fill intergranular pore

space at low pressure, before penetrating the intragranular pores. Overall, the Kope Formation had the

lowest average pore volume (0.005 cm^3/g) and porosity (1.4%). These low values can be linked to its

mineralogy and TOC values as this formation caps the Utica Play. Compared with the Point Pleasant

Formation, which had the highest average pore volume (0.069 cm^3/g), and a high porosity (10.02 %). The

Utica Shale had the highest average porosity (10.5 %) with a high pore volume of 0.046 cm^3/g, as well as

the greatest average total pore area (7.09 m^2/g). The Lexington Limestone has average pore volume of

0.059 cm^3/g, the lowest total pore area average (0.739 m^2/g), and an average porosity of 9.5%. The high

porosity values (e.g. CB8500-U; CB8600-U; CB8670-U; KB10240-PP; KB10270-PP; KB10390-LL to

KB10510-LL) of greater than 10 % could be a result of the sample size used. Tinni et al. (2014) conducted

an experiment on different particle sizes ranging from 5.7 to 0.7 mm, and he found that the MICP

porosity values will vary greatly depending on particle sizes used and a noticeable increase in MICP

porosity was observed between 1.6 mm (GRI +) and 0.7 mm (GRI) particle sizes.

Permeability and tortuosity is inferred by using the same inflection points used for the pore-

throat distribution. Both harmonic and geometric permeability are presented in Table 4-8 to consider

the multiple connected pore networks. The geometric mean considers the weighing of pore volume and

the harmonic favors the smallest values. The Kope Formation has the smallest harmonic permeability of

3.19 nD while the Utica Shale has the highest average harmonic permeability of 11,000 nD. The average

harmonic permeability for the Point Pleasant is 5800 nD and for the Lexington Limestone is 2460 nD.

The geometric permeability is comparable to most samples' harmonic permeability, except for the

anomalous value for sample KB10240-PP (1.06E+11 nD). The Lexington Limestone produces the highest

average geometric permeability of 189,000 nD while the Kope Formation has the lowest average

geometric permeability of 16,000 nD. The average geometric permeability for the Utica Shale and Point

Pleasant Formations were 7900 nD and 2200 nD, respectively. The variance in our permeability results

could be due to the particle size used in experiment. Tinni et al. (2014) found that when particle size

decreases, access to larger pores increases, while apparent permeability decreases because of a

reduction in gas slippage. Yet, our results (Table 4-7) display that as sample size decreased within a

formation, average permeability increased.

Table 4-7 Average permeability for formations

Formation	Sample Size	Average Permeability (nD)	
		Geometric	Harmonic
Kope	1-cm cube	15949	3.19
Utica	1-cm cube	2139	9.6
	GRI +	46528	830
	GRI	877	25370
Point Pleasant	GRI	2.22E+03	5829.7
Lexington Limestone	1-cm cube	20.5	1.24
	GRI	237302	30728

Effective and geometric tortuosities for the meso-pore network (2.8 to 50 nm) are presented in Table 4-8. Effective tortuosity is the average topological distance between two arbitrary points in the sample, and geometric tortuosity is the ratio of the average length of the geometric flow paths through the medium to the straight-line length, across the medium (Ghanbarian et al., 2013). Tortuosity was not able to be calculated for GRI/GRI + samples. The Kope Formation had the highest effective and geometric tortuosity values of 149,253 and 45.5, respectively. The Utica Shale observed the lowest average effective tortuosity of 5603 and an average geometric tortuosity of 15. The Lexington Limestone observed the smallest geometric tortuosity of 7.84 and an effective tortuosity of 2452. Sample KS9930-K observed the highest effective and geometric tortuosity suggesting that the fluid path would experience a very convoluted pathway between pore to pore.

Sample ID	Sample size	Bulk Density (g/cm³)	Apparent (skeletal) density (g/cm³)	Total pore area (m²/g)	Total pore volume (cm³/g)	Porosity (%)	Median pore-throat diameter (nm)		Average pore-throat diameter (nm) 4V/A	Geometric Permeability (nD)	Harmonic Permeability (nD)	2.8-50 nm pore-throat network	
							Volume	Area				Matrix Toruosity (Do/De)	Geometrical Toruosity (Le/L)
P1144-U	1-cm cube	2.38	2.58	14.5	31.9	7.61	8.50	8.5	5.2	466	14.3	4362	18.2
P1235-U	1-cm cube	2.48	2.61	6.97	21.1	5.20	56.0	56.0	4.0	5894	9.60	8077	20.4
CB8500-U	GRI	2.24	2.70	7.62	77.4	17.3	183	9.4	40.6	860	161	17153	54.5
CB8600-U	GRI	2.29	2.69	6.20	64.1	14.7	339	8.2	41.4	569	66.4	26799	62.8
CB8670-U	GRI	2.24	2.68	7.27	74.2	16.6	316	7.3	40.9	1201	75882	21235	59.3
KS9930-K	1-cm cube	2.64	2.68	1.45	52.2	1.39	204	3.9	14.4	15949	3.19	149253	45.5
KS10121-U	1-cm cube	2.55	2.61	5.49	9.80	2.50	16.1	4.2	7.2	58.4	4.86	4370	6.58
KS10150-PP	GRI	2.36	2.59	4.81	73.8	8.61	409000	6.0	30.3	63.1	30.3	32240	52.7
KS10230-LL	1-cm cube	2.62	2.64	1.55	3.80	0.99	6.70	4.3	9.8	20.5	1.24	2452	7.84
KB10150-U	GRI +	2.08	2.30	1.55	45.7	9.50	217501	27.4	118.2	46528	830	121938	107.0
KB10240-PP	GRI	1.71	2.07	0.76	88.7	15.1	273296	41.4	466.4	1.06E+11	18279	37059	74.9
KB10270-PP	GRI	2.01	2.37	0.79	75.3	15.2	252710	33.7	382.2	6359	4758	13988	46.1
KB10360-PP	GRI	1.13	1.14	4.33	38.6	1.18	512	27.0	35.7	251	251	6.04	0.27

KB10390-LL	GRI	2.06	2.37	0.29	60.5	12.5	236164	62.1	848.7	545838	15300	41374	71.8
KB10420-LL	GRI	2.13	2.40	0.72	116	11.5	218592	50.2	65.0	386251	102034	11632	36.5
KB10480-LL	GRI	1.88	2.11	0.75	57.9	10.9	231261	21.3	311.1	1120	342	60069	80.8
KB10510-LL	GRI	2.03	2.33	0.40	58.0	11.8	231507	51.6	583.2	15999	5234	16580	44.1

Table 4-8 Compliation of pore structure characteristics from MICP

4.5 Helium Porosity and Permeability of Core Plugs

Table 4-9 displays the results from helium porosity. Due to the sample size needed for this experiment (e.g. core plugs) only samples from Well A were tested excluding sample KS10150-PP. The samples were taken transverse to bedding plane. Sample KS10150-PP could not be cored for a plug as it was too brittle and fractured easily. When compared to MICP results, the porosity values similar being within ± 0.1 % for sample KS9930-K and KS10230-LL and with ± 0.9 % for sample KS10121-U. All samples were found to have very low porosity. Sample KS10121-U (Utica Shale) had the highest porosity of 1.62 %, and sample KS10230-LL (Lexington Limestone) had the lowest porosity of 1.14 %. Sample KS9930-K has a porosity of 1.52 %.

Table 4-9 Comparison of porosity from two methods

Sample ID	Helium		MICP	
	Sample (cm-plug)	Porosity (%)	Sample Size	Porosity (%)
KS9930-K	2.51 diameter x 3.89 height	1.52	1-cm cube	1.39
KS10121-U	2.50 diameter x 2.96 height	1.62	1-cm cube	2.50
KS10230-LL	2.51 diameter x 3.27 height	1.14	1-cm cube	0.99

Samples were also found to have very low permeability (Table 4-10). Sample KS10230-LL has a k klinkenberg corrected permeability of 2026 nD and samples KS9930-K and KS10121-U have a k klinkenberg corrected permeability of 1013 nD. The latter two of the three samples reach the lower detection limit of the apparatus to measure permeability indicating that the matrix permeability could be lower. MICP geometric and harmonic permeability were much lower than the k klinkenberg corrected permeability suggesting that samples KS9930-K and KS10121-U have permeability lower than 1000 nd, the plug-k detection limit.

Table 4-10 Comparison of permeability from two methods

Sample ID	Helium		MICP		
	Sample (cm-plug)	k Klinkenberg (nD)	Sample Size	Permeability	
				Geometric (nD)	Harmonic (nD)
KS9930-K	2.51 diameter x 3.89 height	1013	1-cm cube	15949	3.19
KS10121-U	2.50 diameter x 2.96 height	1013	1-cm cube	58.4	4.86
KS10230-LL	2.51 diameter x 3.27 height	2026	1-cm cube	20.5	1.24

4.6 Low Pressure Nitrogen Gas Physisorption

Only samples from well Prudential #1-A and CB8600-U were tested for this experiment, all of which are from the Utica Shale. The characteristic isotherm shape of the Utica Shale samples in Figure 4-17 all exhibit type II isotherms according to the classification of Sing (1985). The rapid gas adsorption volume increase at low relative N_2 pressure (<0.05) suggest the filling of micropore (< 2 nm) and mesopores (2-50 nm). As the relative pressure increases from 0.05 to 0.95 the adsorb gas volume is slowly increasing at the stage of mesopore filling and capillary condensation. When the relative pressure is at its max of about 1.0, another rapid increase in gas adsorption volume is observed. This is indicative of the presence of macropores or fractures.

Obvious hysteresis loops are observed in all samples. Open pores and especially bottleneck pore can produce hysteresis (Zhang et al., 2016). Samples from well Prudential #1-A can be classified by type H2 and sample CB8600-U by type H3 according to the classification presented by Sing (1985). Type H3 is indicative of a large volume of mesopores while type H2 is indicative of various distribution of pore types and pore diameter. The presence of meso- and macropores is consistent with MICP data.
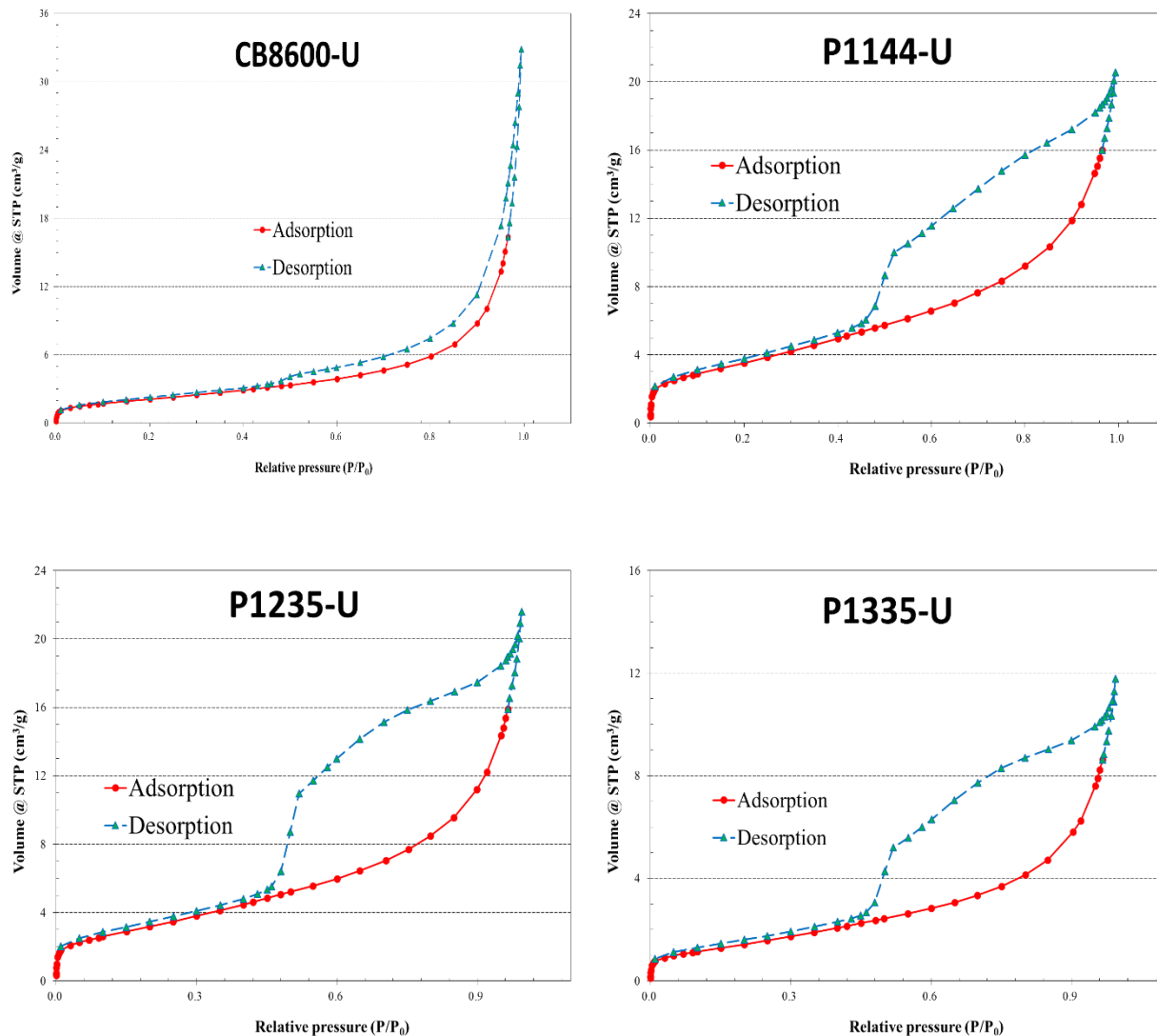
Figure 4-17 Gas sorption isotherm profiles for samples tested

Figure 4-18 exhibits the cumulative pore volume and incremental pore volume. Sample CB8600-U has one obvious peak at about 4 nm but also has a large volume pores in the range of 5 to 15 nm. Samples from well Prudential #1-A all show a similar unimodal distribution with a peak at about 4 nm.
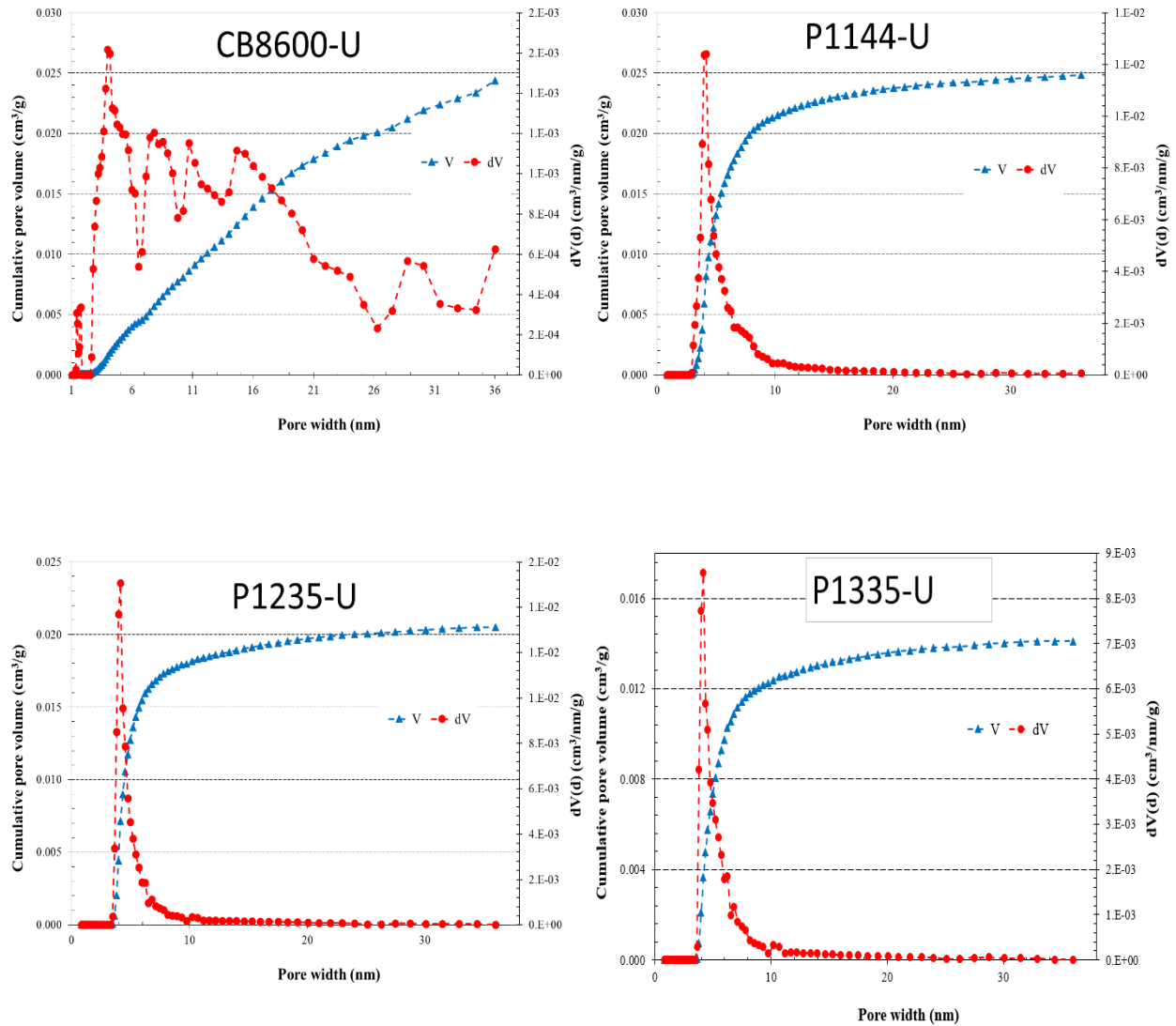
Figure 4-18 Cumulative and incremental pore volume

4.7 Contact Angle

As discussed in the methods section, contact angle between sample surface of various liquids and fluid can be used to assess the wettability of samples. Data was recorded for the sample from initial contact till there was no more change in contact angle or fluid was imbibed into sample. An example of raw data is presented in Figure 4-19, and Figure 4-20 presents an example of the final results for contact angle of four fluids plotted versus log time. The fluids used were DI water, API brine, 20% IPA, and n-decane. The contact angle results are presented in Table 4-11 were taken at the 30 second after fluid

rock contact. As n-decane quickly spreads out onto sample surface within 1 second; as result, contact

angle recorded was initial angle measured. The detection limit of the interfacial instrument is 3 degrees,

in that case such a value was recorded for contact angle.

Figure 4-19 Before and after droplet of fluid on to sample surface, sample P1336-U 20%IPA
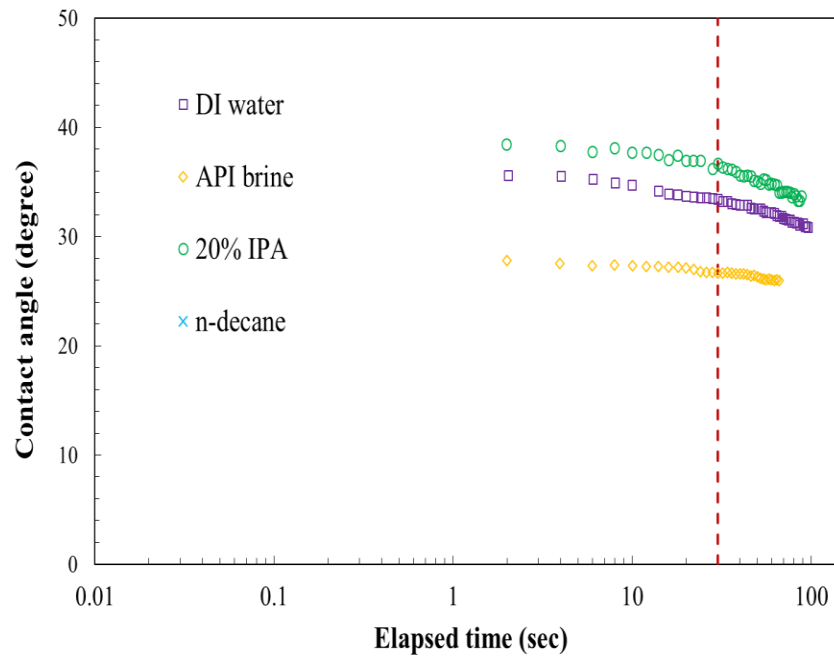
Figure 4-20 Contact angle versus log time for various fluids on sample P1336-U

The results of contact angle on sample surface display excellent wetting to n-decane, yet also shows good wetting to the other fluids (DI water, API brine, and 20% IPA). The relatively low contact angle for DI water, API brine, and 20% IPA could be related to the high clay content. For API brine, the highest contact angle measured was 49° for sample KS10121-U, and the lowest contact angle was the detection limit of 3° for sample P1235-U. For 20% IPA, the highest contact angle measured again was for KS10121-U at 36°, and the lowest contact angle measured was the detection limit of 3° for sample KS10150-PP. This indicates that samples are wetting to all fluids. Even though n-decane fluid had the lowest contact angle measured, samples may be more represented by a mixed-wetting where mineral deposits between grains promote continuous oil-wetted paths or dalmatian wetting where connate water might isolate oil-wetted surfaces (Lake, 2007). Mineralogy influence on wetting characteristics will be further assessed in the discussion section.

Table 4-11 Summary of contact angle after 30 sec for DI water, API brine, and 20% IPA, and after 1 sec for n-decane

Sample ID	Contact angle (4 fluids) (degrees)			
	after 30 sec			after 1 sec
	DI Water	API Brine	20% IPA	n-decane
P1144-U	-	27.64	16.24	3
P1235-U	15.27	3	29.42	3
P1336-U	33.46	26.68	36.69	7.84
KS9930-K	-	31.42	20.47	3
KS10121-U	-	49.49	36.34	10.71
KS10150-PP	-	24.52	3	10.81
KS10230-LL	-	36.55	18.79	10.13

4.8 Spontaneous Fluid Imbibition

For spontaneous fluid imbibition, both DI water and n-decane were run on the samples to probe pore connectivity along with the interaction between different fluids in the sample. Table 4-12 contains a summary of results obtained from DI water and n-decane imbibition experiments.

Table 4-12 Imbibition results for two fluids DI water and n-decane

Sample ID	Slope	DI Water			Stage II Slope	n-decane	Predicted k (nD)
		6 hr	12 hr	24 hr		Stage II Slope	
P1144-U	1	0.869 ± 0.605	0.254	2.121	0.225 ± 0.059	x	51
	2	0.280 ± 0.146	0.244	0.284		0.401	
	3	x	x	0.002		x	
P1235-U	1	0.536 ± 0.231	0.487	0.153	0.238 ± 0.058	x	5.5
	2	0.243	0.148	0.076		0.621	
	3	x	0.101	0.043		x	
P1336-U	1	0.724 ± 0.05	2.737	0.679 ± 0.390	0.310 ± 0.179	x	2.6
	2	0.246 ± 0.213	0.715	0.135 ± 0.082		0.869	
	3	x	x	0.013		0.361	
KS9930-K	1	1.593 ± 1.994	6.291	0.981	0.226 ± 0.011	x	75.2
	2	0.158 ± 0.030	0.519	0.114		0.564	
	3	x	x	x		x	
KS10121-U	1	1.048	4.558	0.438	0.220 ± 0.038	x	0.3
	2	0.221 ± 0.195	0.251 ± 0.131	0.130		0.648 ± 0.233	
	3	x	x	x		-0.037	
KS10230-LL	1	0.922 ± 0.683	1.351 ± 0.058	1.263	0.300 ± 0.086	x	0.003
	2	0.272 ± 0.021	0.152 ± 0.065	0.292		0.687 ± 0.114	
	3	x	x	x		0.104	

Based on the slope characteristics from Figure 4-21 thru Figure 4-26, the DI water imbibition behavior can generally be divided into two stages: initial noisy stage (Stage I) and linear imbibition stage (Stage II). The steep and noisy initial slope Stage I is due to the sample first coming into contact with the fluid, and occurs within the first few minutes. This rapid increase of cumulative imbibition height would also be caused by boundary effects caused by larger pores and pore-throats exposed at sample surface (Yang et al., 2017). Stage II occurs when linear slopes are observed in the plot of log cumulative imbibition height vs. log imbibition time, and this slope we can relate to its pore connectivity. In various samples, we did experience two different slopes during Stage II for DI water (i.e., Figure 4-22 B, C) which may reflect the complex connectivity and wettability for the shale composition. Stage II slopes usually occurred within the first minute and continued the rest of the experiment. Most of samples run with DI water did not reach the top of the sample as indicated by the behavior of the imbibition curves continue to increase during the late imbibition process, but in some cases (i.e., Figure 4-22 B) fluid did reach the top of the sample as indicated by the lower slope in Stage III.

From our DI water imbibition results, imbibition slopes in Stage II range from 0.175 to 0.364 in well Prudential #1-A and 0.152 to 0.385 in Well A. Both wells produced Stage II slopes that are indicative of poorly connected pore network towards DI water. For well Prudential #1-A we see an increase in Stage II slope with depth and all samples from this well are Utica Shale in the low maturity range. As compared to the Utica Shale sample from Well A, high maturity sample KS10121-U, has a slope with an averaged Stage II slope of 0.220 ± 0.038. In Well A, sample KS10230-LL, has the highest slope of 0.300 ± 0.086.

Unlike DI water, n-decane imbibition behavior generally produces three stages: initial rapid increasing and noisy stage (Stage I), linear imbibition stage (Stage II), and late plateau stage (Stage III).

Stage I was particularly noisy when compared to Stage I of DI water. The imbibition curve rapidly

increased, which is attributed to the sample may be unstable and/or boundary effects, but then for

most of our samples was followed by a rapid decrease. After about 10 minutes a linear Stage II slope

was observed in all samples. With a slope close to zero, Stage III occurs when the fluid has reached the

top of the sample though it will continue to be imbibed into the sample's nano-sized matrix until it

completely fills the available pore space (Yang et al., 2017).

From our n-decane results, imbibition Stage II slopes range from 0.401 to 0.869 in well

Prudential #1-A and 0.564 to 0.687 in Well A. Both produce Stage II slopes around 0.5 which are

indicative of a well-connected pore system towards n-decane and suggest a classical Fickian behavior

(Hu et al., 2012). Again, in Well A there is an increase of slope with depth. As stated in the methods

section, a predicted permeability can be calculated with imbibition slopes near 0.5 (shown in Table 4-

12). In well Prudential #1-A and Well A, permeability decreases with depth from 51 nD to 2.6 nD and in

Well A from 75.2 to 0.003 nD. The lower Stage II slopes for n-decane runs produces lower predicted

permeability. As n-decane is attracted to the hydrophobic organic-matter pores it will preferentially

imbibe into them. This may explain the rapid increase in Stage I and high Stage II slope values as n-

decane rapidly invades the macro- and meso-pore network of the sample.

Our results show that the samples show different wettability attractions for different fluids. Our

organic-rich Utica Shale and other upper Ordovician members show good connectivity for n-decane

fluid, and sparse connectivity for DI water. The slopes from our imbibition results suggest that the

wettability of our samples are oil-wet to mixed-wet in nature, but the oil-wet regions are better

connected than the water-wet regions.
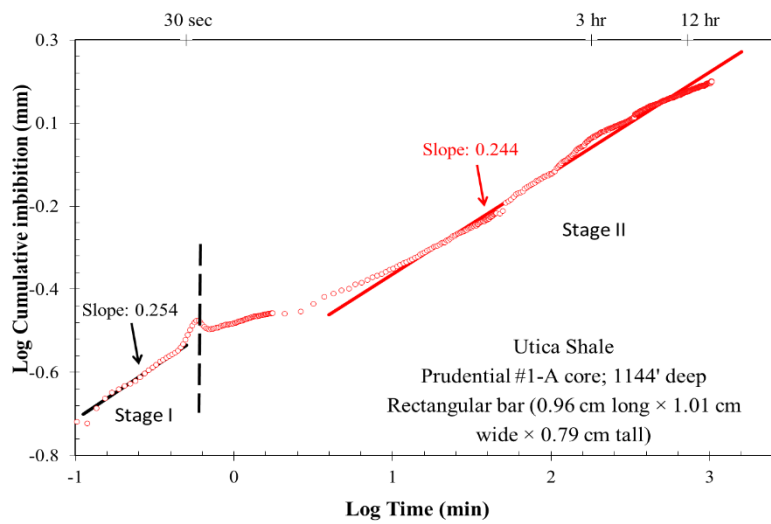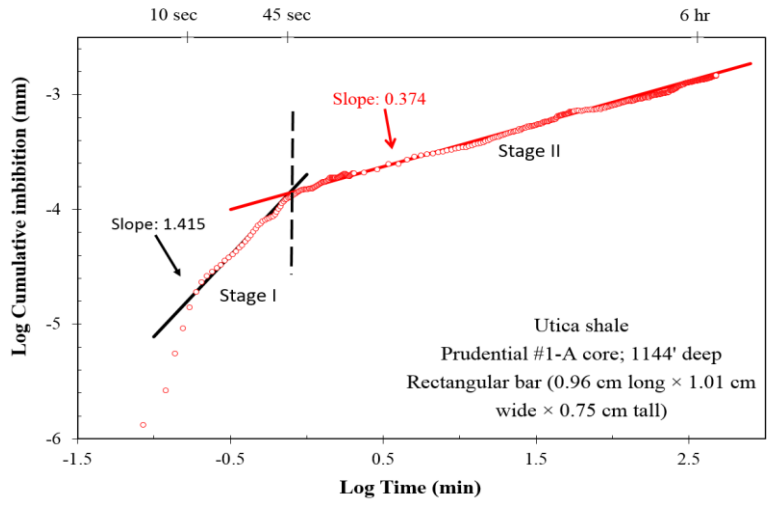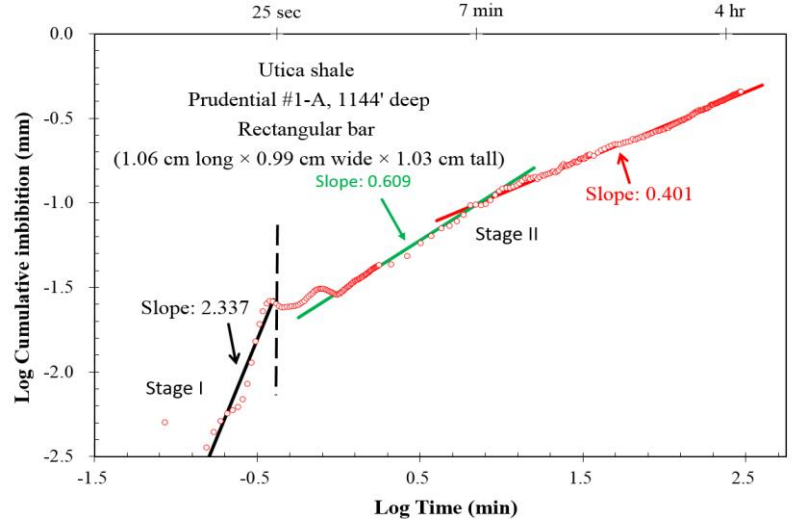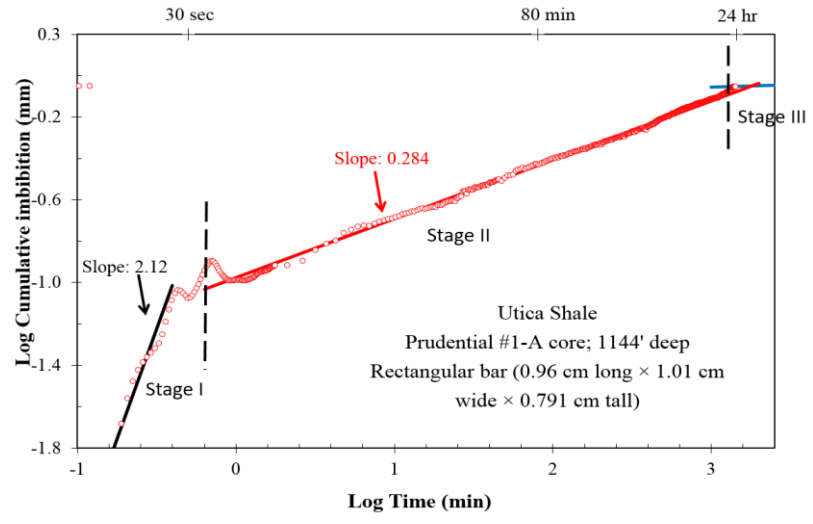
Figure 4-21 Imbibition curves for P1144-U. A) DI water 6 hr; B) DI water 12 hr; C) DI water 24hr; D) n-decane 4 hr
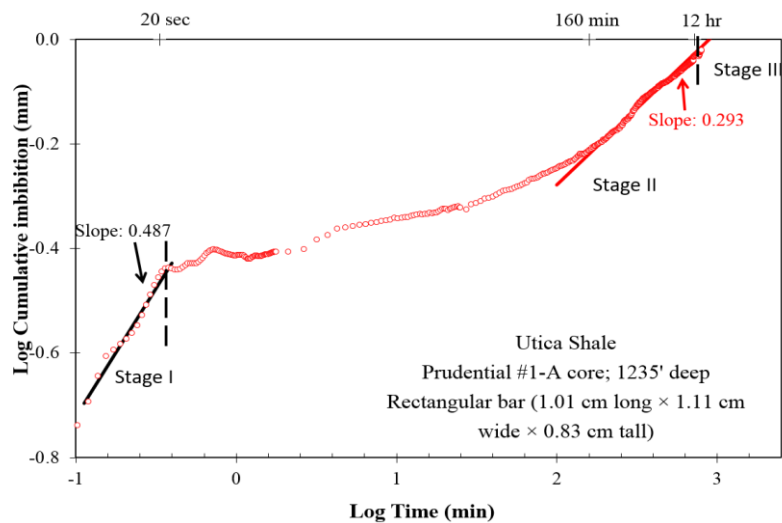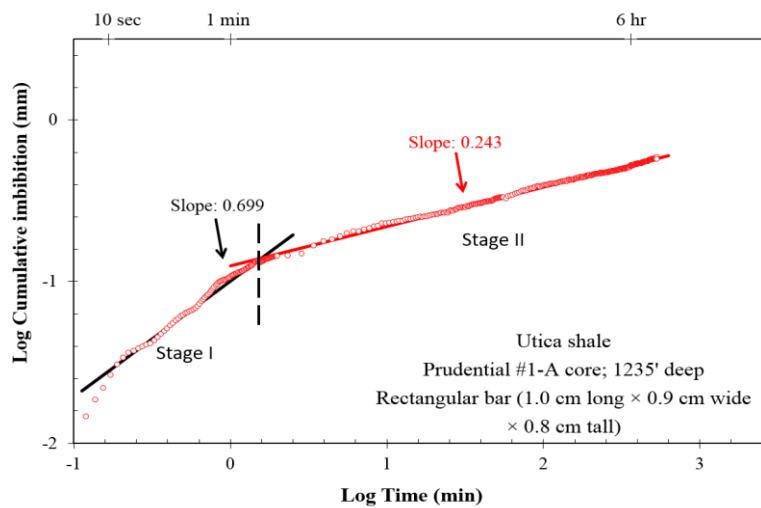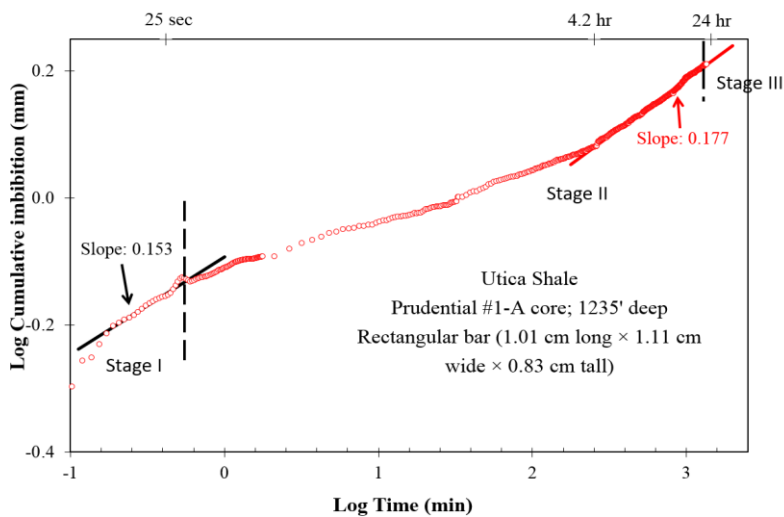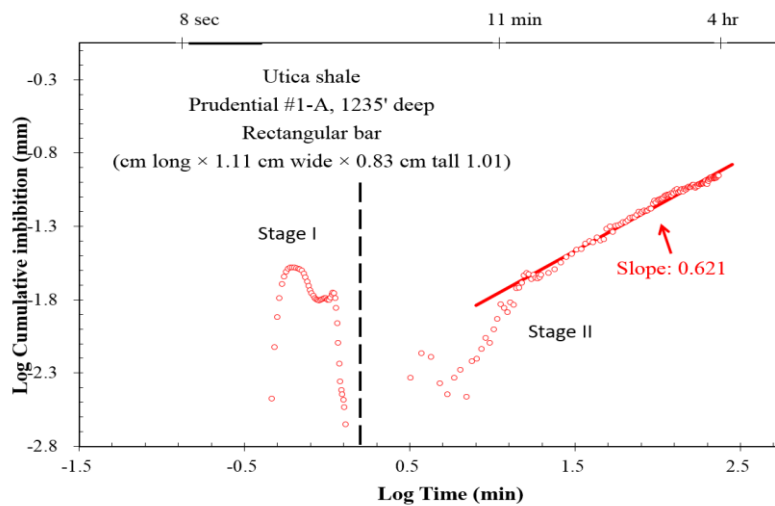
Figure 4-22 Imbibition curves for P1235-U. A) DI water 6 hr; B) DI water 12 hr; C) DI water 24hr; D) n-decane 4 hr
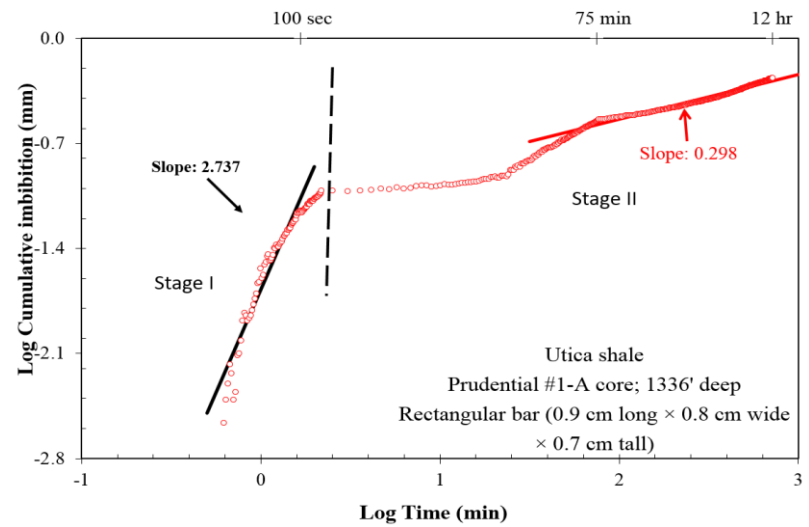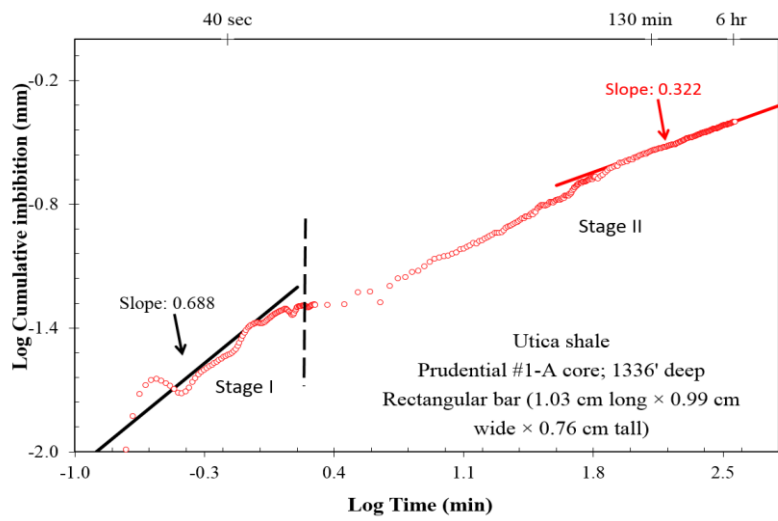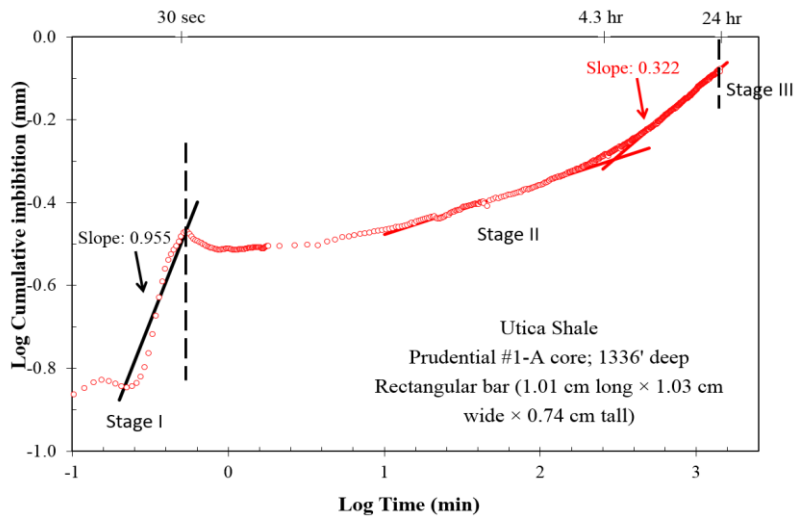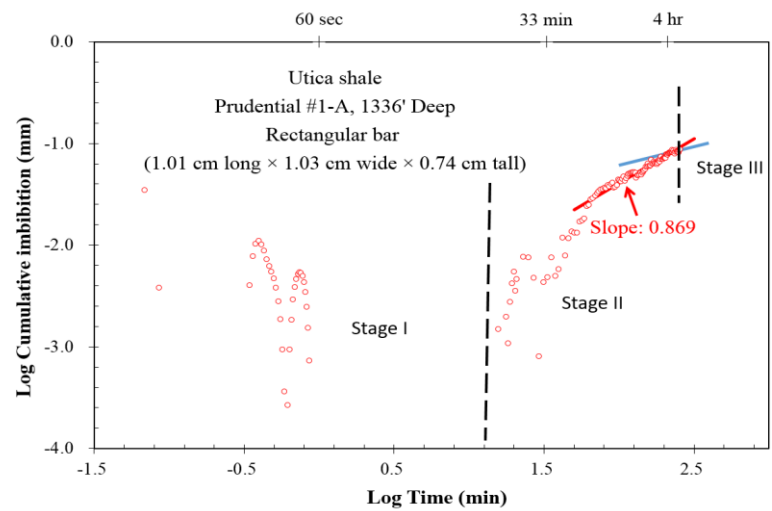
Figure 4-23 Imbibition curves for P1336-U. A) DI water 6 hr; B) DI water 12 hr; C) DI water 24hr; D) n-decane 4 hr
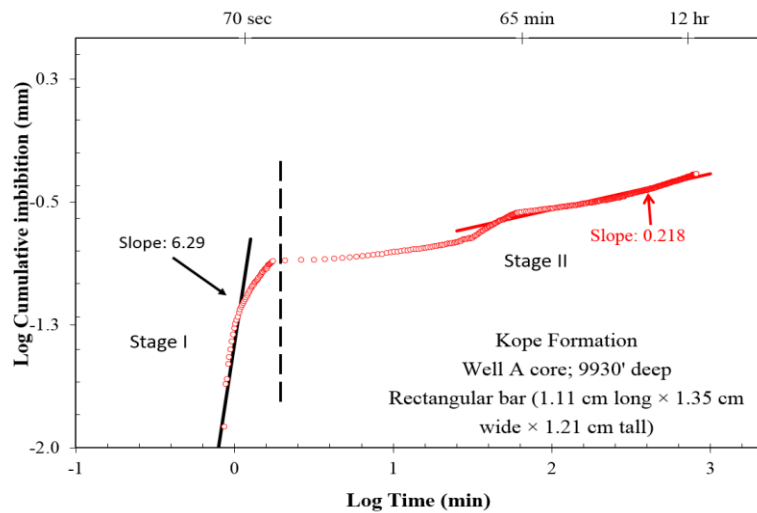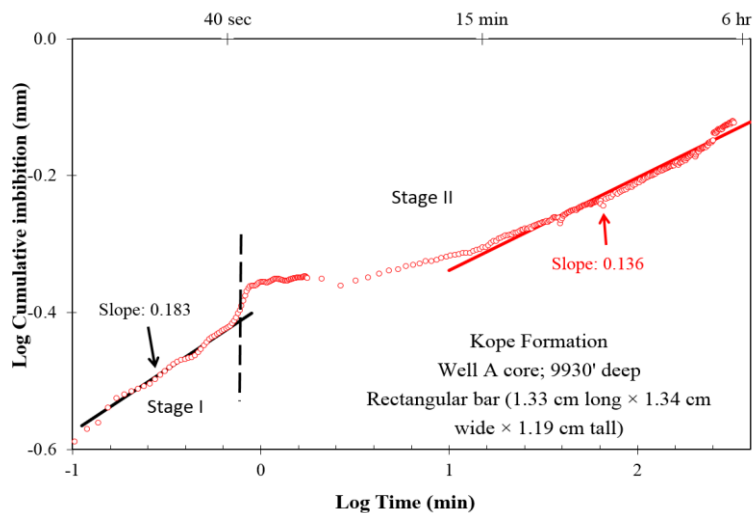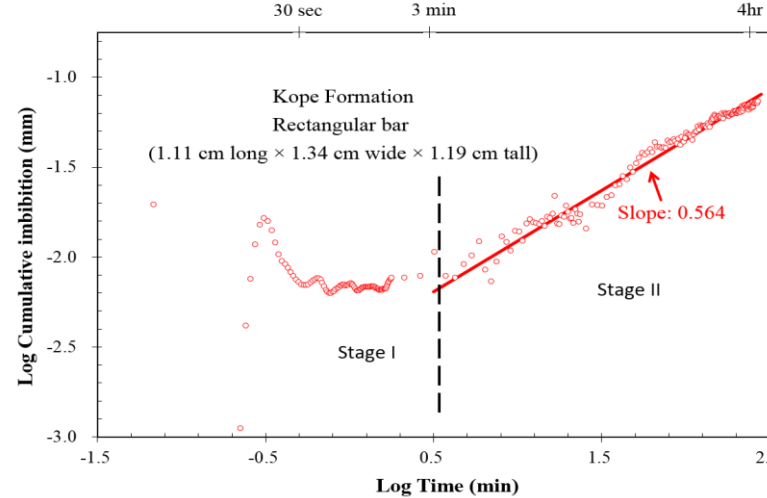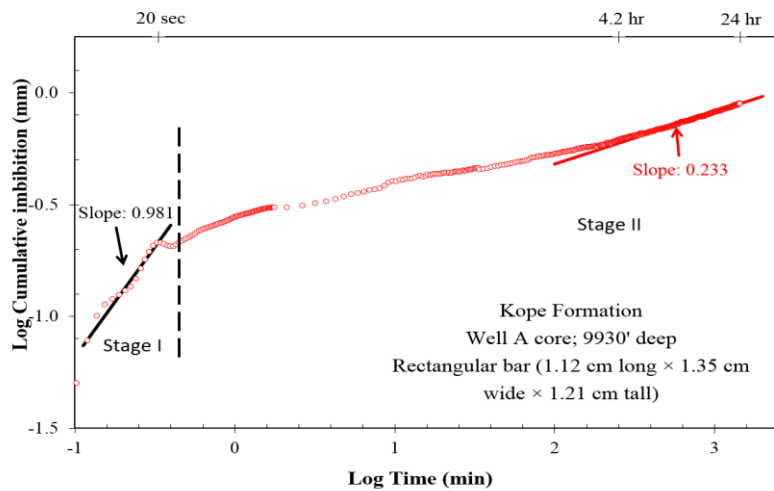
Figure 4-24 Imbibition curves for KS9930-K. A) DI water 6 hr; B) DI water 12 hr; C) DI water 24hr; D) n-decane 4 hr

90
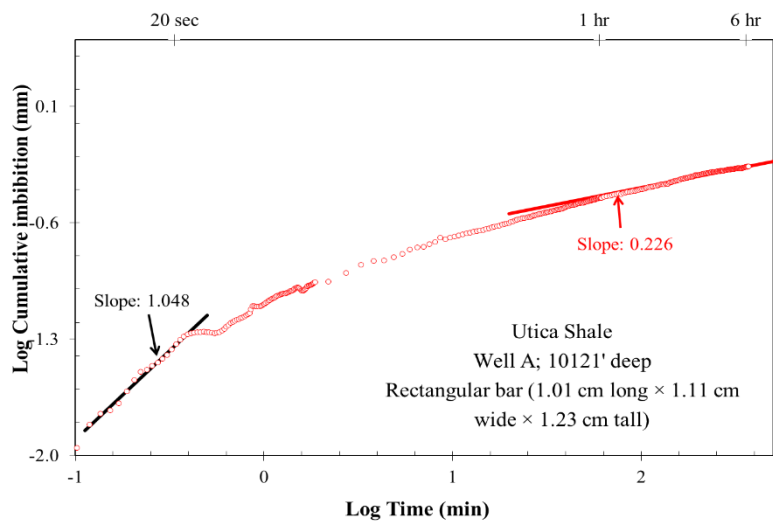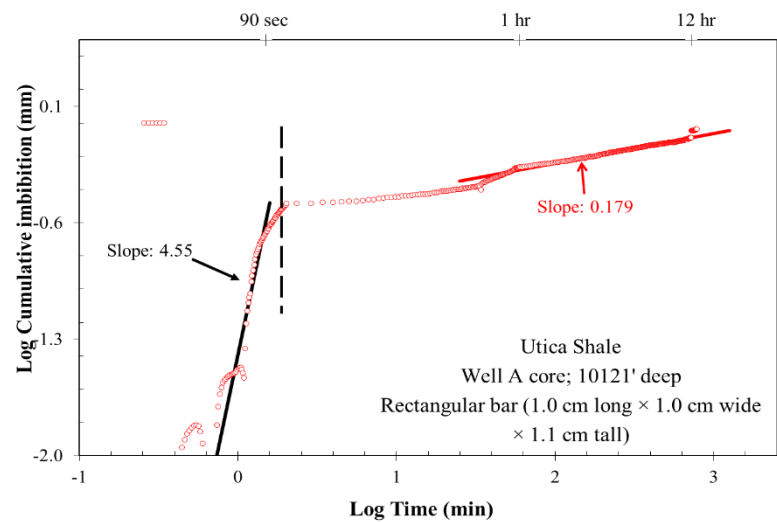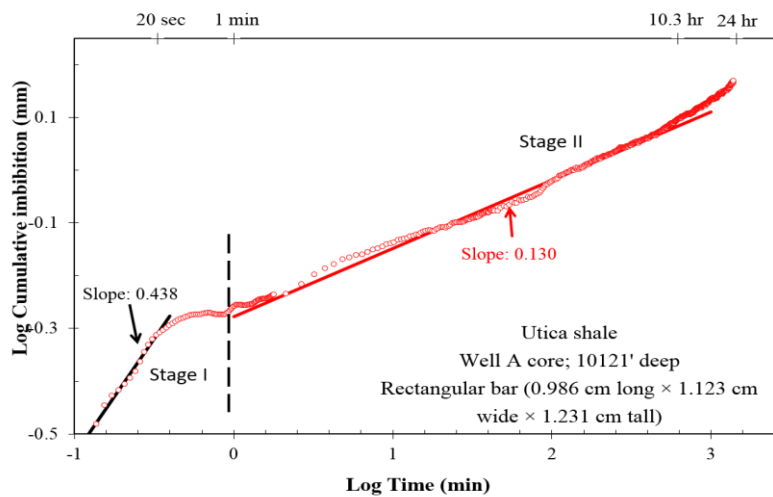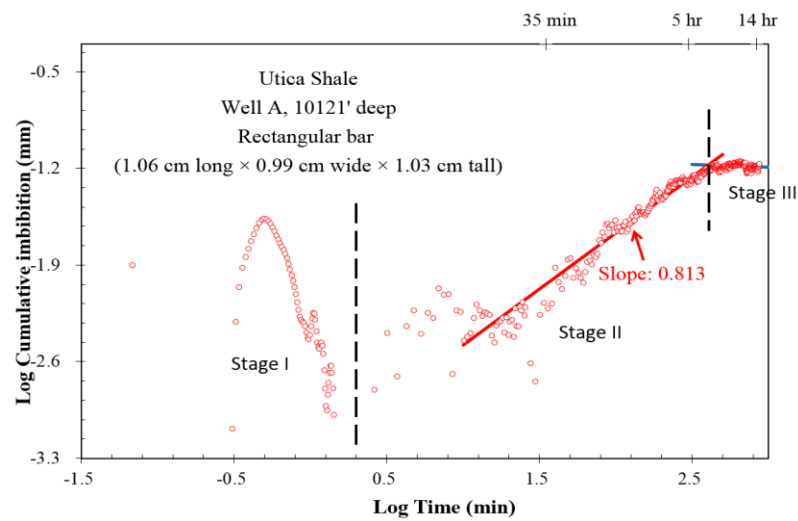
Figure 4-25 imbibition curve for KS10121-U. A) DI water 6 hr; B) DI water 12 hr; C) DI water 24hr; D) n-decane 4 hr
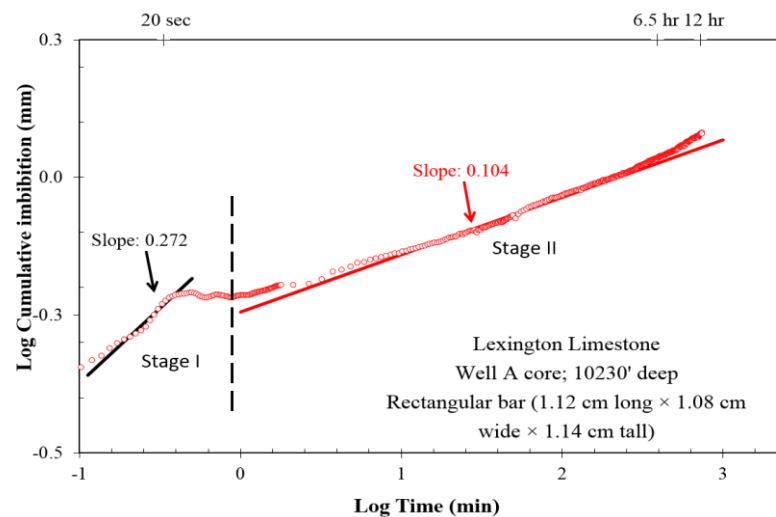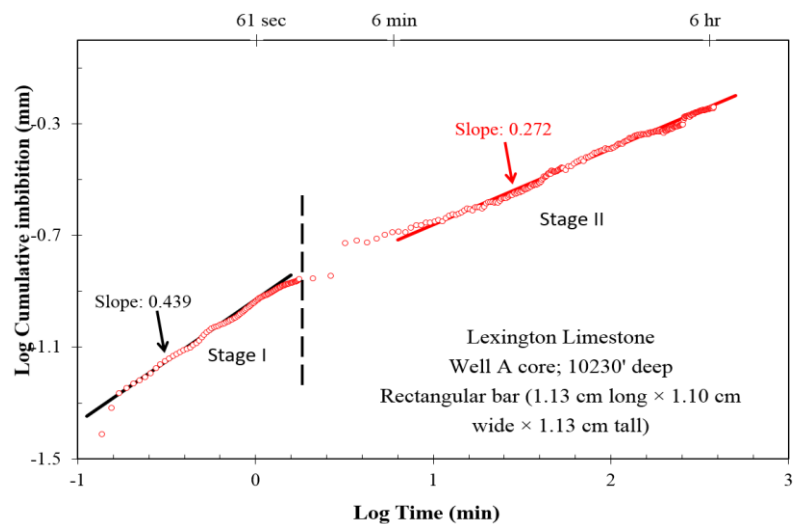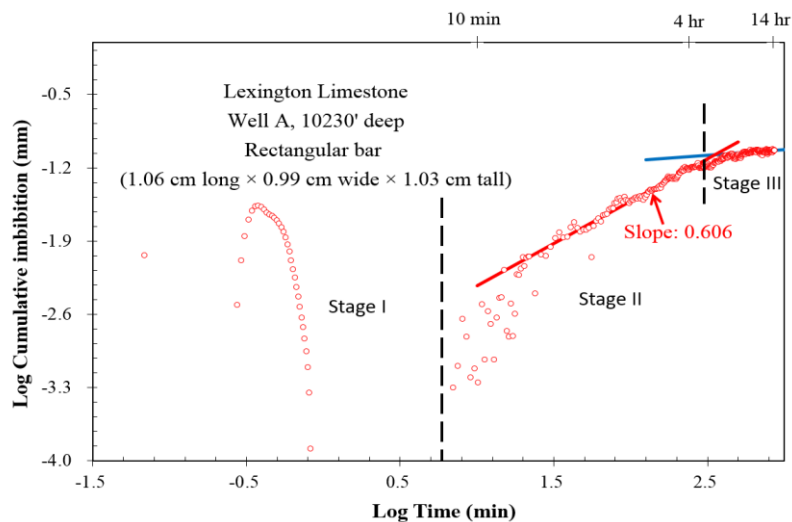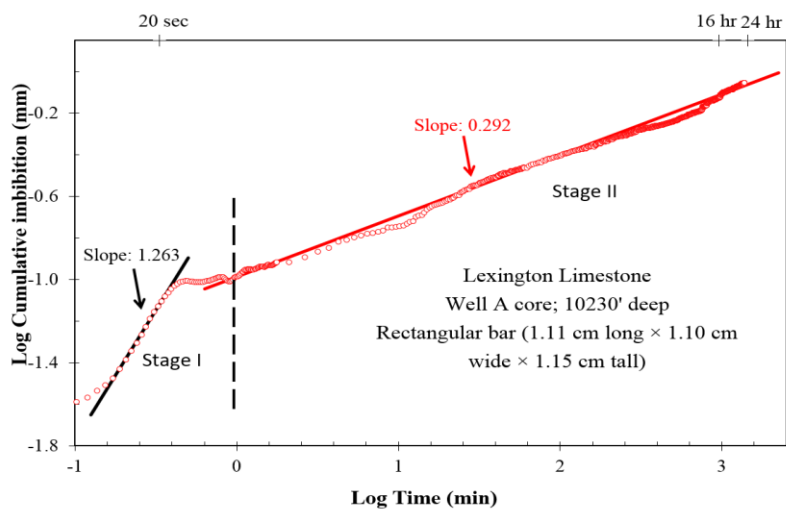
Figure 4-26 Imbibition curves for KS10230-LL. A) DI water 6 hr; B) DI water 12 hr; C) DI water 24hr; D) n-decane 4 h

4.9 Production Data

All the wells except for Prudential #1-A have production data from initial production to December 2016. Well A, Well B, and Cadiz B 4H-14 are all currently producing gas while Cadiz B 4H-14 is also producing oil (Table 4-13). The producing formation for these three wells is the Point Pleasant. Well A initially produced nearly 300,000 mcf per month. Yet after a couple months of keeping this production rate, Well A production started to consistently decline till the end of 2016 in producing 2,500 mcf per month. From the year 2014 to 2015, Well A experienced a 73% decrease in first year production. Well B initially produced about 230,000 mcf per month and after 10 months increase to producing 310,000 mcf per month. This was followed by a production decline to produce 120,000 mcf at the end of 2016 with a first-year production decline of 47%. Cadiz B 4H-14 had the lowest initial production starting at 170,000 mcf per month and after 12 months produced a 12% first year increase of production. Gas production stayed consistent in Cadiz B, at the end of 2016 it was producing at 110,00 mcf. The initial oil production in Cadiz B 4H-14 was about 3000 bbl per month and experienced a steady decline to 66 bbl per month. From the year 2015 to 2016 the annual decline in oil was 91% for well Cadiz B (Figure 4-27). The production trends will be compared to the geochemical and petrophysical data, but the overall complexity of the production behavior is beyond the scope of this study and will not be discussed.

Table 4-13 Well Information

	Well A	Well B	Cadiz B 4H-H	Prudential # 1-A
Status	producing	producing	producing	plugged
Type	gas	gas	oil/gas	oil/gas
Vertical/Horizontal?	Horizontal	Horizontal	Horizontal	Vertical
Formation	Point Pleasant	Point Pleasant	Point Pleasant	Trempealeau
First Production	11/13/2013	11/1/2015	7/1/2014	n/a
Cumulative Produced (mcf and bbl)	Gas	3,586,492	3,564,880	4,683,480	n/a
	Oil	0	0	34,060	
First year production decline (%)	73%	47%	(+) 12%	n/a

94

(A) Well A

(B) Well B

95
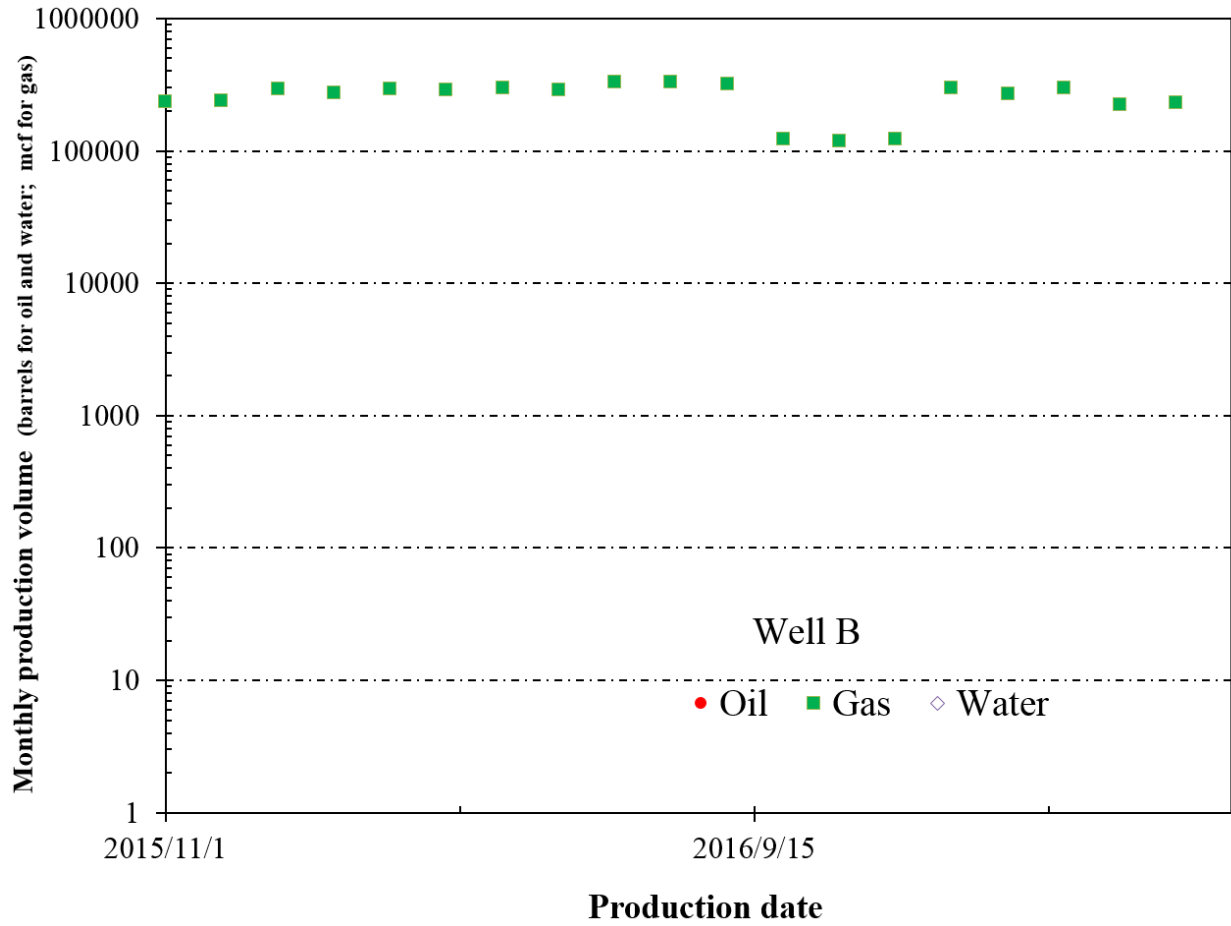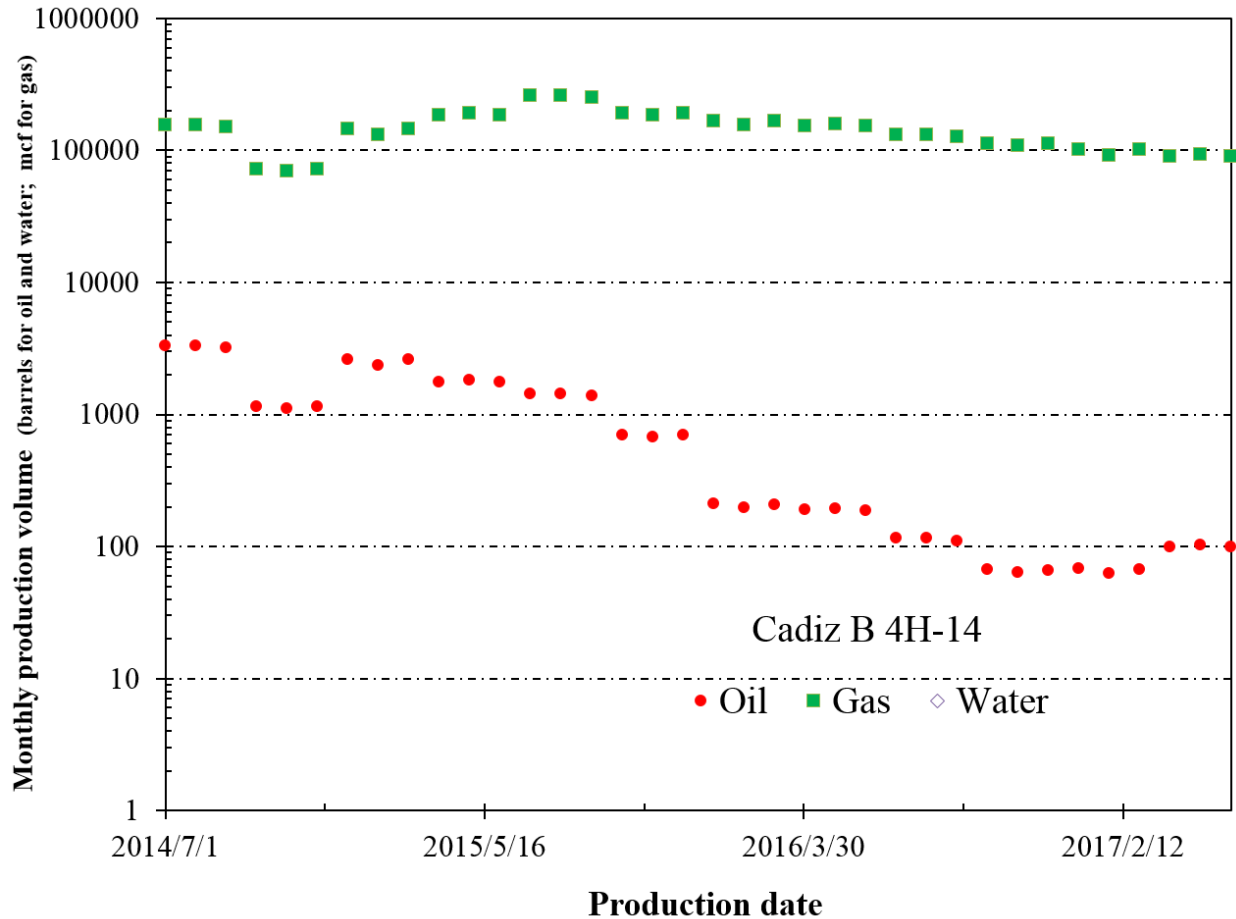
(C) Cadiz 4H-14

Figure 4-27 Monthly production data. (A) Well A (B) Well B (C) Cadiz 4H-14. (Drilling Info, 2017)

Chapter 5: Discussion

5.1 Mineralogy and TOC Trends

Mineralogy is directly related to rock's geomechanical properties, while TOC is a good indicator of hydrocarbons in rocks. Knowing mineralogy and TOC trends within a reservoir could aid in locating future drilling sites. Figure 5-1 plots various minerals versus TOC and depth. Overall, higher TOC values are found in eastern Ohio; the Lexington Limestone Formation has the highest average TOC of 4.5%. TOC has a weak correlation with clay and carbonate contents. As TOC increases, carbonate content increases and clay content decreases, but is not consistent across formations and wells. Regionally,

96

there is a decrease in clay content and increase in carbonate content moving eastward. Vertically,

carbonate content tends to increase with depth within a well, and clay tends to decrease within a well.

There is a strong inverse correlation between carbonate and clay with a correlation coefficient of 0.73.

(A)

(B)
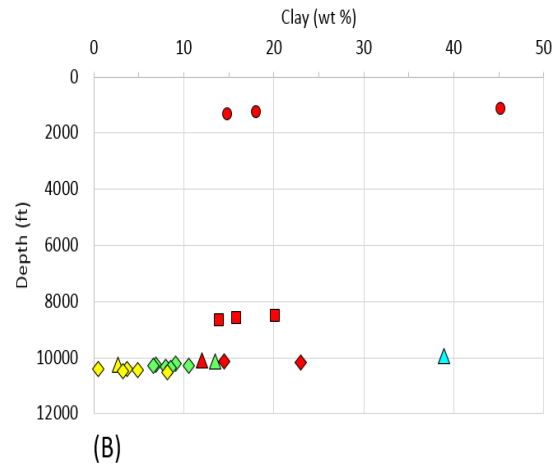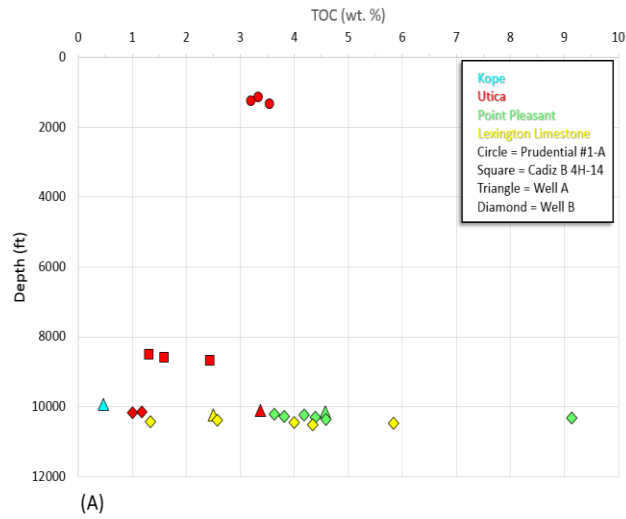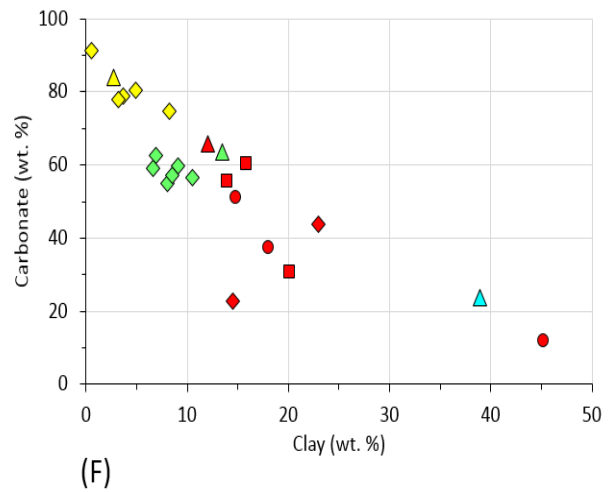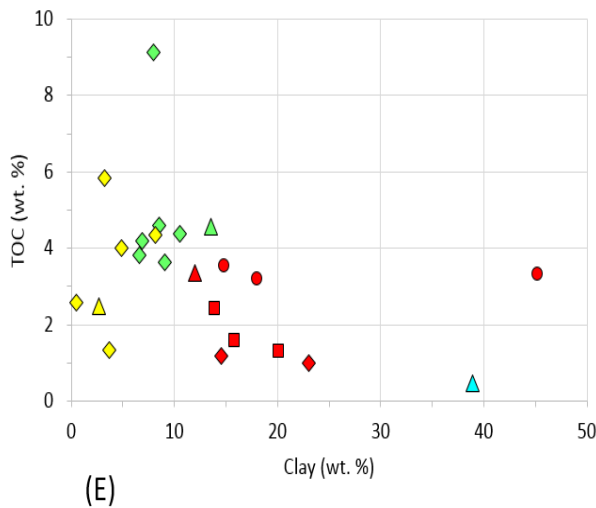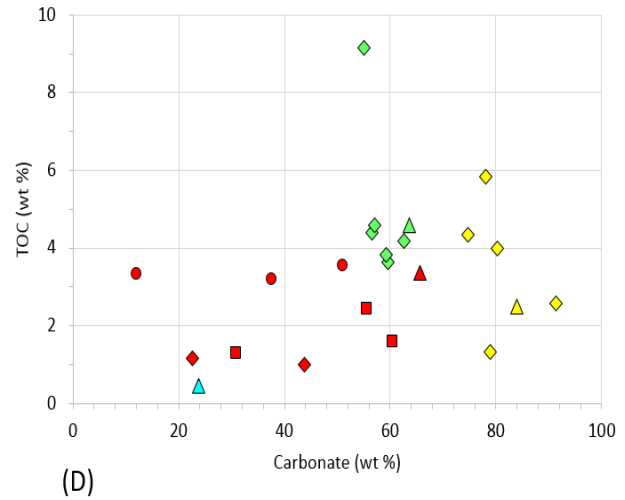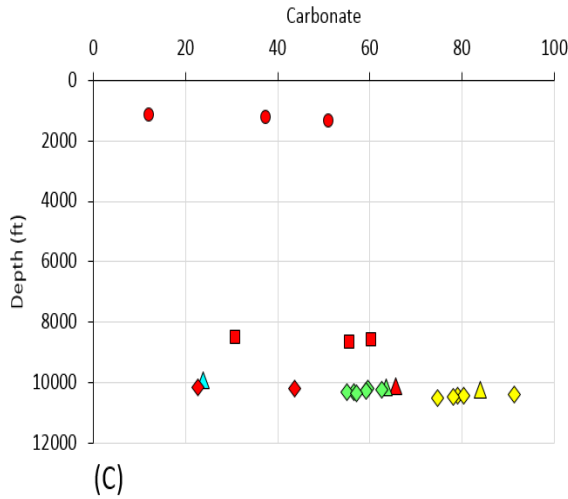
Figure 5-1 (A) TOC vs. Depth; (B) Clay vs. Depth; (C) Carbonate vs. Depth; (D) TOC vs. Carbonate; (E) TOC vs. Clay; (F) Carbonate vs. Clay

5.2 Porosity and Permeability

Porosity is critical for unconventional reservoirs as it controls the storage capacity of hydrocarbons in place. In addition to natural fractures, porosity forms the permeability pathways that enable hydrocarbons to flow from induced fractures to the well bore (Loucks et al., 2012). Porosity measurements vary greatly, ranging from 1.6 to 17.3 % in the Utica Shale, 1.2 to 15.2% in the Point Pleasant, and 1.0 to 12.5 % in the Lexington Limestone, but similar values were obtained between MICP

and helium porosity results for three samples (Table 5-1), indicating the validity of MICP-derived

porosity

Table 5-1 Porosity measurements for samples

Sample ID	Sample Size	MICP porosity	He porosity
P1144-U	1-cm cube	7.6	-
P1235-U	1-cm cube	5.2	-
P1336-U	1-cm cube	-	-
CB8500-U	GRI	17.3	-
CB8600-U	GRI	14.7	-
CB8670-U	GRI	16.6	-
KS9930-K	1-cm cube	1.4	1.5
KS10121-U	1-cm cube	2.5	1.6
KS10150-PP	GRI	8.6	-
KS10230-LL	1-cm cube	1.0	1.1
KB10150-U	GRI +	9.5	-
KB10240-PP	GRI	15.1	-
KB10270-PP	GRI	15.2	-
KB10360-PP	GRI	1.2	-
KB10390-LL	GRI	12.5	-
KB10420-LL	GRI	11.5	-
KB10480-LL	GRI	10.9	-
KB10510-LL	GRI	11.8	-

Permeability values also vary greatly, ranging from 0.3 to 46528 nD in the Utica Shale, 10.6 to

6359 nD in the Point Pleasant, and 0.003 to 545837 in the Lexington Limestone nD (Table 5-2). Between

the different methods to obtain permeability, the approach of n-decane imbibition from sorptivity

consistently produces lower permeability values, and for most samples the geometric permeability

obtained from MICP produces higher permeability values. The variability of permeability values could be

due to sample size (matrix only or also containing laminations). From Figure 3-3, the Kope Formation

contains thin laminae while the Utica Shale and Lexington Limestone contain fossiliferous laminae.

Figure 5-2A shows there is no correlation between porosity and permeability, but when examining

samples with permeability of less than 2000 nD (Figure 5-2B) there is a weak relationship, permeability

increases as porosity increases with a correlation coefficient of 0.36.

Table 5-2 Permeability measurements for different approaches

Sample ID	MICP geometric k (nD)	n-decane Imbibition k (nD)	Helium k (nD)
P1144-U	466	51	-
P1235-U	5894	5.5	-
P1336-U	-	2.6	-
CB8500-U	860	-	-
CB8600-U	569	-	-
CB8670-U	1200	-	-
KS9930-K	15948	75.2	1013
KS10121-U	58.4	0.3	1013
KS10150-PP	63.1	-	-
KS10230-LL	20.5	0.003	2026
KB10150-U	46528	-	-
KB10240-PP	10.6	-	-
KB10270-PP	6359	-	-
KB10360-PP	251	-	-
KB10390-LL	545837	-	-
KB10420-LL	386250	-	-
KB10480-LL	1119	-	-
KB10510-LL	15999	-	-
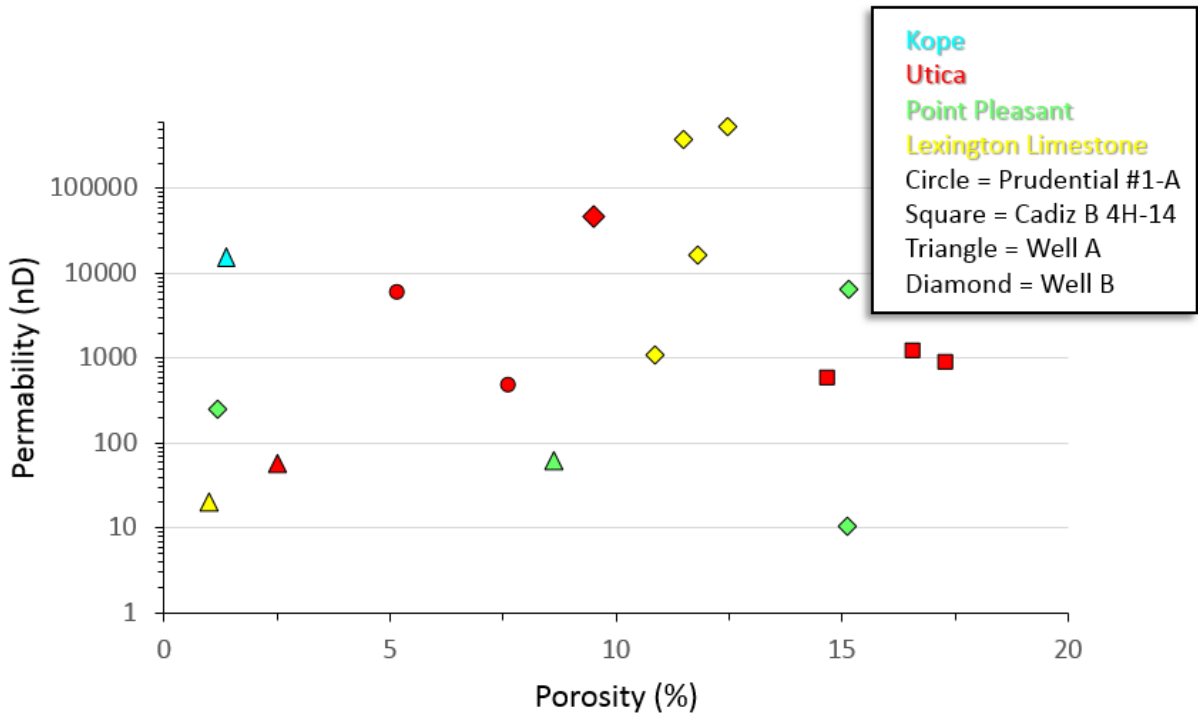
A)
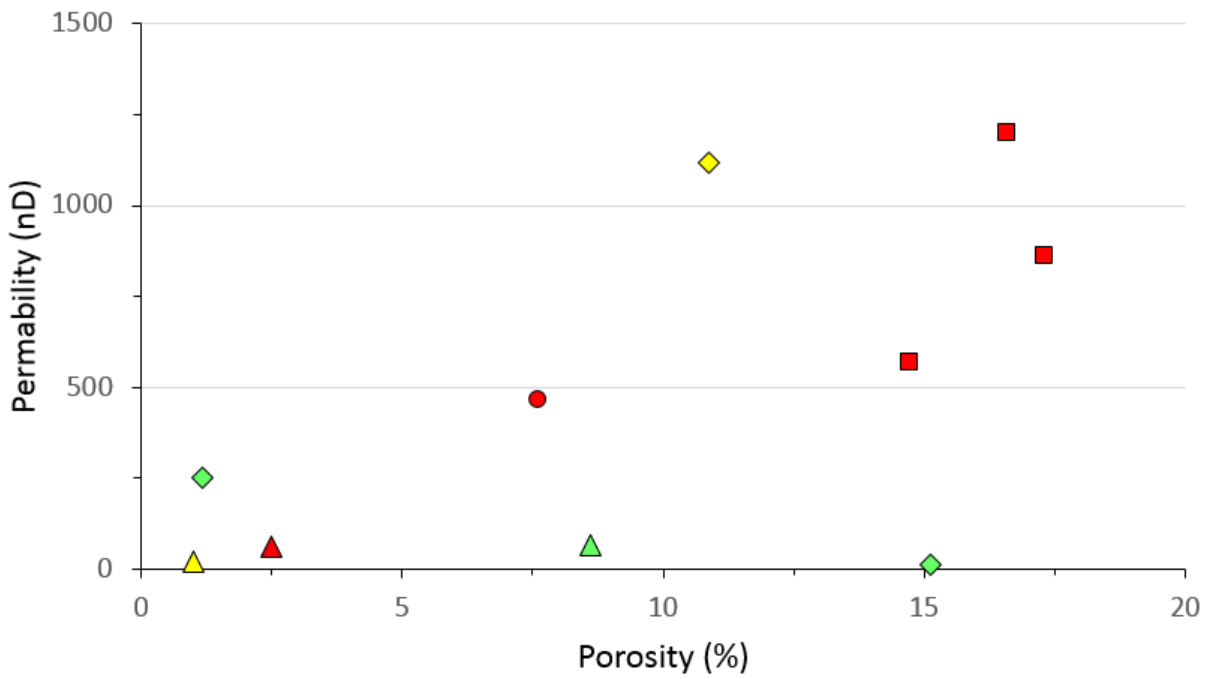
B)

Figure 5-2 Porosity vs. permeability for tested samples from MICP. A) Permeability range 500,000 nD; B) Permeability range 2000 nD

Based on thin section petrography and SEM images, the work of Patchen and Carter (2015) suggested that Utica and Point Pleasant rocks contained little to no mineral porosity and instead the porosity is developed in organic matter (OM). Based on SEM images, helium pycnometry, and XRD the work of Ardakani et al. (2017), demonstrated that organic matter is not the major controlling factor on overall porosity in the Utica Shale while mineralogy has a more significant control. Such different results might be related to tested samples with different maturity. Studies done on more mature gas shales including Barnett Shale (Loucks et al., 2009), Woodford and Horn River Shale (Curtis et al., 2012; Loucks et al., 2009) and the Marcellus Formation (Milliken et al., 2013) have proven that OM-hosted pores are significant component of the pore system. Based on the observations of Loucks et al. (2009), Curtis et al. (2012) and Milliken et al. (2013), we should expect to see a strong correlation between TOC and total porosity.

Overall, there is no correlation between TOC and porosity (Figure 5-3). However, examining each formation closely, the Utica Shale and Point Pleasant Formation display a strong negative correlation between porosity and TOC with a correlation coefficient of 0.88 and 0.69 respectively. As TOC increases, we observe a decrease in porosity in both the Utica and Point Pleasant shales. Possible explanations for this are either that organic matter is largely non-porous for the higher TOC samples or they contain a large amount of migrated bitumen filling up the pore space at this maturity levels. The work of Löhr et al. (2015) indicated that the absence of OM-hosted pores in the mature stage of Ro ~ 1.2 is due to the infilling of pores by generated and retained bitumen, and further maturation will release these filled pores from oil cracking to gas.
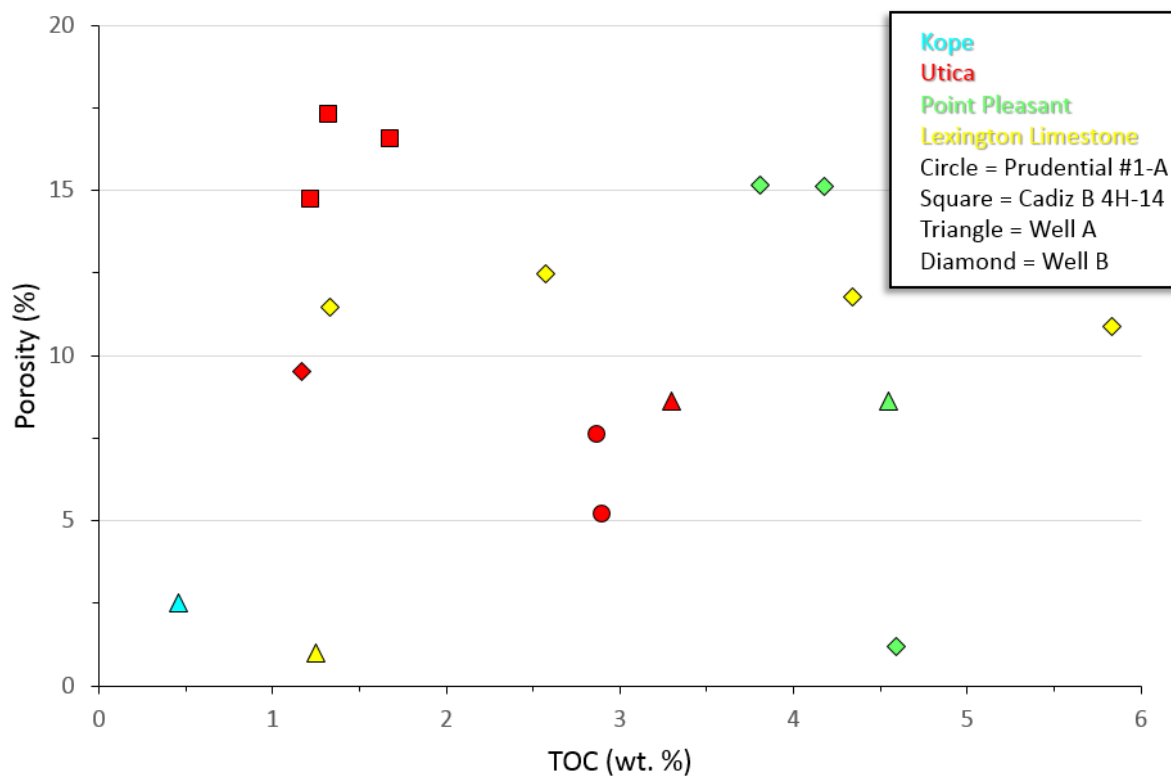
Figure 5-3 Porosity versus TOC from studied samples

To further study the controlling factor on overall porosity, the Utica Shale is examined for OM-porosity development. Figure 5-4 shows the distribution of pore-throat diameters of 5 to 50 nm across different maturities, and the results do not support organic pore creation through maturation. Not all organic matter contains organic-matter pores. Loucks and Reed (2014) observed that mature type III kerogen does not commonly produce OM pores. Utica Shale samples from well Cadiz B 4-H and Well A are both kerogen type III while Prudential #1-A is kerogen type II, and Well B is kerogen type II/III. Even though our results do not show pore creation through maturation, organic matter still has a major influence on porosity, as majority of our samples have at least 30% of porosity accounted for by pore-throat diameters in the range of 5 to 50 nm. Well Prudential #1-A is in the immature zone but in a locally high TOC spot which could contribute to high percentage of 5 to 50 nm pore-throat diameters observed.
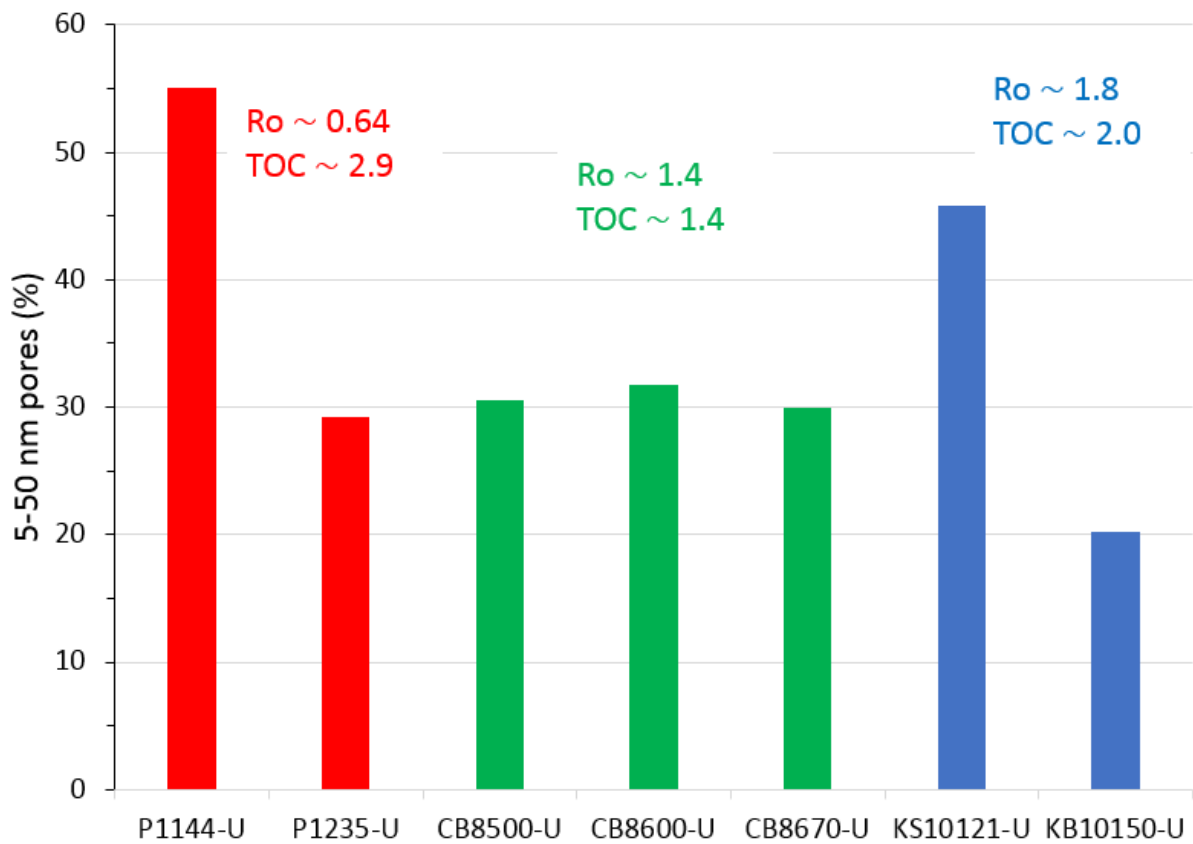
Figure 5-4 Percentage of pores at 5-50 nm throat sizes for Utica Shale samples across different maturity levels

Ardakani et al. (2017) reported that in the Utica Shale, mineralogy has more significant control on overall porosity than organic matter. To further study this observation, mineralogy is compared to porosity in Figure 5-5. For the most part, carbonate follows porosity in a parallel fashion while quartz and clay have no influence on porosity. So, this may suggest that carbonate influences overall porosity although it is not the controlling factor as a high proportion of pores less than 50 nm contribute to overall porosity in the Kope and Utica Shale samples.
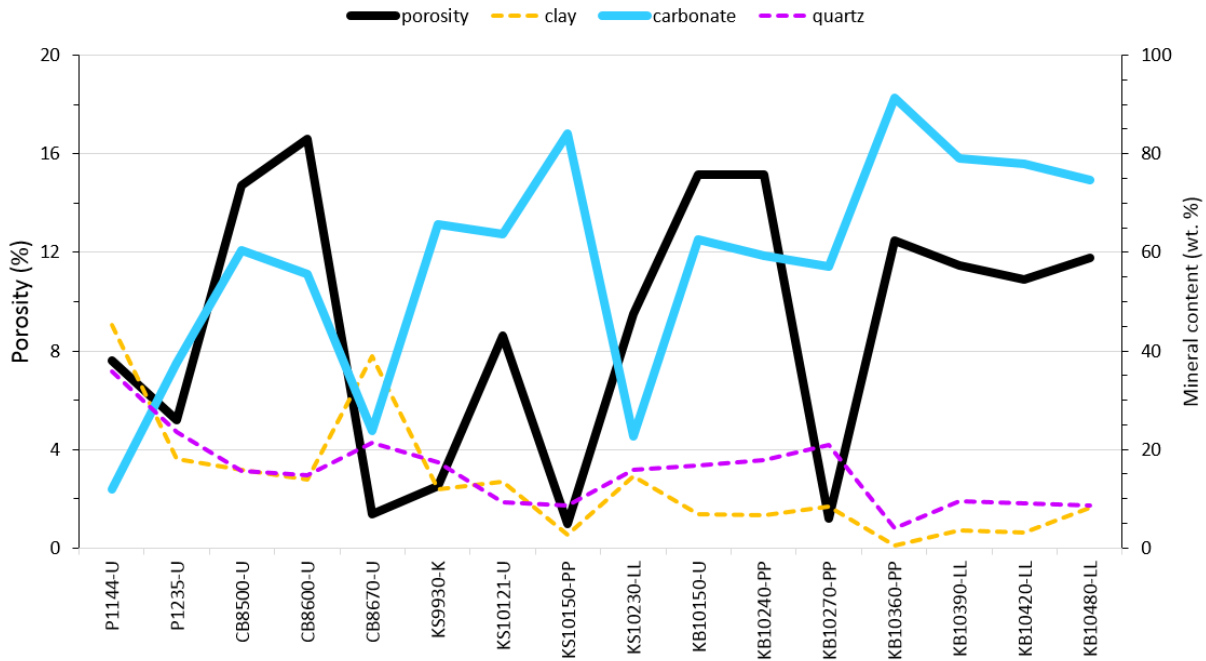
Figure 5-5 Porosity vs. clay, carbonate, and quartz content

5.3 Wetting and Imbibition Characteristics

Both DI water and n-decane can be spontaneously imbibed into the samples. N-decane consistently had a higher Stage II slope. This suggests that the hydrophobic pore network is well-connected; while the hydrophilic pore network is poorly connected containing oil-wet pores (Xu and Dehghanpour 2014).

As samples become deeper, fluid uptake decreases. This observation is consistent with our trends in Figure 5-6, clay decrease with depth (less hydrophilicity) and TOC increase with depth (more hydrophobicity). The greater the water intake the greater of difference of fluid intake there was. For example, P1235-U, the difference of fluid intake was about 85%. As most of our DI water imbibition runs did not observe a Stage III slope and continued to imbibe sample could be due to the fact that muscovite and chlorite can adsorb a significant amount of water (Ghanbari and Dehghanpour, 2015). Also, water

adsorption by muscovite, illite (alteration of muscovite) and mixed illite-smectite, chlorite-smectite, may produce water-induced microfractures, enhancing permeability and porosity.

Figure 5-6 TOC and clay volumes for samples

5.4 Geochemistry

The pore network can be quantified and related to by three major matrix-related pore types: interparticle pores, intraparticle pores, and OM-hosted pores (Loucks et al., 2012) As rocks mature, OM-hosted pores develop as hydrocarbons are expelled from the kerogen, leaving behind pores. The pyrolysis parameter S1 is regarded as representing the abundance of free hydrocarbons (soluble organic

matter) in the source rocks and therefore can be used to indicate the bitumen content in shales (Cao et al., 2015). Figure 5-7 compares S1 to MICP porosity values. These samples are from immature, wet gas, and dry gas region. Apart from the one anomalous point from Well B, there is an apparent correlation; as S1 increases there is an increase in porosity. This observation may imply that kerogen has been converted to porous pyrobitumen or cracking of bitumen has left behind pore space. When examining each formation closer, we again see a strong negative correlation in the Utica Shale, and a weak correlation in the Point Pleasant as we did with porosity and TOC (Figure 5-3), with a correlation coefficient of 0.78 and 0.27, respectively. This negative correlation suggests the breakdown of kerogen into bitumen has a negative impact on the overall porosity in the Utica Shale and Point Pleasant Formations as the bitumen may be occupying pore space.
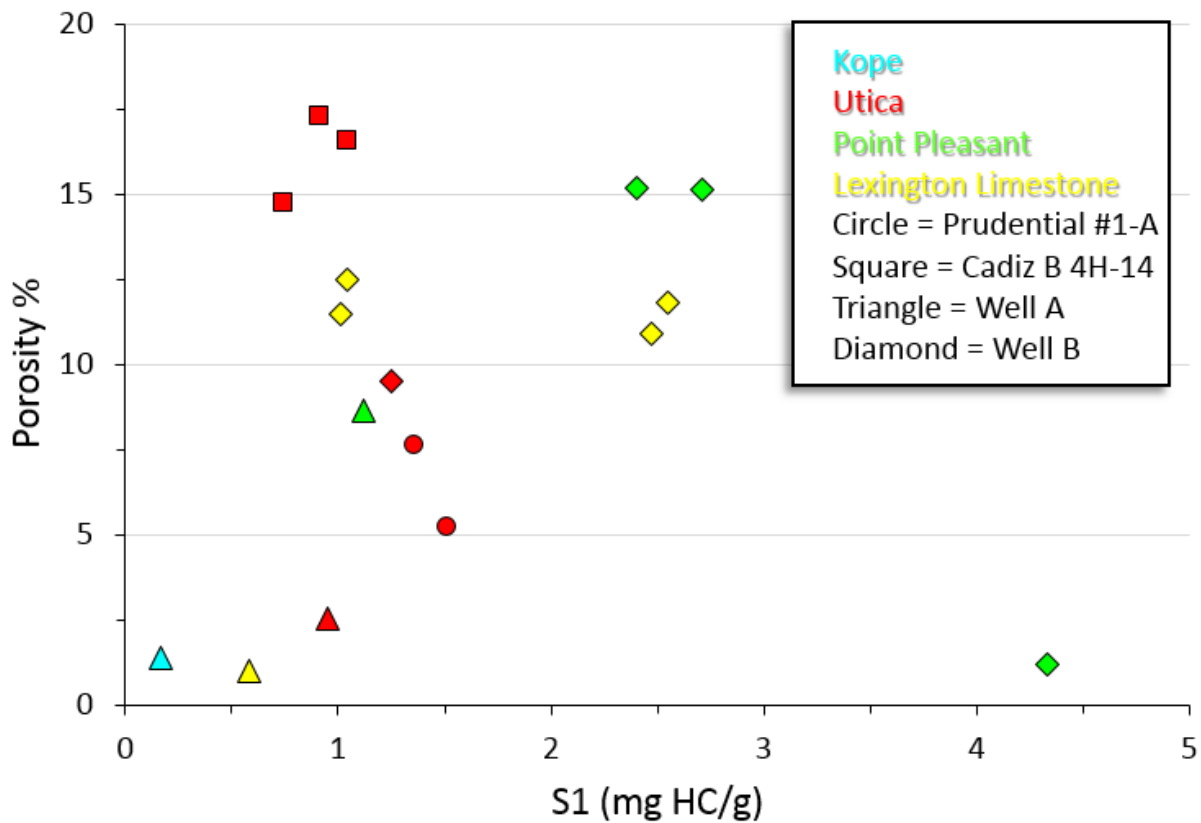
Figure 5-7 Plot of S1 vs. porosity

To further investigate whether maturation controls the pore size distribution, we compare the pore size to S1. Figure 5-8 shows S1 values compared to pore-throat diameters 5 to 50 nm. Figure 5-9 shows S1 values relative to mineral hosted pores with pore throat diameters 0.05 to 1.0 μm. From Figure 5-8 and 5-9 there appears to be two different trends associated with the different mineralogy of formations. The carbonate-rich samples (KB10240-PP, KB10270-PP, KB10360-PP, KB10390-LL, KB10420-LL, KB10480-LL, KB10510-LL), shaded in the yellow box, show S1 values mimicking the volume of pore-throat diameters 5 to 50 nm and 0.05 to 1.0 μm. This supports the idea of pore development through maturation in the Point Pleasant and Lexington Limestone formation. The other trend noticed is associated with the shaly formations, shaded in the grey box, of Prudential #1-A, Cadiz B 4H-14, Kope (KS9930-K), Utica Shale of Well A. Oppose pore-throat diameters ranging from 5 to 50 nm, a decrease of S1 for these formations, exhibits an increase in the volume of mineral hosted pores. This would imply that maturation has less influence on pore development for the Kope Formation and Utica Shale.
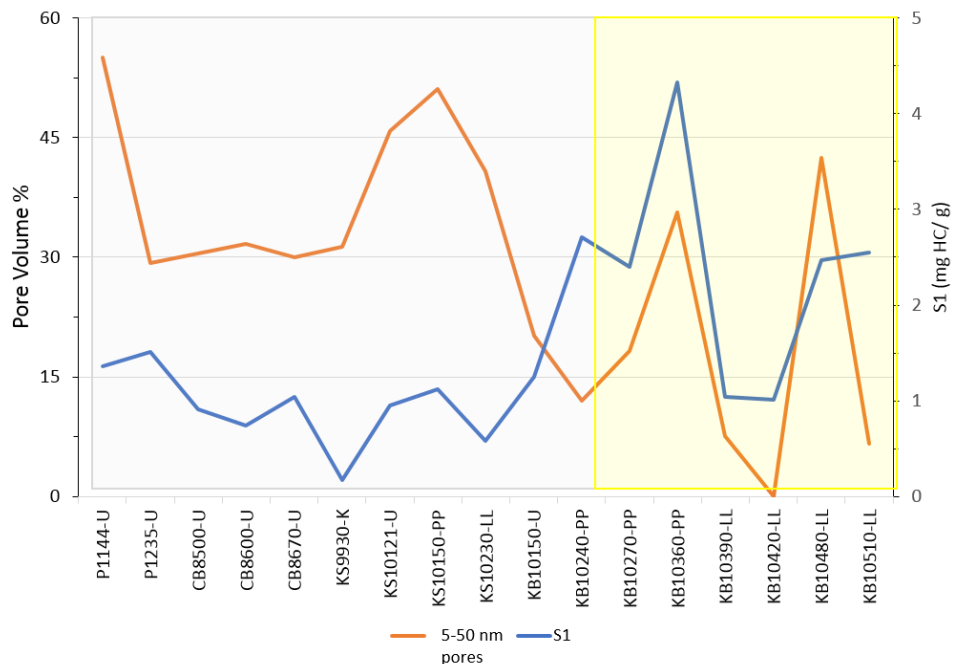
Figure 5-8 Plot of pore volume % of 5 to 50 nm pore-throats relative to S1 values
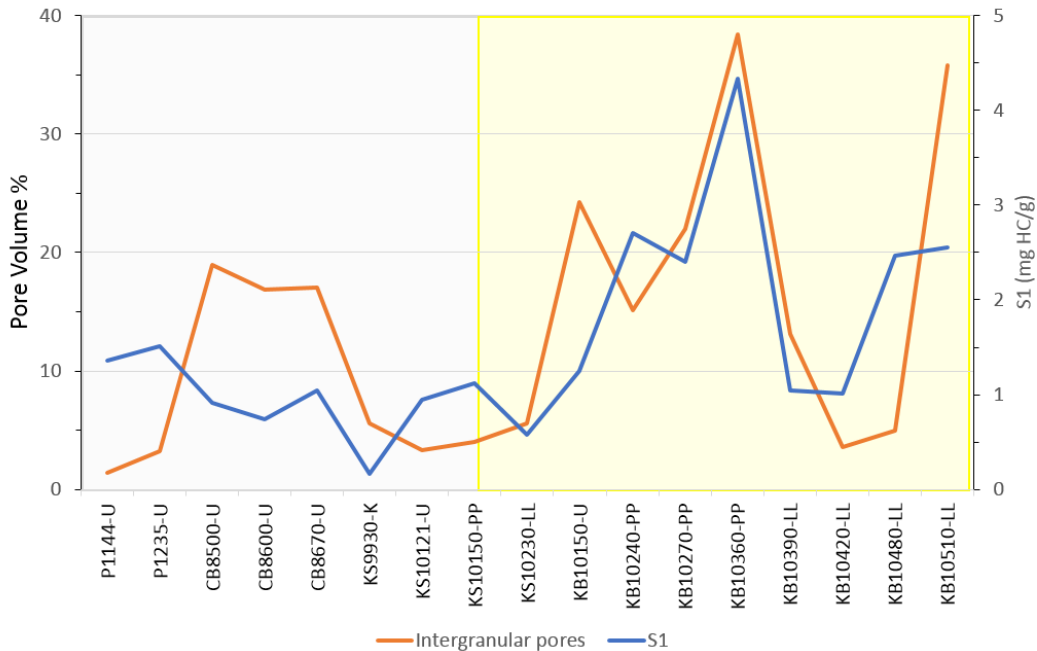
Figure 5-9 Plot of pore volume % of 0.05 to 1.0 µm pore-throats relative to S1 values

Jarvie (2012) proposed the oil saturation index by looking at the crossover effect of, S1 values (oil content) versus the organic richness (TOC). The oil crossover ratio is one to one, and formations above the line are expected to be productive. The idea behind his study is that there is a resistance to oil flow until the oil sorption threshold onto the shale matrix is exceeded (oil cross over or saturation index). The results in Figure 5-10 show that nearly all of our samples are below the saturation index with the slope of one and could be unproductive. As we know from Section 4.9, all the wells except for Prudential #1-A are producing gas and Cadiz B 4H-14 producing both oil and gas. As most of our samples are thermally mature, the cracking of oil to gas could theoretically lower the oil crossover line. It seems that, a saturation index with a slope of 0.5 would collate with the production history of our wells (Figure 5-10).
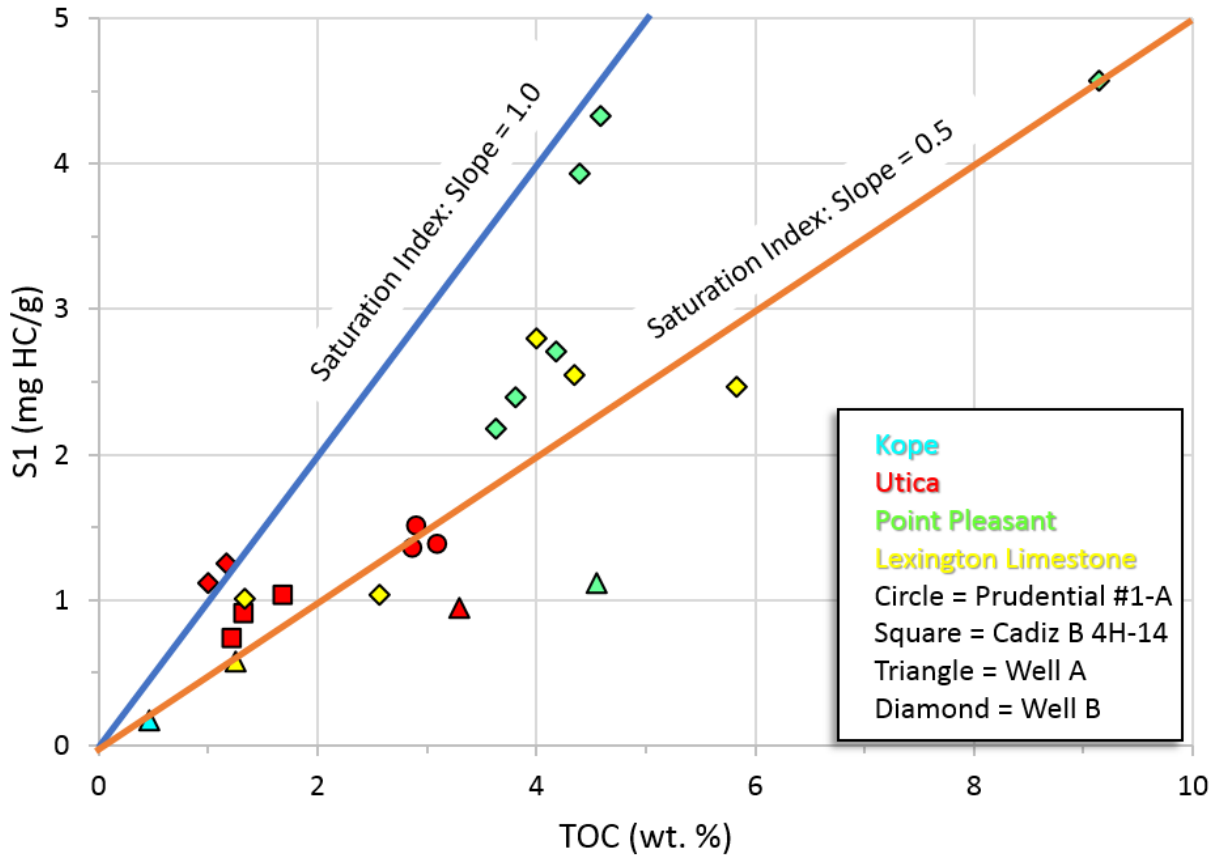
Figure 5-10 Plot of Jarvie (2012) oil crossover line for Utica Play samples

5.5 Reservoir Quality

All successful reservoirs must have the same fundamental characteristics: storage, conductivity and drive. When these basic elements come together in appropriate combination, a rock unit then can be considered a quality reservoir (Ottmann and Bohacs 2014). Fracture development is the key to a successful shale gas reservoir as it enhances the flow of hydrocarbons via the stimulated fractured network and micro-fractures. High brittle mineral content (i.e. quartz and feldspars) can make a reservoir easier to create networked fractures; conversely clay group minerals and organic matter primarily control ductility (Levinthal et al., 2016).

To quantify the brittleness of our samples we used the ternary diagram used by Anderson

(2014) to characterize 15 gas-producing shales with respect to their mineralogy and relevance to

brittleness (Figure 5-11). On this ternary plot, the shaded red area marks the transition zone between

shales that act in a ductile manner, towards the clay axis, and those that act in a predominately brittle

manner, right of the shaded red area. Only two samples, KS9930-K (Kope Formation) and P1144-U (Utica

Shale), fall into the transitional zone suggesting that these samples may act in a more ductile manner if

hydraulically stimulated. Most of our samples fall within the brittle zone indicating that they would be

desirable for hydraulic stimulation, even though the mineralogy of the Utica Shale samples varies

greatly, both laterally and vertically.
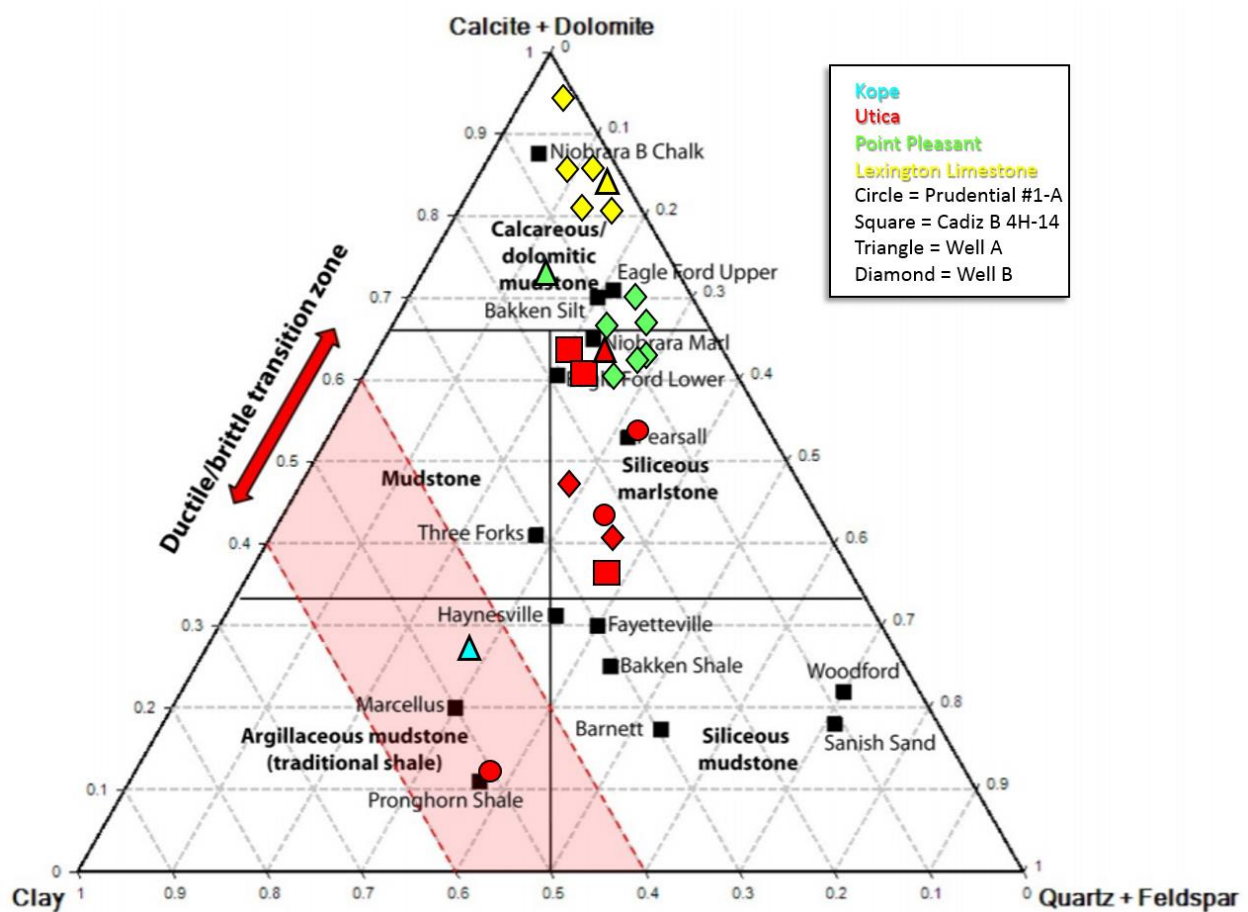
Figure 5-11 Ternary plot of normalized mineral content with ductile/brittle zone (modified from Anderson, 2014)

111

Ottman and Bohacs (2014) quantified the primary properties on a triangle (Figure 5-12) that control the enriched reservoir and conductivity elements important to make a quality reservoir. For their classification scheme, the horizontal axis is the hard component percentage which considers the hard/brittle minerals minus the soft/ductile components of clay %, TOC vol. % and porosity %. According to Passey et al. (2010), TOC volume % can be approximated by doubling TOC wt. %. The vertical axis is the organic component expressed as a volume percentage. Ottman and Bohacs (2014) found that the most successful plays group together with similar properties as "Organically Rich Mudstones". This group, is brittle and enriches in organic material to provide storage and hydrocarbons, but not so much to soften the rock enough to diminish induced reservoir conductivity. Results from this study show the average values from Point Pleasant and Lexington Limestone formations plot within the group of "Organically Rich Mudstones" while the Kope and Utica Shale Formation plots as an "Organically Lean Mudstone". This is consistent with the work of Patchen and Carter (2015) to indicate the Point Pleasant Formation is the target interval in Utica Play.
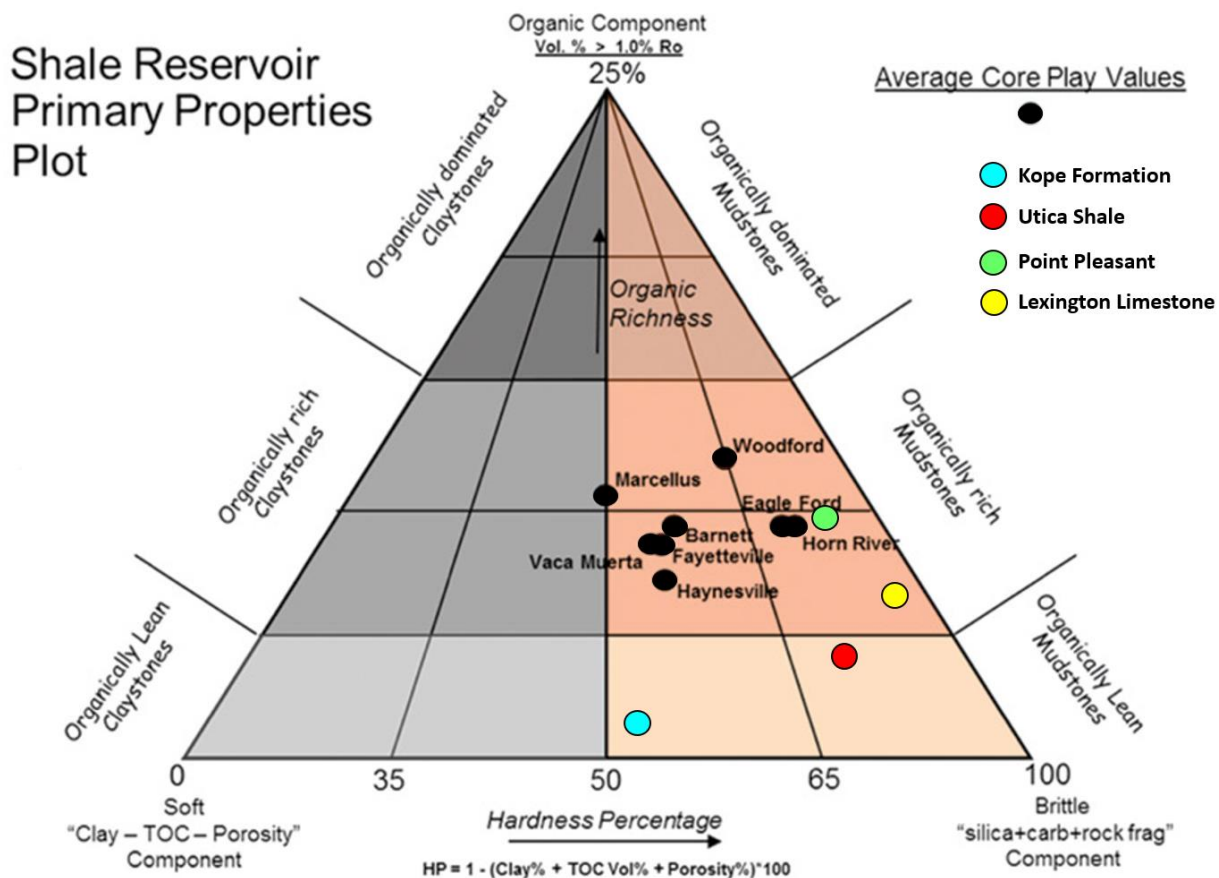
Figure 5-12 Plot of shale reservoir's primary properties (modified from Ottman and Bohacs, 2014)

Our results support the Point Pleasant Formation being the primary target for hydrocarbon production over the Utica Shale. Our XRD results display that the Point Pleasant Formation is one lithofacie (silica-rich carbonate mudstone) whereas the Utica Shale is a range of lithofacies and pore-throat size distributions (Figure 4-5; Figure 4-16). The high carbonate content suggests that fracing could be very effective for all formations of Utica Play. Furthermore, our MICP results display that the Point Pleasant Formation has a larger median pore-throat size and higher porosity to produce hydrocarbons than the Utica Shale, and higher TOC values (Table 5-3). Geochemically, the Point Pleasant shales are better quality source rocks and more generative potential (Figure 4-6; Figure 4-7; Table 5-3).

Table 5-3 Comparison of average petrophysical and geochemical values of Utica and Point Pleasant Formations from the high maturity zone

	Utica	Point Pleasant
TOC (%)	1.62	4.90
S1 (mg HC/g)	1.00	3.03
S2 (mg HC/g)	1.39	2.68
Porosity (%)	6.00	10.0
Median pore-throat diameter (nm)	10.5	27.0
Geometric permeability (nD)	23293	2220
Matrix tortuosity (Do/De)	63154	20823

Well A, Well B and Cadiz B 4H-14, located in eastern Ohio, are horizontal wells producing gas with the Point Pleasant Formation being the primary target (Figure 1-2). Figure 5-12 displays that the Point Pleasant Formation, shares similar reservoir properties to other successful shale plays (i.e., Eagle Ford, Horn River, Woodford). Well A and Well B have produced nearly the same amount of gas up to December 2016 with Well B producing that amount of gas in 13 months (Table 5-4). The different production trends for Well A and Well B could be due to different petrophysical, geochemical and mineralogical characteristics of the Point Pleasant Formation presented in Table 5-4. Our MICP results show that the Point Pleasant Formation in Well B has better storage and flow of hydrocarbons indicated by the high porosity (10.5 %), geometric permeability (3310 nD), median pore-throat diameter (34 nm), and matrix tortuosity (17,018) compared to Well A values of 8.6 %, 63.1 nD, 6 nm, and 32,240, respectively. Geochemically speaking, Well B has greater TOC content (5.0 %) with better source rocks quality (S1 = 3.34 mg HC/g) and greater generative potential (S2 = 3.05 mg HC/g). Mineralogically, the

Point Pleasant Formation is similar in Well A and Well B, with a carbonate content ~ 60 % and clay

content ~ 10 %.

Table 5-4 Comparison of production history and petrophysical, geochemical, and mineralogical
characteristics of Point Pleasant Formation between Well A and Well B

	Well A	Well B
First Production	11/13/2013	11/1/2015
Cumulative Produced (mcf)	3,586,492	3,564,880
First year production	73%	47%
Point Pleasant Characteristics		
Carbonate (wt. %)	63.6	58.4
Clay (wt. %)	13.5	8.27
TOC (%)	4.60	5.00
S1 (mg HC/g)	1.12	3.35
S2 (mg HC/g)	0.44	3.05
Porosity (%)	8.60	10.5
Geometric Permeability (nD)	63.1	3310
Median Pore-Throat Diameter (nm)	6.00	34.0
Matrix Tortuosity (Do/De)	32240	17018

Chapter 6: Conclusions and Recommendations

Chapter 6.1 Conclusions

Samples were chosen from the Utica Play spanning various maturity ranges to study the

petrophysical and geochemical properties. Observations were as follow:

- Mineralogically speaking, the Point Pleasant and Lexington Limestone are dominated by carbonate, while the Utica Shale is very heterogenous both laterally and vertically. Carbonate and clay have an inverse relationship in the Utica Play, as clay increases carbonate decreases.

- Based on TOC wt. % data, the Utica Shale has good to very good source rock potential while the Point Pleasant and Lexington Limestone rank from good to excellent source rock potential

- Pyrolysis data indicate that the majority of Utica Play samples are type II/III and type III kerogen, mostly gas prone

- Based on MICP data, the clay-rich formations have more inter-clay platelet, organic-matter, and intragranular pores with 2.8 to 50 nm pore-throat sizes, as the more carbonate-rich experience more prevalent amount of intragranular and intergranular pores of $\sim$ 100 nm in throat sizes.

- 5 to 50 nm pore-throat diameters play an important role in contributing over 30% of porosity in most samples, and haves a positive correlation with S1. Bitumen may be filling the pores of the Utica Shale and Point Pleasant Formations at maturation level of $\sim$ 1.2 R_o %. Carbonate affects overall porosity but is not a controlling factor.

- Imbibition results indicate high pore connectivity for hydrophobic fluid (n-decane) and low for hydrophilic fluid (DI water).

- For the same samples, there is a high variability of permeability values, which could be due to sample size (matrix only or also containing lamination), technique, and interpretation method.

- Based on the ternary plot of Ottmans and Bohacs (2014) for shale reservoirs, the Point Pleasant and Lexington Limestone share similar traits, such as hardness and organic richness, as other successful shale plays in the U.S. In addition, these formations have larger median pore-throat sizes, than Utica and Kope, for oil molecules to move. Furthermore, the ternary plot of Andersons (2014) shows nearly all of our samples fall in the brittle zone which is desirable for hydraulic fracturing.

- Petrophysically, geochemically, and mineralogically speaking, our results support the Point Pleasant Formation being the primary target of the Utica Play. The higher and better sustain production rates of Well B compared to Well A could be due to the more favorable petrophysical and geochemical characteristics of the Point Pleasant Formation.

Chapter 6.2 Recommendations

In order to gain more insight on the Utica Play more sampling of each formation needs to be done with the same exact study (e.g., sample size). Further experiments such as field emission-scanning electron microscopy (FE-SEM) can image the pores > ~ 5nm for pore types, for different maturity samples both before and after solvent cleaning to remove migrate bitumen, and scanning transmission x-ray microscopy analysis (STXM) can differentiate between the different types of organic matter. This will help evaluate the nature and complexity of pore structure.

Appendix A

Standard Operating Procedures at Shimadzu Center for Environmental, Forensics and Material Science

Laboratory for XRD analysis

Standard Operating Procedure
MaximaX XRD-7000: Shimadzu X-ray Diffractometer

Sample Preparation

- Prepare your sample by compacting the sample into the sample holder using a glass slide
- Avoid vertical loading by removing excess sample with the edge of the glass slide
- Attempt to make your sample as flat and homogenous as possible; once this is completed your sample is ready to be analyzed.

Power Operations: *IF THE CHILLER & XRD ARE ALREADY ON CONTINUE TO STEP THREE*

- Turn the chiller on by pressing the power button (on the face of the chiller), a green light will illuminate.
    - Allow the chiller to sit for ~20 mintutes to adjust to the proper temperature.
- Turn the XRD on by pressing the power button on the left hand side. The green power button will illuminate on the front panel of the XRD.

XRD Calibration:

- Locate and open the [PCXRD] program on the desktop. The main "XRD-6100/7000" panel will display.
- Click the [Display and Setup] icon, a "door alarm check" window will pop up. Follow the prompt to open and close the XRD door, once complete click "Close". A "IOcon" window will pop up with the message "Now Calibration! If ready OK", Click "OK".
- The XRD is officially calibrated and ready to process your sample.

Setting Anaylisis Conditions:

To set the processing conditions go to the "XRD 6100/7000" panel.

- Click on the [Right Gonio Conditon] icon to open the [Anaylisis Conditon Edit Program] window
- Click the blue bar under [Measurement Mode: Standard] to open the [Standard Condition Edit] window.
- Most of the settings in the [Standard Condition Edit] window will be preset. Only a few conditions will need to be changed.
- The following general condition settings will work for a wide array of materials.
    It's very important to follow these next steps, double check any settings you change ensuring to follow these guidelines prescisely. This will minimize minor mistakes when processing materials and will prevent damage to the detector.
    - <u>Scanning condition:</u> Scan Range (deg) = 2°-70°
    - <u>Optional Condition:</u> Check the box [Option Enable]
    - <u>Beta Attatchment:</u> Control Mode: *Rotation*
                        Rotation Speed (rpm): *6*
    - <u>Slit Conditon:</u> Slit Condtions are preset, and must be verified on the XRD to ensure the proper slit sizes match the settings listed under the Slit Conditions.
        - Checking the Slits:
            - Open the XRD door, on the left side of the XRD is the X-ray tube, the Divergence Slit is attached to the left side of the divergence soller slits.
            - On the right hand side will be the detector arm which contains a set of Scattering soller slits, the Scattering Slit faces the sample (Left) and the Receiving Slit faces the detector (Right).
            - If they are not the same sizes as what is preset in the [Slit Condition] box change the slit's so they do match.
        - *Standard Slit Settings:*
            - <u>Divergence Slit:</u> 1.0°
            - <u>Scattering Slit:</u> 1.0°
            - <u>Recieveing Slit:</u> 0.3 mm
- Double check your settings and make sure they are correct, if they are click [OK].
- A [File & Sample Condition Edit] window will display; change the [Group name] to match your destination folder name and change [File name] and [Sample Name] to match your sample name, click [New].
    - Later samples can be created by simply changing the file and sample names and clicking [Modify].
- Click [Close] on the [Standard Conditon Edit] window.

Starting the XRD processing:

- Locate and click the [Right Giono Analysis] icon on the [XRD-6100/7000] panel.

- Your current sample name should appear highlighted blue in the upper portion of the [Right Gonio System: AnyisisCondition Edit Program] window. Highlight your sample and click [Append], this adds your sample to the list in the bottom portion of the window labeled [Entry for Analysis], click [Start].
- Your sample should appear in the bottom of the [Right Giono Analysis & Spooler Program] window, click [Start] in this window. This officially starts the analysis process.
  - Indicators for Analysis: A clicking sound will come from the XRD when the locking mechanism on sliding door locks. On the face of the XRD a yellow light should illuminate under [X-RAYS ON].
- Leave all software windows open and allow the XRD to process your sample, this should take ~30 minutes.

Completed XRD Processing:
- A complete peak spectrum should appear in the [Right Giono Analysis & Spooler Program] window upon completion.
- The green [Anaylzing!] Box should disappear and the yellow [X-RAYS ON] light should turn off.
- If you have more samples to analyze, continue to run your samples in the same manner listed above.

Opening Peak Profile Spectrum:
- Locate and open the icon for the [MDI jade 9] software on the Desktop.
- Under [file], click [Read], locate the folder [xddat] under [favorites]. Locate the folder where your samples are saved.
- In your folder, each sample should have a [.RAW] file, use this file to open your selected spectrum in the [Jade 9] software.

Identifying Minerals in Peak Spectrum:
It's important to have an educated background on the sample you're analyzing. Knowledge regarding the bulk composition and what you're searching for will greatly reduce the amount of time spent IDing the various peaks in the spectrum.

- Locate the [Find Peaks] icon on the main tool bar next to the [Floppy Disk/Save] icon, this will identify and mark any statistically significant peaks within the spectrum
- Choose a mineral database: At the top of the panel to the right of the spectrum window, there will be a drop down menu choose the [RDB-Minerals] as the database. The RDB-Mineral database should be predominately used to identify most minerals in your spectra.
  - *If you cannot find a mineral in the RDB-Minerals database change to the [PDF+4 Minerals] database library, but be sure to change back to the RDB database once the mineral is located.*
- Begin searching for minerals based on your pre-existing knowledge regarding the sample. When you identify minerals that fit your peak spectrum hit [Enter] on the keyboard, this process will add the minerals to a compiled list of those minerals which you identified in the spectrum.
- Once you have exhausted your initial hypothetical list of minerals, a helpful tool to use is the [Line Based Search/Match]. Go to the main tool bar and lcoate [Identify] and select the [Line Based Search] option.
  - *This tool will compile a list of minerals by searching a selected PDF database for entries with peaks which are statistical matches for the peaks identified within your spectrum.*
  - Settings:
    - [Two-Theta Error Window] max setting should be no more than 0.24%
    - [Top Hits to List] max setting 80
  - Set the parameters and click the blue [Play] icon next to the [X] to run the search and generate a list of possible phases that might fit your spectra.
    Note: the line based search should not be used as a primary way to identify the bulk mineral mode of the sample as the software is not consistent when generating phases and will possibly leave out important phases for the spectrum.

- Once all minerals have been ID'd, check that they have been added to the mineral list by pushing [Enter] on the keyboard.
- Click the [%] icon next to the drop-down mineral list located on the toolbar in the middle of the window to begin modal analysis.
  - An overlay will appear with different chart configurations of the modal results, to change the configurations of the chart use the drop down menu in the chart window.

Analysis Check with Pattern Deconvolution:

- A key indication that the peak spectrum has been fully fitted and identified is by using the [Pattern Deconvolution] tool which automatically runs with the modal analysis.
    - The pattern deconvolution tool will generate a red overlay spectrum on top of the original white spectrum.
    - This process is generating a [Best Fit Profile] composed of the selected mineral standards from the [Mineral PDF database library] with your sample spectrum.
    - If all minerals have been properly identified, then the red deconvolution overlay will match the peak spectra for each peak. If there are peaks that don't have the red deconvolution overlay then those peaks have not been identified.
- Continue processing your spectrum until your original spectra and the deconvolution spectra match.

Saving Data:

To save your data,

- Go to [file] and [Save], save yout data under [Current work as *.SAV]. This will save all analyisis as a separate file.

Appendix B

Standard Operating Procedures at Shimadzu Center for Environmental, Forensics and Material Science

Laboratory for TOC analysis

The SSM-5000A is a solid sample module which can run two types of analysis, Total Carbon (TC) and Inorganic Carbon (IC), both of which are analyzed by a nondispersive infrared detector (NDIR). By subtracting the IC values from TC values, the Total Organic Carbon (TOC) of a sample can be quantified.

Methods

The TC method

- Uses the electric furnace to heat the combustion tube to 900°C, this allows the carbon combustion oxidation reaction to occur and will yield carbon dioxide which will be analyzed through the NDIR.

The IC method

- Uses the electric furnace to heat the combustion tube to 300°C, and, by adding 0.4 mL of 33% Phosphoric Acid (H$_3$PO$_4$), for the carbonate acidification reaction to occur, will yield carbon dioxide which will be analyzed through the NDIR.

Sample Table

a. Open [TOC-V Sample Table Editor] icon and enter your initials

b. Click the [New] icon in the [Sample Table] window

c. Select [SSM-5000A] for the H/W System Settings

d. Select icon labeled [Connect] located on the top row of the window

e. Right click on the number 1 in the Sample Table window and select the [Insert Sample] tab

f. Select [Calibration curve] parameter and search in the Thawspace (T:) Drive for the folder labeled [SSM-5000A_CalCurve].

g. Depending on which type of analysis will be run you will choose the file "TC_CalCurve_SSM5000-A" for Total Carbon or the "IC_CalCurve_SSM5000-A" for Inorganic Carbon.

h. Select [Next], then specify your [Default Sample Name] (e.g., Bob_Shales) and specify your [Default Sample ID] (e.g., LS_1200)

i. Select [Next], then assure the units are in mg/L and leave the [Expected Conc. Range] as is, this number is negligible.

j. Select [Next] and assure your integration time is maxed out at 20:00 min, then select [Finish].

Sample Boat

There are two distinct Tupperware boxes with sample boats depending on which method is used.

a. When using the TC method, use the box labeled "Heat Treated Sample Boats".

b. When using the IC method, use the box labeled "Acid Treated Sample Boats".

    i. Use tweezers to grab a clean sample boat from its respective box and place it on the scale.

    ii. Once the scale has balanced out and a right directional arrow appears on the screen, press the [O/T] button to tare the scale.

    iii. Carefully use the scoopula to scoop a small amount of your sample into the boat. (ideal weight 30-70 mg)

    iv. Once the scale has balanced out, record the weight in mg. This value is used to calculate the concentration of carbon.

Collecting TC

a. Return to the [Sample Table] and click on row number 1 where you inserted your first sample and make sure it is highlighted.

b. Select the [Start] icon located to the left on the second row of the [Sample Table Editor] window.

c. To run your first sample you will be required to name your Sample Table in the Thawspace (T:) Drive (e.g., Bob_Shales_2017_05_01).

d. Next, you will be prompted to enter the weight (mg) of your sample obtained from the balance. **DO NOT PRESS START**.

e. Carefully open the TC chamber by turning the blue knob counter clockwise and slide the cover over to the right.

f. Place the boat on the metal sample boat holder, make sure it is aligned so that it fits securely in the boat holder.

g. Slid the cover back over the chamber and make sure it is tightened by rotating the blue knob in the clockwise direction.

h. Return to the Enter Sample Amount screen and once the weight is input select [Start].

i. If all background conditions are met, a green [Ready] icon will appear on the top right window and you will be prompted to [Push the sample boat into the measurement position] which you do by pushing the front blue knob all the way forward.

j. To view your measurements, click the second blue icon in your sample window, it has an icon of a graph and a syringe.

k. Once your measurement is complete, you will be prompted to pull the boat back to the cooling position, this is the position located between the [sample change] and [measuring] position on the top panel of the instrument.

l. nce the boat has cooled sufficiently, you will be prompted to pull the boat back to the preparation position.

m. Once the sample boat has reached the [sample change] position, a table with your Total Carbon Concentration will appear.

n. Open the chamber cover by rotating the blue knob counter clockwise and sliding it over to the right.

o. ***CAUTION*** sample boat will still be extremely hot, use the tweezers and carefully pick up the boat and place it on the hot plate.

p. To run another sample for TC analysis, repeat the previous steps as necessary.

Collecting IC

a. Return to the [Sample Table] and click on row number 1 where you inserted your first sample and make sure it is highlighted.

b. Select the [Start] icon located to the left on the second row of the [Sample Table Editor] window.

c. To run your first sample you will be required to name your Sample Table in the Thawspace (T:) Drive (e.g., Bob_Shales_2017_05_01).

d. Next, you will be prompted to enter the weight (mg) of your sample obtained from the balance. **DO NOT PRESS START**.

e. Carefully open the IC chamber by turning the green knob counter clockwise and slide the cover over to the right.

f. Place the boat on the metal sample boat holder, make sure it is aligned so that it fits securely in the boat holder.

g. Slid the cover back over the chamber and make sure it is tightened by rotating the green knob in the clockwise direction.

h. Return to the Enter Sample Amount screen and once the weight is input select [Start].

i. If all background conditions are met, a green [Ready] icon will appear on the top right window. Although you will be prompted to [Push the sample boat into the measurement position], ***WAIT*** First, pull up on the white plastic nozzle attached to the bottle of phosphoric acid and allow it to fully inject 0.4 mL of acid into the sample boat so IC reaction can occur.

j. Once the acid has fully injected into the sample boat, push the front green knob all the way forward to the measuring position.

k. To view your measurements, click the second blue icon in your sample window, it has an icon of a graph and a syringe.

l. Once your measurement is complete, you will be prompted to pull the boat back to the cooling position, this is the position located between the [sample change] and [measuring] position on the top panel of the instrument.

m. Once the boat has cooled sufficiently, you will be prompted to pull the boat back to the preparation position.

n. Once the sample boat has reached the [sample change] position, a table with your Inorganic Carbon Concentration will appear.

o. Open the chamber cover by rotating the green knob counter clockwise and sliding it over to the right.

p. ***CAUTION*** sample boat will still be extremely hot and may have residual phosphoric acid, use the tweezers and carefully pick up the boat and place it in the beaker with yellow tape labeled Dilute Phosphoric Acid.

q. To run another sample for IC analysis, repeat the previous steps as necessary.

Saving Results

a. Once all TC and IC sample analysis has been completed you can compile a comprehensive report of all your data to save.

b. Select the [File] tab in the top menu bar, scroll down and select [Print] and scroll to the right and select [Sample Report-All]

c. Ensure that the printer is set to [Microsoft XPS Document Writer] and click [OK]

d. Save your file to the Thawspace (T:) Drive so that you can email yourself the results for use the UTA Box sync cloud service.

e. Once all analyses are saved it would behoove you to open up an MS Excel spreadsheet and create a table of all of your sample with TC in one column and IC in another to easily subtract them to get the sample TOC values. **Remember: TOC = TC - IC**

Appendix C

Laboratory procedure for pyrolysis by Weatherford Laboratories

Description of Selected Experimental Methods

Rock Sample Preparation

Samples for Total Organic Carbon (TOC) and/or Programmed Pyrolysis may each require varying levels of sample preparation. Groups of samples are evaluated as to their respective condition as received and are handled differently depending on the various types of contaminants, lithologies, and analytical objectives. Samples are not high-graded prior to grinding unless specifically instructed by the client. When necessary and as instructed, water washing may be required to remove water-based mud. Solvent washing can be utilized to remove oil-based and/or synthetic-based mud. Additional solvent extraction of the crushed rock will be necessary to completely remove the contaminating oil-based and/or synthetic-based mud. Sample picking may also be necessary to remove lost circulation material or known cavings. Samples for TOC and Programed Pyrolysis are then ground to pass through a fine mesh sieve prior to analysis.

Total Organic Carbon

Approximately 0.10 g of crushed rock is accurately weighed and then digested with concentrated hydrochloric acid to remove all carbonates form the sample. At this point, gravimetric carbonate content can be determined if requested. Following digestion, the sample is washed through a filtering apparatus, placed in a combustion crucible and dried. After drying, the sample is analyzed with a LECO Carbon Analyzer with detection limits to 0.01 weight percent. Standards and sample duplicates are tested regularly to assure superior instrument performance.

Programmed Pyrolysis (Rock-Eval II, Rock-Eval VI, Source Rock Analyzer)

Programmed pyrolysis (Rock-Eval and SRA) is performed to assess source rock quality and thermal maturity (e.g., Peters, 1986; Peters and Casa, 1994). In programmed pyrolysis, crushed rock samples are heated in an inert environment to determine the yield of hydrocarbons and CO_2. The sample is initially held isothermally at 300°C for 3 minutes, producing the S1 peak by vaporizing the free (unbound) hydrocarbons. High S1 values indicate either large amounts of kerogen-derived bitumen (as in an active source rock) or the presence of migrated hydrocarbons. The oven then increases in temperature by 25°C/minute to a final temperature of approximately 600°C, depending on the instrument type. During this time, hydrocarbons that evolve from the sample as a function of the pyrolytic degradation of the kerogen are measured, generating the S2 peak and is proportional to the amount of hydrogen-rich kerogen in the rock. The temperature at which the S2 peak reaches a maximum, "T_{max}", is a measure of the source rock maturity.

Accuracy of T_{max} is 1-3°C, depending on the instrument, program rate and sample size, but can also vary by organic matter type. Tmax values for samples with S2 peaks less than 0.2 mg HC/g rock are often inaccurate and should be rejected unless a definitive kerogen peak is noted from the pyrogram. Any carbon dioxide released between 300° and 390°C is also measured, generating the S3 peak, providing an assessment of the oxygen content of the rock. In addition to the standard programmed pyrolysis method, we have several additional methods available designed to provide the client with additional useful information as it relates to the geochemical nature and potential of a rock sample including but not limited to TOC quantification, Carbonate quantification, Reservoir Oil Quality, APIR and Kerogen Kinetic analyses. A summary of analytical results from Programmed Pyrolysis follows.

Results

S1:	free oil content (mg hydrocarbons per gram of rock)
S2:	remaining hydrocarbon potential (mg hydrocarbons per gram of rock)
S3:	organic carbon dioxide (mg CO_2 per gram of rock)
TOC:	total organic carbon content (wt. %)
Tmax:	temperature at maximum evolution of S2 hydrocarbons
Ratios:	hydrogen index (HI), oxygen index (OI), production index (PI), S2/S3, and S1/TOC

References

Anderson, T. 2014. Key parameters for liquid-rich unconventional plays: Case studies from North

America. In Proceedings, Geoscience Technology Workshop, Hydrocarbon Charge

Considerations in Liquid-Rich Unconventional Petroleum Systems, November 2013, Vancouver,

BC, Canada, p. 1-33.

Ardakani, O. H., Sanei, H., Ghanizadeh, A., Lavoie, D., Chen, Z., Clarkson, C. R. 2017. Porosity variations in

the Upper Ordovician Utica Shale, southern Quebec, Canada. Geoconvention May 15-19, 2017

Calgary, Canada.

American Petroleum Institute Recommended Practice (API RP) 40. 1998. Recommended Practice for

Core Analysis (2nd Ed.). Am. Petrol. Inst., Washington, DC.

Bai, B., Sun, Y., and Liu, L. 2016 Petrophysical properties characterization of Ordovician Utica gas shale in

Quebec, Canada. *Petroleum Exploration and Development,* 43(1): 74-81.

Barrett, E.P., Joyner, L.G., and Halenda, P.P. 1951. The determination of pore volume and area

distributions in porous substances. I. Computations from nitrogen isotherms. Journal of the

American Chemical Society, 73: 373-380.

Brett, C. E., and Algeo, T. 1999. Stratigraphy of the Upper Ordovician Kope Formation in its type area

(northern Kentucky), including a revised nomenclature: *in*ALGEO, T.J., and BRETT, C.E., eds.,

Sequence, cycle and event stratigraphy of Upper Ordovician and Silurian strata of the Cincinnati

Arch region: 1999 Field conference of the Great Lakes Section of SEPM, Cincinnati, p. 47–64.

Brunauer, S., Deming, L.S., Deming, W. E., and Teller, E. 1940. On a theory of the van der Waals

adsorption of gases. Journal of the American Chemical Society, 62: 1723-1732.

Cai, J., Hu, X., Standnes, D. C., and You, L. 2012. An analytical model for spontaneous imbibition in fractal

porous media including gravity. *Colloids and Surfaces A: Physicochemical and Engineering*

Aspects, 414: 228-233. doi:10.1016/j.colsurfa.2012.08.047

Cao, T., Song, Z., Wang, S., Cao, X., Li, Y., and Xia, J. 2015. Characterizing the pore structure in the

Silurian and Permian shales of the Sichuan Basin, China. Marine and Petroleum Geology, 61:

140-150.

Chukwuma, F. 2015. Nanopetrophysics of the Utica Shale, Appalachian Basin, Ohio, USA. M.S. Thesis,

Department of Science, University of Texas at Arlington, USA.

Coretest Systems. 2012. AP-608 Operator's manual, 7:d.

Curtis, M.E. Cardott, B.J., Sondergeld, C.H., and Rai, C.S., 2012. Development of organic porosity in the

Woodford Shale with increasing thermal maturity. International Journal of Coal Geology, 103:

26-31.

Dollimore, D., and Heal, G.R. 1964. An improved method for the calculations of pore-size distributions

from adsorption data. Journal of Chemical Technology and Biotechnology, 14: 109-144.

Dow, WG. 1977. Kerogen studies and geologiscal interpretations. Journal of Geochemical Exploration. 7:

77-99.

DrillingInfo, 2017. Drillinginfo.com.

EIA (Energy Information Administration), 2016. EIA produces new maps of the Utica Shale play.

http://www.eia.gov/todayinenergy/detail.php?id=26052

El Nady, M., and Hammad, M. 2015. Organic richness, kerogen types and maturity in the shales of the

   Dakhla and Duwi formations in Abu Tartur area, Western Desert, Egypt: Implication of Rock-Eval

   pyrolysis. Petroleum Science, 37(4): 423-428.

Ettensohn, F.R. 2008. The Appalachian Foreland Basin Eastern United States, in Miall, A., The

   sedimentary basins of United States and Canada: Sedimentary Basins of the World, Elsevier,

   Amsterdam. 5(C): 105 – 179.

Ettensohn, F.R. 2010. Origin of Late Ordovician (mid-Mohawkian) temperate-water conditions on

   southeastern Laurentia: Glacial or tectonic: Geological Society of America Special Paper 466, p.

   163-175.

Ewing, R.P., and R. Horton. 2002. Diffusion in sparsely connected pore spaces: Temporal and spatial

   scaling. American Geophysical Union Journal: Water Resources Research. 38(12)

   doi:10.1029/2002WR001412.

Gao, Z.Y., and Hu, Q.H. 2013. Estimating permeability using median pore-throat radius obtained from

   mercury intrusion porosimetry. Journal of Geophysics and Engineering, 10, 025014.

   DOI:10.1088/1742-2132/10/2/025014.

Ghanbari, E., and Dehghanpour, H. 2015. Impact of rock fabric on water imbibition and salt diffusion in

   gas shales. International Journal of Coal Geology, 138: 55-67.

Ghanbarian, B., Hunt, A., Ewing, R., and Sahimi, M. 2013. Tortuosity in porous media: a critical review.

   Soil Science Society of America Journal, 77(5):1461.

Gregg, S.J., and Sing, K.S.W. 1991. Adsorption, Surface Area and Porosity. Academic Press, London, 303

   pp.

Guidry, K., Luffel, D., and Curtis, J. 1995. Development of laboratory and petrophysical techniques for evaluating shale reservoirs, final report: Des Plaines, Illinois, Gas Technology Institute, GRI-95/0496, 304 p.

Hager, J. 1998. Steam drying of porous media. Ph.D. Thesis, Department of Chemical Engineering, Lund University, Sweden.

Handy, L.L. 1960. Determination of effective capillary pressures for porous media from imbibition data. Petroleum Transactions, AIME. 219: 75–80.

Hansen, M. 1997. The Geology of Ohio-The Ordovician: Ohio Geology, Fall 1997.

Harris, A.G. 1979. Conodont color alteration, an organo-mineral metamorphic index, and its application to Appalachian Basin geology, in Scholle, P.A., and P.R. Schluger, eds., Aspects of diagenesis: Society of Paleontologists and Mineralogists Special Publication, 26: 3-16.

Hu, Q.H., Persoff, P., and Wang, J.S.Y. 2001. Laboratory measurement of water imbibition into low-permeability welded tuff. Journal of Hydrology, 242(1-2): 64–78.

Hu, Q.H., Ewing, R.P., and Dultz, S. 2012. Pore connectivity in natural rock. Journal of Contaminant Hydrology, 133: 76–83.

Hu, Q.H., and Ewing, R.P. 2014. Integrated experimental and modeling approaches to studying the fracture-matrix interaction in gas recovery from Barnett Shale. Final Report, Research Partnership to Secure Energy for America (RPSEA), National Energy Technology Laboratory, Department of Energy, 91p.

Hu, Q.H., Ewing, R.P., and Rowe, H.D. 2015. Low nanopore connectivity limits gas production in the Barnett Formation. Journal of Geophysical Research: Solid Earth, 120(12): 8073-8087.

Hu, Q.H., Y.X. Zhang, X.H. Meng，Z. Li, Z.H. Xie, and M.W. Li. 2017. Characterization of multiple micro-nano pore networks in shale oil reservoirs of Paleogene Shahejie Formation in Dongying Sag of Bohai Bay Basin, East China. Petroleum Exploration and Development, 44(5): 720–730.

Ismail, M., and Zoback, M. 2016. Effects of Rock Mineralogy and Pore Structure on Stress-dependent Permeability of Shale Samples. *Philosophical Transactions of the Royal Society A: Mathematical, Physical and Engineering Sciences* 374.2078.

Jarvie, D., Claxton, B., Henk, F., and Breyer, J. 2001. Oil and Shale Gas from the Barnett Shale, Ft. Worth Basin, Texas, AAPG National Convention, June 3-6, 2001, Denver, CO, AAPG Bulletin, 85(13): A100.

Jarvie, D.M., 2012. Shale Resource Systems for Oil and Gas: Part 2 – Shale-oil Resource Systems. American Association of Petroleum Geologist Memoir. 97: 89–119

Jiang, C., Bryant, S., and Daigle, H. 2015. A bundle of short conduits model of the pore structure of gas shale. Unconventional Resources Technology Conference (URTEC)., 20–22. http://doi.org/10.15530/urtec-2015-2169349

Kao, C. S., and Hunt, J.R. 1996. Prediction of wetting front movement during one-dimensional infiltration into soils: Water Resources Research, 32: 55-64

Katz, A.J., and Thompson, A.H. 1986. A quantitative prediction of permeability in porous rock. Physical Review B, 34: 8179–81.

Katz, A.J., and Thompson, A.H. 1987. Prediction of rock electrical conductivity from mercury injection measurements. Journal of Geophysical Research, 92(B1): 599–607.

Kaufmann, J. 2010. Pore space analysis of cement-based materials by combined nitrogen sorption – Wood's metal impregnation and multi-cycle mercury intrusion. Cement and Concrete Composites. 32(7): 514–522.

Kino. 2014. Optical Dynamic / Static Interfacial Tensiometer & Contact Angle Meter Brochure.

Klinkenberg, L.J. 1941. The permeability of porous media to liquids and gases. Drilling and Production Practice. 57–73.

Ko, L., Loucks, R., Milliken, K., Liang, Q., Zhang, T., Sun, X., Hackley, P., Ruppel, S., and Peng, S. 2017. Controls on pore types and pore-size distribution in the Upper Triassic Yanchang Formation, Ordos Basin, China: Implications for Pore-evolution Models of Lacustrine Mudrock. *Interpretation*, 5(2), SF127-SF148.

Labani, M., Rezaee, R., Saeedi, A., Hinai, A. 2013. Evaluation of pore size spectrum of gas shale reservoirs using low pressure nitrogen adsorption, gas expansion and mercury porosimetry: A case study from the Perth and Canning Basins, Western Australia. Journal of Petroleum Science and Engineering, 112: 7-16.

Lake, L. 2007. Petroleum engineering handbook: Reservoir Engineering and Petrophysics. Society of Petroleum Engineers. Chapter 11 – Water flooding. 5: 1042.

Langford, F.F., and Blanc-Valleron, M.M., 1990. Interpreting Rock-Eval pyrolysis data using graphs of pyrolyzable hydrocarbons vs. total organic carbon: AAPG Bulletin, 74: 799-804.

Lastoskie, C., Gubbins, K.E., and Quirke, N. 1993. Pore size distribution analysis of microporous carbons: a density functional theory approach. *Journal of Physics and Chemistry*, 97: 4786-4796.

Levinthal, J., Richards, B., Snow, M., Watrous, M., and McDonald IV, L. 2016. Correlating NORM with

mineralogical composition of shale at the microstructural and bulk scale. Applied Geochemistry,

76: 210-217.

Löhr, S.C, Baruch, E.T, Hall, P.A., and Kennedy, M.J. 2015. Is organic pore development in gas shales

influenced by the primary porosity and structure of thermally immature organic matter?. Organic

Geochemistry, 87: 119-132.

Loucks, R., Reed, R., Ruppel, S., and Jarvie, D. 2009. Morphology, genesis, and distribution of nanometer-

scale pores in siliceous mudstones of the Missippian Barnett Shale. Journal of Sedimentary

Research, 79: 848-861.

Loucks, R., Reed, R., Ruppel, S., and Hammes, U. 2012. Spectrum of pore types and networks in

mudrocks and a descriptive classification for matrix-related mudrock pores. AAPG Bulletin,

96(6): 1071–107.

Loucks, R., and Reed, R. 2014. Scanning-electronmicroscope petrographic evidence for distinguishing

organic-matter pores associated with depositional organic matter versus migrated organic

matter in mudrocks. GCACS Journal, 3: 51–60.

Micromeritics. 2001. Porosimetry brochure.

Milliken, K., Rudnicki, M., Awwiller, D., Zhang, T. 2013. Organic matter-hosted pore system, Marcellus

Formation (Devonian), Pennsylvania. AAPG Bulletin, 97: 177-200.

Morrow, N. R., Mason, G. 2001. Recovery of oil by spontaneous imbibition. Current Opinion in Colloid

and Interface Science, 6. 321-337.

NGI (Natural Gas Intel). 2017. Information on the Utica Shale. http://www.naturalgasintel.com/uticainfo

Obaje, N.G., Wehner, H., Scheeder, G., Abubakar, M.B., and Jauro, A. 2004. Hydrocarbon prospectively
of Nigeria's inland basins: organic geochemistry and organic petrology. AAPG Bulletin, 88(3):
325-353.

ONDR (Ohio Department of Natural Resources), 2013. Calculated Vitrinite Reflectance.
http://geosurvey.ohiodnr.gov/portals/geosurvey/Energy/Utica/Ordov-Shale_Ro-Average_03-
2013.pdf

ONDR, 2013. Ordovician Shale TOC Max Map.
http://geosurvey.ohiodnr.gov/portals/geosurvey/Energy/Utica/Ordov-Shale_TOC-Max_03-
2013.pdf

Orton, E. 1899. Petroleum and natural gas in New York: New York State Museum Bulletin. 6(30): 395-526

Ottman, J., and Bohacs, K. 2014. Conventional reservoirs hold keys to the 'Un's. AAPG Explorer. Feb.
2014.

Passey, Q.R., Bohacs, K.M., Esch, W.L., Klimentidis, R.E., and Sinha, S. 2010. From oil-prone source rock
to gas-producing shale reservoir – geologic and petrophysical characterization of unconventional
shale-gas reservoirs: SPE 131350, 29 p.

Patchen, D.G., Hickman, J.B., Harris, D.C., Drahovsal, J.A., Lake, P.D., Smith, L.B., Nyahay, R., Schulze, R.,
Riley, R.A., Baranoski, M.T., Wickstrom, L.H., Laughrey, C.D., Kostelnik, J., Harper, J.A., Avary,
K.L., Bocan, J., Hohn, M.E., and McDowell, R. 2006. A geologic playbook for Trenton-Black River
Appalachian basin exploration: U.S. Department of Energy, Final Report, 582 p.

Patchen, D. G., and Carter, K. 2015. A geologic play book for Utica Shale Appalachian Basin exploration.
West Virginia University Appalachian Oil & Gas Consortium. Final Report July 1, 2015.

Peters, K.E. 1986. Guidelines for evaluating petroleum source rock using programmed pyrolysis. AAPG

    Bulletin, 70: 318-329.

Peters, D., and Achaegakwo, C. 2016. Source-rock potential of the lower cretaceous sediments in SD – 1x

    well, offshore Tano Basin, south western Ghana. Petroleum and Coal, 58(4): 476-489.

Philip, J.R. 1957. The theory of infiltration: 4. Sorptivity and algebraic infiltration equations. Soil Science.

    84: 257–265.

Pope, M.C., and Read, J.F., 1997 High-resolution surface and subsurface sequence stratigraphy of late

    Middle to Upper Ordovician (late Mohawkian-Cincinnatian) foreland basin rocks, Kentucky and

    Virginia. AAPG Bulletin, 81(11): 1866–1893.

Quantachrom Instruments. 2015. autosorb iQ/ASiQwin operating manual.

Ravikovitch, P.I., Haller, G.L., and Neimark, A.V. 1998. Density functional theory model for calculating

    pore size distributions: Pore structure of nanoporous catalysts. Advance Colloid Interface

    Science. 76-77: 203-226.

Repetski, J.E., Ryder, R.T., Weary, D.J., Harris, A.G., and Trippi, M.H., 2014, Thermal maturity patterns

    (conodont color alteration index and vitrinite reflectance) in Upper Ordovician and Devonian

    rocks of the Appalachian basin—A major revision of USGS Map I–917–E using new subsurface

    collections, Chap. F.1

Rowan, E.L. 2006. Burial and thermal history of the central Appalachian basin, based on three 2-D

    models of Ohio, Pennsylvania, and West Virginia. U.S. Geological Survey Open-File Report 2006–

    1019.

Schlumberger. 2014. sCore Lithofacies Classification Reveals Barnett Reservoir Quality. Case Study.

    www.slb.com/ls

Sing K.S.W., Everett D.H., Haul R.A.W., Moscou L., Peirotti R.A. and Rouquerol J. 1985. IUPAC commission on colloid and surface chemistry including catalysis. Pure and Applied Chemistry, 57: 603–619

Swift, A., Sheets, J., Cole, D., Anovitz, L., Welch, S., Gu, X., Mildner, D., Chipera, S., Buchwalter, E., Cook, A. 2014. Nano- to microscale pore characterization of the Utica Shale. Unconventional Resources Technology Conference. URTeC 1923522.

Tinni, A., Fathi, E., Agarwal, R., Sondergeld, C., and Rai, C. 2012. Shale permeability measurements on plugs and crushed samples. SPE 162235 presented at the Canadian Unconventional Resources Conference, Alberta, Canada, 30 October – 1 November, 2012.

Tinni, A., Sondergeld, C., and Rai, C. 2014. Particle size effect on porosity and specific surface area measurements of shales. International Symposium of the Society of Core Analysts. Avignon, France. SCA 2014-013, 12 pp.

Tissot, B.P., and Welte, D.H., 1984. Petroleum Formation and Occurrence (2nd ed.). Heidelberg Springer-Verlag.

Tokonaga, T. K., and J. Wan, 2001. Surface – zone flow along unsaturated frock fractures. Water Resource Research, 84: 257-264.

Waples, D.W. 1985. Geochemistry in Petroleum Exploration. Reidel Publ. Co., Dordrecht and IHRDC, Boston.

Wallace, L. G., and Roen, J.B. 1989. Petroleum source rock potential of the Upper Ordovician black shale sequence, northern Appalachian basin: U.S. Geological Survey Open-File Report 89-488.

Wang, Y., Liu, S., and Elsworth, D. 2015. Laboratory investigations of gas flow behaviors in tight

    anthracite and evaluation of different pulse-decay methods on permeability estimation.

    International Journal of Coal Geology, 149: 118-128.

Washburn, E.W. 1921. Note on a method of determining the distribution of pore sizes in a porous

    material. Proceedings of the National Academy of Sciences, 7: 115–116.

Webb, A. 2001. An introduction to the physical characterization of materials by mercury intrusion

    porosimetry with emphasis on reduction and presentation of experimental data. Micromeritics

    Instrument Corporation.

Wickstrom, L. 2013. Geology and activity of the Utica-Point Pleasant of Ohio. Search and Discovery

    Article #10490,

    http://www.searchanddiscovery.com/pdfz/documents/2013/10490wickstrom/ndx_wickstrom.p

    df.html

Witt, W. D. 1993. Chapter 1 Principal oil and gas plays in the Appalachian Basin (Province 131) Middle

    Eocene Intrusive Igneous Rocks of the Central Appalachian Valley and Ridge Province—Setting,

    Chemistry, and Implication for Crustal Structure. U.S.G.S. Survey Bulletin, 1839-I.

Xu, M., Dehghanpour, H., 2014. Advances in understanding wettability of gas shales. Energy and Fuels,

    28: 4362–4375.

Yang, R., Hao, F., He, S., He, C., Guo, X., Yi, J., Hu, H., Zhang, S., and Hu, Q.H. 2017. Experimental

    Investigations on the Geometry and Connectivity of Pore Space in Organic-rich Wufeng and

    Longmaxi Shales. Marine and Petroleum Geology, 84: 225-42.

Zhang, X., Morrow, N., and Ma, S. 1996. Experimental verification of a modified scaling group for

    spontaneous Imbibition. SPE Reservoir Engineering, 11.04: 280-85.

Biographical Information

Dillon Worley is from Spring, Texas where he attended high school at Klein High School. He decided to attend Texas A&M University and was a member of the cross country and track & field team. After only 3 years he received his Bachelors of Science in Geology in August 2015. From there, he wanted to further study his passion for rocks and decided to pursue a Master's degree from the University of Texas at Arlington starting in August 2015. Here, Dillon found an extra interest in nano-petrophysics and decided to join Dr. Q.H. Hu's research team. After graduation Dillon is going to pursue a job in the oil and gas industry.